2013

The constant-pressure gas-driven radial displacement and viscous fingering instability in a finite liquid drop in a Hele-Shaw cell

Andrew Ryan White
Iowa State University

The constant-pressure gas-driven radial displacement and viscous fingering instability in a finite liquid drop in a Hele-Shaw cell

by

Andrew R. White

A thesis submitted to the graduate faculty

in partial fulfillment of the requirements for the degree of

MASTER OF SCIENCE

Major: Engineering Mechanics

Program of Study Committee:

Thomas Ward III, Major Professor

Paul Durbin

Thomas Rudolphi

Iowa State University

Ames, Iowa

2013

DEDICATION

I would like to dedicate this thesis to my mother and father for all the love and support they have provided me through both the best and worst of times.

TABLE OF CONTENTS

LIST OF FIGURES

ACKNOWLEDGEMENTS

I would like to express my sincerest gratitude to my advisor Dr. Thomas Ward for all of the support and direction he provided me over the past several years beginning with his lectures on fluid dynamics in the fall of 2008; without him this would not have been possible. I would like to thank the Department of Mechanical and Aerospace Engineering at North Carolina State University for providing me a foundation in engineering on which to build, and I would like to thank the Department of Aerospace Engineering at Iowa State University for supporting the remainder of my Master of Science degree. I also wish to thank Dr. Paul Durbin and Dr. Thomas Rudolphi for being on my program of study committee and for the assistance they provided in completing this thesis.

ABSTRACT

The displacement of a liquid by a less viscous fluid in a porous medium or other small geometry often results in an interfacial instability that takes the form of "fingers" or "tongues." Typically referred to as viscous fingering or the Saffman-Taylor instability, this instability has direct relevance to many industries. For example in oil recovery nearby water can enter the oil reservoir and hinder yields, while some enhanced oil recovery techniques use fluids to displace oil and become less effective as the instability appears. This instability is also detrimental to gas-assisted injection molding and some embossing processes, while it could produce desirable effects in some industries such as patterning thin polymer films. Unfortunately the majority of studies of the two-phase displacement problem introduce the displacing fluid at a constant flow rate as opposed to a constant pressure. In this thesis a finite liquid drop is displaced radially by a gas at constant pressure in a Hele-Shaw cell. A Hele-Shaw cell consists of two parallel plates with a gap spacing much smaller than the length and width, effectively producing a two-dimensional flow. The problem is investigated in three separate studies: the displacement of glycerol-water mixtures by air, the displacement of aqueous $Ca(OH)_2$ by CO_2, and the displacement of mineral oil with dissolved polyisobutylene, a shear-thinning liquid, by air. Experimental videos are analyzed to track the expansion of the gas phase and the development of the instability, and a simple conservation of volume approach is used to estimate the residual film produced by the displacement. Finally a novel quantity is defined to justly compare very different instability regimes such as smooth pedal-like fingers (primarily a Newtonian effect) and fractal dendritic fingers (primarily a shear-thinning effect) in order to quantify the instability and its growth.

CHAPTER 1. GENERAL INTRODUCTION

1.1 Introduction

When a less viscous fluid displaces a more viscous fluid the interface often becomes unstable. Typically called *viscous fingering* or the *Saffman-Taylor instability*, the instability takes the form of "fingers" or "tongues" of the less viscous phase penetrating the more viscous phase and is often associated with adverse effects such as inefficient displacement. This two-phase displacement problem occurs regularly in porous media and in other small geometries in a number of industries. For example the instability can directly impact oil recovery(1; 2). Also some fluid-assisted injection molding technologies are concerned with the two-phase instability (3; 4), and viscous fingering can occur in hot embossing and other soft lithography process (5; 6). The viscous fingering problem has been studied extensively dating back to the 1950s in Hele-Shaw cells (see: Literature review) . A Hele-Shaw cell consists of two flat parallel plates where the gap between them is much smaller than the length and width of the plates. This allows for good visualization of the experiments and effectively produces a two-dimensional flow. Viscous fingering problems have been studied in both linear and radial geometries with a wide range of fluids. Displacing fluids have included gases such as air and CO_2 and liquids such as water and glycerin, while the displaced fluids have included liquids from oils to non-Newtonian liquid crystals. The majority of these viscous fingering studies have used constant flow rates for the displacing phase which makes the mathematical analysis more straight forward.

In the following chapters the viscous fingering problem is studied in a radial Hele-Shaw cell where the displacing phase is a gas at *constant pressure*. The constant pressure problem is fundamentally different from the constant flow rate problem, a key difference being the average velocity of the interface is no longer constant. Additionally in this thesis the constant pressure

gas displaces a *finite volume* drop of liquid. This means at some elapsed time the gas phase bursts out of the liquid drop which is a phenomenon only studied recently (7; 8). The finite volume also allows for an estimation of the residual film resulting from the displacement process which has only been done recently (7; 8; 9).

While the constant pressure and finite volume viscous fingering problem will be presented in the next chapters with different fluids and motivations, each will use similar analytical tools. In general the rate of displacement of the liquid by the gas will be examined as will the residual film thickness. Additionally, since performing the experiments discussed in chapters 2 and 3, improvements have been made in the image analysis which will allow for a new quantitative measure of the instability in chapter 4. Unfortunately the constant pressure problem makes the application of analytical analyses difficult and so many of the results will rely on empirical relationships.

1.2 Thesis organization

This thesis contains two previously published papers plus some new results. The following section will provide a brief literature review highlighting a number of the major milestones in the paradigm's history. Chapters 2 and 3 will each contain one of the previously published papers in its entirety with its own introduction, analysis, procedure, results, discussion and conclusion. Chapter 4 will present new results on viscous fingering in shear-thinning liquids and will contain its own introduction, analysis, procedure, results, discussion and conslusion. A general conclusion as well as a discussion of some future work will be presented in chapter 5 followed by a bibliography for the entire thesis.

1.3 Literature review

The viscous fingering problem has been recognized for many years by the oil industry where, for example, the extraction of oil can cause nearby water to enter the oil reservoir, or fluids can be used to displace oil to aid in oil recovery. Some of the first analyses of the displacement problem were published by Muskat and Wyckoff in 1935 (1) and then Arthur in 1944 (2) to

understand how the instability affects oil recovery. Later in 1950 the first lab experiments showing viscous fingering were performed by Lewis (10) to support the first stability analysis of the fingering problem performed by Taylor in 1950 (11). The experimental apparatus used by Lewis consisted of two parallel plates with some gap spacing that is considerably smaller than the length and width of the plates. This apparatus, commonly known as a Hele-Shaw cell in honor of H.S. Hele-Shaw (12), has since become the standard for investigating this two-phase displacement problem. A convenient aspect of Hele-Shaw flow is that the lubrication approximation can be applied. Then when the flow is fully developed and the fluids of interest are incompressible the gap-averaged velocity reduces to Darcy's law

$$\bar{u}_1 = -\frac{b^2}{12\mu}\frac{dp}{dx_1} \tag{1.1}$$

where b is the gap and μ is the dynamic viscosity, making the experiment analogous to flow in a porous medium with permeability $\frac{b^2}{12}$. Within six months of each other between 1958 and 1959 Saffman and Taylor (13) and then Chuoke *et al* (14) performed nearly identically linear stability analyses on the fingering problem beginning with the velocity potential from Darcy's law. While the viscous fingering instability is called the *Saffman-Taylor instability* in many textbooks and papers in honor of their work published in 1958, there is some debate about to whom the instability should be attributed (15).

Paterson in 1981 (16) performed the first radial viscous fingering experiments in a Hele-Shaw cell, providing a more realistic view of how a gas bubble would behave in an oil reservoir accompanied by a linear stability analysis of the radial problem. This approach to the viscous fingering problem is significant because it eliminates wall effects whereas previous linear studies could only accurately analyze fingers away from the walls. From 1980 onward work on viscous fingering has flourished. Advances in the stability analysis of the linear problem were made by Park and Homsy (17; 18) in 1984 where improvements were made on the interfacial boundary condition.

Nittmann *et al* in 1985 published the first experiments where a non-Newtonian shear-thinning liquid was used (19). Their results are significant because for the first time fractal fingering patterns were observed due to the shear-thinning effects. Daccord and Nittmann a year

later made one of the first analyses of this non-Newtonian fingering instability by using a fractal dimension (20). Afterward many studies using shear-thinning and other non-Newtonian liquids have been performed. One of the few studies of a constant pressure driven non-Newtonian system was done in 1987 by Buka *et al* (21; 22). In their work the radial displacement of liquid crystals was investigated and an attempt at a linear stability analysis for the constant-pressure system was made. While their experimental data agrees well with their stability analysis they use Darcy's law to determine the velocity of the liquid-gas interface which may not be valid. As will be shown in this thesis the interface velocity is not constant for the radial constant-pressure problem and therefore the flow cannot be considered fully developed. Another of the few constant pressure non-Newtonian studies was performed by Yamamoto in 2001 a linear Hele-Shaw cell where an analysis of the fingering patterns and finger development was studied (23). Some stunning numerical work on the gas-driven displacement of shear-thinning liquids has been performed by Fast *et al* in 2001 and 2004 (24; 25) however they are considering a fixed capillary number i.e. fixed velocity which again is different from the constant pressure study presented in this thesis. For an in-depth review of the viscous fingering problem up to 1995 refer to work by McCloud (26).

In the past decade the area of viscous fingering has continued to grow. New work on viscous fingering with an interfacial chemical reaction, where the displacement is driven by a constant flow rate or the reaction itself, has been performed by De Wit and others (27; 28; 29; 30). Other work continues to refine the analyses of the constant flow rate problem in radial geometry (31). Carrillo *et al* studied displacement in a *rotating* Hele-Shaw cell (9). Their study used a finite liquid volume which allowed for a measure of the film thickness by simple mass conservation. In papers by Ward and White in 2011 (7) and White and Ward in 2012 (8) the use of a finite liquid drop was also used and for the first time the bursting of the gas phase out of the liquid drop was analyzed. Also in (8) the exponential increase in the displaced volume due to constant pressure injection was for the first time shown with and without a fingering instability. These two papers are shown in their entirety in chapters 2 and 3. Recently Dallaston *et al* have been working on numerical solutions to the finite volume problem, however the bursting phenomenon is yet to be achieved numerically (32).

Recently the research trend has focused on altering the geometry in an attempt to limit or prevent the instability from occuring. Techniques such as using elastic plates in a Hele-Shaw cell (33) and introducing gradients in the gap height (34) have been shown to limit the instability. A method for suppressing the instability by using a pulsed pressure injection will be described in the future work section of this thesis.

CHAPTER 2. GAS DRIVEN DISPLACEMENT OF A LIQUID IN A PARTIALLY FILLED RADIAL HELE-SHAW CELL

A paper published in *Physical Review E*[1]

Thomas Ward[2,3], Andrew R. White[4]

2.1 Abstract

The displacement of liquids from confined geometries by using a gas phase is a problem that is relevant to many technologies. Efficient removal of the liquid phase is achieved when an extremely thin residual fluid film is produced as it is displaced. Here the dynamics of air, at constant pressure, displacing a glycerol-water drop in a radial Hele-Shaw cell is studied in this context at low Reynolds numbers. Empirically derived expressions relating the input parameters (fluid viscosity, pressure and drop volume) to characteristic gas flow and liquid displacement rates, and the steady state film thickness, are proposed and compared with experiments. The experiments consist of measuring cross sectional areas of the penetrating gas (air) and displaced liquid using glycerol-water mixtures with viscosities ranging O (1-100) cSt and with inlet pressures ranging 3.5-10.5 kPa at gap spacings of 50-100 μm. We estimate that the system produces residual film thicknesses in the range of 5-95 μm.

[1] *T. Ward, A. R. White. Gas-driven displacement of a liquid in a partially filled radial Hele-Shaw cell.* Phys. Rev. E ***83**, (2011)*

[2] Assistant professor, Department of Mechanical and Aerospace Engineering, North Carolina State University

[3] Author for correspondence: thomasw@iastate.edu

[4] Undergraduate student, Department of Mechanical and Aerospace Engineering, North Carolina State University

2.2 Introduction

The displacement of a viscous fluid phase by a gas phase has been of interest to academics and industries for many years. There are several emerging and existing technologies where determining operating conditions that result in the efficient displacement of the more viscous phase is a desired outcome such as enhanced oil recovery processes that utilize CO_2 gas (35). Other relevant technologies include the evaporation (36), or cooling (37) of a liquid phase by the penetrating gas phase, so that it may be useful in a microgravity environment where, for example, processes involving buoyancy driven displacement, such as boiling, are difficult to engineer (38; 39). In each of these examples the fundamental question is how to efficiently displace liquids in small geometries by using a less viscous gas phase. In this manuscript a radial Hele-Shaw cell geometry with gap spacing, b, less than the capillary length $\ell_c = \sqrt{\gamma/\rho_L g}$ (where γ is the liquid-solid surface tension in air, ρ_L is the liquid phase density and g the gravitational acceleration constant) is used to experimentally study the dynamic penetration of a gas injected at a constant pressure into a finite volume of a viscous liquid, and to measure the residual thin film prior to bursting, i.e. break-though of the gas phase, at time t_{end}. The usual Saffman-Taylor fingering instability (13) occurs during the penetration of the gas into the liquid but the details of the fingering are not studied here. Instead we focus on the measurement of thin films and penetration rates of a less viscous fluid into a more viscous one in a radial Hele-Shaw cell geometry at low Reynolds number.

The desired experimental result is the displacement of a more viscous fluid by a less viscous fluid in a confined geometry where transport occurs in only the radial direction at the penetrating gas-liquid interface. But in practice this is never observed due to the formation of films of the more viscous fluid. Thick films can result in little radial displacement that can later develop into large droplets on the substrates where the maximum drop height is on the order of the capillary length (40). In this manuscript it is assumed that the bursting time, t_{end}, is much shorter than the time required to produce a sufficient number of drops on the order of the gap spacing b (according to (40) this can take days for molecular scale films, in our experiments we typically observed droplet formation after bursting) and the film that results

from the penetrating gas is assumed to be steady.

There is much literature on the subject of thin film formation by penetration of a viscous fluid phase with a less viscous one (26; 41; 42; 43; 44; 45) and our discussion of these previous studies is to point out their similar conclusions. In general, all theories and experiments suggest that steady film thicknesses always scale like $h_\infty = C_0 Ca^{*n}$ where $Ca^* = U\mu_L/\gamma$ (here and throughout the manuscript asterisks $\cdot^*$ denote a dimensionless variable) is the capillary number based on a steady velocity U and liquid viscosity μ_L. The steady film thickness is h_∞, and the power n and the coefficient C_0 are determined for a systems geometry, and range of capillary numbers. For the film that forms when a bubble penetrates liquid in a tube the power is $n = 2/3$ for capillary numbers $Ca^* < 1 \times 10^{-3}$ (64); the exponent power is slightly smaller at $n = 1/2$ for small capillary numbers $1 \times 10^{-3} < Ca^* < 1 \times 10^{-2}$ (46; 47; 48) and for $Ca^* \geq 1$ an asymptotic limit of h_∞ is approached (47). A power of $n = 2/3$ was also determined for the problem of thin film formation due to displacement of a more viscous fluid by a less viscous fluid in a two dimensional geometry (17; 49; 50).

indent It is more difficult to develop similar expressions relating the capillary number and film thickness for the problem of film formation due to fluid displacement in a *radial* Hele-Shaw geometry because the definition for a steady velocity is not easily accessible. Therefore, most previous Hele-Shaw studies in radial geometries focused on the Saffman-Taylor instability since a radial geometry allowed analysis of the moving front without interference from sidewalls (13; 15; 16; 18; 31; 51).

In 1999, Carrillo et al (9), through a combination of analysis and experimentation, studied fluid displacement driven by axial rotation in a radial Hele-Shaw geometry in the limit of low Reynolds and Rossby numbers. A study combining experiments and analysis of a similar system and for a wide range of rotation rates was performed in 2006, by Álvarez-Lacalle et al, (52). In the inaugural studies of the axial rotation of a radial Hele-Shaw cell performed by Carillo et al, there were two conditions proposed: 1) a pre-wet Hele-Shaw cell with a drop placed in the center and 2) a dry Hele-Shaw cell with all other conditions the same as the first. Their problem was unique because the authors were able to avoid the usual fingering instability by using rotation to generate centrifugal acceleration to displace the liquid phase,

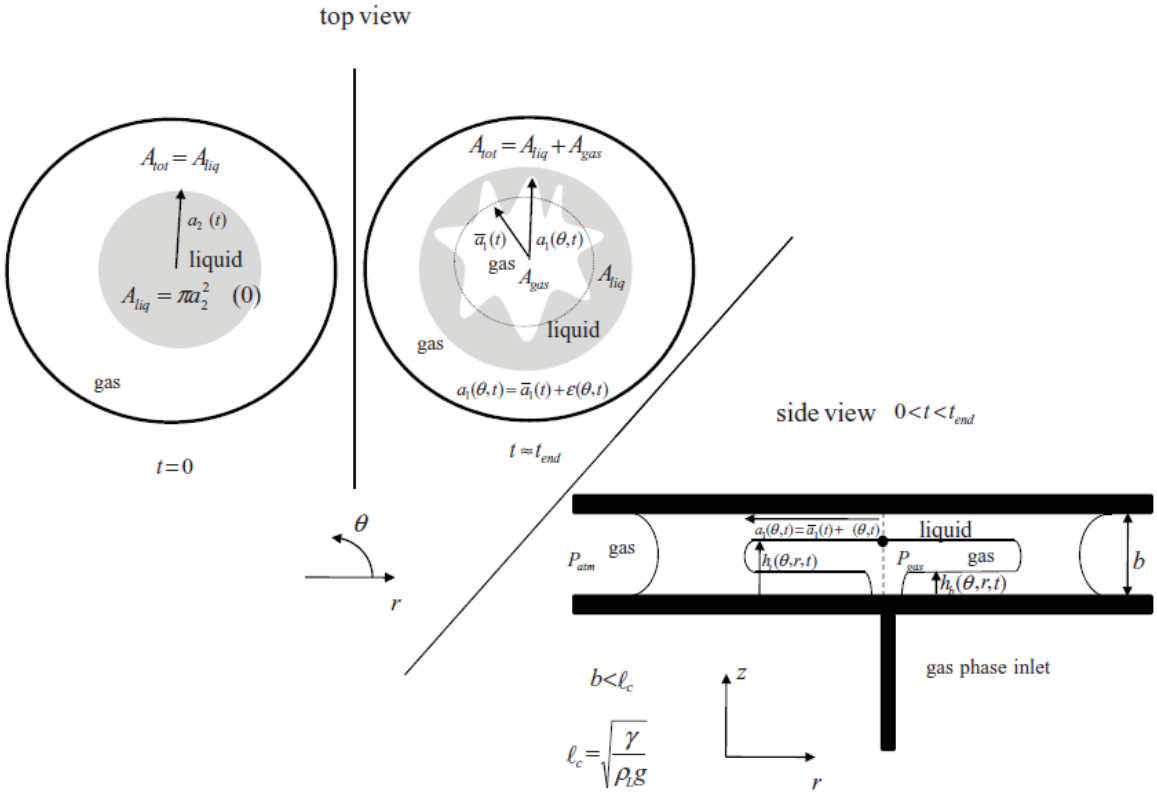

Figure 2.1 *Top and side view of problem schematic and experimental setup. The top view shows the initial drop configuration at time $t = 0$ and the proposed configuration at later times where a typical fingering instability develops in the azimuthal direction. The radial distance measured from the center to the inner air gas interface, a_1, is assumed to be the sum of an average component that is independent of the azimuthal direction and an azimuthally symmetric disturbance radius, i.e. $a_1(\theta,t) = \bar{a}_1(t) + \varepsilon(\theta,t)$. The side view shows the proposed configuration for the top and bottom films and the average radial velocity profile $\bar{u}$ that is only a function of the radial distance, r.*

which subsequently syphoned the less viscous phase fluid (air) into the Hele-Shaw cell in their experiments. The ability to measure film thickness was possible in their system because the authors considered the displacement of a finite volume of liquid, denoted here as V_{liq}. The finite volume allows tracking of the outer and inner annular liquid radii, then with knowledge of the initial radius the authors determine a steady film thickness where they show that the residual film were less than 10% of the gap spacing. Note that in Carrillo et al (9) an empirical capillary number was developed and we seek to do the same. We also form transport equations and develop expressions for displacements rates and film thickness based on the cross sectional areas (penetrating gas and total) for the problem of a viscous fluid being displaced by a pressure-driven less viscous one by developing empirical correlations based, in part, on the analysis of (9).

In the next section the problem description and cross sectional area evolution equations are discussed. This is followed by an explanation of the experiments, and details of the procedure. Then the experiments and results are analyzed qualitatively and quantitatively to describe data trends. In the last section we conclude with some remarks on the results and possible future experiments.

2.3 Analysis

The purpose of this section is to develop expressions for the film thickness resulting from gas driven displacement of a partially-liquid filled region in a radial Hele-Shaw cell by using average displacement. To develop this equation we assume that the displaced liquid and gas phase liquid forms a steady thin-film as it is displaced for the conserved volumes. Empirical correlations for the rate of displacement of the inner and outer cross sectional areas are also introduced in the subsections that follow.

We begin with a discussion on the relative inner and outer annular radii a_1 and a_2, respectively, where the inner gas phase displaces the outer liquid phase fluid. We assume that the annular outer radius is simply a function of time, $a_2(t)$, since the annular liquid is bounded by air. The inner gas creates a Saffman-Taylor instability as it penetrates the liquid phase, and for large amplitude instabilities, where a_1 is on the order of a_2, the approximation that

a_2 is only a function of time will not hold. But it is observed to be accurate for the range of parameters presented in this study. We also only consider average gas phase radius $\bar{a}_1(t)$ in the analysis by assuming that the gas phase radius is the sum of a uniform-average radius and a linear azimuthal disturbance $a_1(\theta,t) = \bar{a}_1(t) + \varepsilon(\theta,t)$ (31), where the disturbance is periodic in θ and possess azimuthal symmetry such that $\varepsilon(+\theta,t) = \varepsilon(-\theta,t)$ on some domain $\theta \in [-\pi,\pi]$.

Using this information we now consider an initially cylindrical-viscous Newtonian droplet, of radius $a_2(0)$, concentrically confined between two parallel circular plates at a distance b apart where $b \ll \ell_c$ (see Fig. 2.1 for problem illustration) or equivalently the Bond number $Bo^* = (b/\ell_c)^2 \ll 1$. At time $t > 0$ a gas is injected into the center of the parallel plates at a constant pressure P_{gas} where the gage pressure is written as $\Delta P = P_{gas} - P_{atm}$ with P_{atm} equal to ambient atmospheric pressure. The injection pressure is assumed low i.e. $\Delta P/P_{atm} \ll 1$ so that the gas density and temperature are both considered constant throughout the displacement process (53). It is also assumed that surface tension is negligible where $\Delta P > \gamma/b$. At time t_{end} the drop bursts resulting in rupture of the gas-liquid interface. The liquid properties of viscosity μ_L, density ρ_L, and subsequently the kinematic viscosity denoted $\nu_L = \mu_L/\rho_L$, along with the surface tension at the gas-liquid interface, γ, are used for normalization throughout the manuscript and their values are assumed to remain constant for a given experimental setup.

2.3.1 Volume conservation

The gas phase average radius, $\bar{a}_1(t)$, is difficult to estimate from experimental data because of the Saffman-Taylor instability (13). So we instead rely on volume conservation to develop expressions for the transient cross sectional area of the gas $A_{gas} = \int_{A_{gas}} dA$ (with $dA = r\,dr\,d\theta$ a differential area element), which will allow for direct comparison between theory and experiments where in the experiments $A_{gas} = \sum_i A_{gas_i}$ where A_{gas_i} is an area element based on an image pixel, i. In general, values for the transient gas phase volume, V_{gas}, depend on the film that is deposited on the top and bottom walls as the liquid is displaced, where the distance measured from the bottom wall to the lower and upper portion of the gas phase are denoted as h_t and h_b respectively (see Fig. 2.1 for description) and may not be spatially uniform. But the Bond number is considered small in the problem statement so the variations in the

top and bottom film are negligible in this limit and $h_t = h_b$. Dividing the gas volume, V_{gas}, by the gas area, A_{gas}, yields an average gas layer thickness $\frac{V_{gas}}{A_{gas}} = b - \bar{h}$, where $\bar{h}$ is the (top and bottom) average-radial liquid film thickness spanning the gas region. The liquid volume $V_{liq} = \pi a_2^2(0)b$ is constant with no simple expression for the area $A_{liq} = \int_{A_{liq}} dA$. The total volume, $V_{tot} = V_{gas} + V_{liq}$, is equal to $A_{tot}(t)b$ where we define the change in total volume as being equal to the gas volume $\Delta V_{tot}(t) = V_{tot} - V_{liq} = A_{tot}b - \pi a_2^2(0)b = V_{gas}$ where we consider all cross sectional areas to be uniform in the z-direction, and also assume a similar relationship between differential and image pixel based expressions for the total area as there is for the gas area A_{gas}. Note that the gas area and change in total area also share the same initial condition $A_{gas}(0) = \Delta A_{tot}(0) = 0$.

The expression relating the change in total volume with the gas volume may be re-written as $\Delta A_{tot} b = A_{gas}(b - \bar{h})$ where ΔA_{tot} and A_{gas} differ by a constant $\frac{b-\bar{h}}{b}$ when considering steady averaged-films i.e. $\frac{d\bar{h}}{dt} = 0$. A steady film assumption is not physically possible at early times since the total film thickness value is initially equivalent to the plate separation distance. But after a sufficient amount of elapsed time the average film thickness in the region spanning the gas phase is given by,

$$\frac{\bar{h}}{b} = 1 - \frac{\Delta A_{tot}}{A_{gas}}, \tag{2.1}$$

where $\bar{h}$ is analogous to $2h_\infty$, the value used in the traditional liquid film measurement problems. Also, this particular result is analogous to the one derived in (9) for a finite volume of fluid displaced in an initially dry rotating Hele-Shaw cell.

2.3.2 Displacement rates

For the gas phase area we assume an empirical relationship for the expansion rate of the form $\dot{A}_{gas} = \omega A_{gas}$ (dots denote derivatives with respect to time), and subsequently $\Delta \dot{A}_{tot} = \omega \Delta A_{tot}$, due to volume conservation. These expressions are based on experimental observations and (9). Integration of these equations, with the initial conditions $A_{gas}(0) = \Delta A_{tot}(0) = 0$ and $\frac{\dot{A}_{gas}}{A_{gas}} = \frac{\Delta \dot{A}_{tot}}{\Delta A_{tot}} = \omega$, for $t > 0$, results in expressions for the transient cross sectional areas,

$$A_{gas}(t) = C_{gas}\left(e^{\omega t} - 1\right), \text{ and} \tag{2.2a}$$

$$\Delta A_{tot}(t) = C_{tot}\left(e^{\omega t} - 1\right). \tag{2.2b}$$

To determine an expression for ω we analyze the dimensionless momentum conservation equation $Re^*(\mathbf{u}^*_{t^*} + \mathbf{u}^* \cdot \nabla^* \mathbf{u}^*) = \nabla^* \cdot \boldsymbol{\sigma}^*$ using $1/\omega$, b and ωb for the time, length and velocity scales respectively, and $\mu_L \omega$ for the stress scale $\boldsymbol{\sigma}$ with $\boldsymbol{\sigma} = -P\mathbf{I} + \boldsymbol{\tau}$ where $\boldsymbol{\tau} = \mu_L[\nabla \mathbf{v} + \nabla \mathbf{v}^T]$ is the viscous stress tensor and $\mathbf{I}$ is the identity tensor. In the limit $Re^* = \frac{\omega b^2}{\nu_L} \ll 1$ we propose that $\omega \propto \Delta P/\mu_L$ based on dimensional analysis that the fluid is driven by a gas at constant pressure.

Developing empirical relationships for the coefficients, C_{gas} and C_{tot}, and ω, are not straightforward since each depends on the variables μ_L and ΔP and possibly b. Therefore, the main focus on the gas area and the total area rate equations is to determine if the relationship for the characteristic rate $\omega \propto \Delta P/\mu_L$ is accurate within our range of experimental parameters. A more general empirical relationship for ω will be used for comparison with experiments and is a power law of the form,

$$\omega = C_\omega \left(N_\omega \frac{\Delta P}{\mu_L}\right)^m \tag{2.3}$$

where m is to be experimentally determined. Values of m in the vicinity of unity would reinforce the validity of the main assumptions in this radial flow model.

For the total film thickness an empirical relationship is derived by considering the generic capillary number $Ca^* = v_{char}\mu_L/\gamma$. Using this definition with characteristic velocity $v_{char} = \omega b$ would yield a dimensionless group that is independent of viscosity for $m = 1$. A more precise velocity for the inner annular region is derived by considering the first two non-zero terms in the Taylor expansion of the average gas displacement written in terms of the transient area [Eq. (2.2a)] yielding the expression $\bar{a}_1(t)\sqrt{\pi} = \sqrt{A_{gas}} \approx \sqrt{\omega t + O(\omega t)^2}$. Ignoring higher order terms, $O(\omega t)^2$, in the expansion suggests that the coefficient for the average velocity and average acceleration are both proportional to $\sqrt{\omega}$ at early elapsed time. Inserting this expression into the capillary number suggest a numerator that scales like $Ca^* \propto \mu_L\sqrt{\omega} = \sqrt{\mu_L \Delta P}$. We use

this result to propose an empirical relationship for the film thickness in terms of the viscosity and pressure of the form,

$$\frac{\bar{h}}{b} = C_{\bar{h}} \left(N_{\bar{h}} \mu_L \Delta P\right)^n \tag{2.4}$$

where the normalization constant is proportional to the surface tension i.e. $N_{\bar{h}} \propto \gamma$. The power n is to be determined experimentally where measured values of $2n$ in the vicinity of 0.50 would suggest the reasoning used to develop the empirical correlation is valid. A two term power law, in μ and ΔP, would be a much better choice but determining the separate powers from experimental data would be difficult given that we can essentially only measure the cross sectional areas, A_{gas} and A_{tot}.

The functional dependence with ΔP and μ_L that has been proposed for ω and $\bar{h}/b$ are each normalized by $N_\omega = \sqrt{\frac{\rho_L b^3}{\gamma}}$ and $N_{\bar{h}} = \sqrt{\frac{b}{\rho_L \gamma^3}}$, respectively, determined by using dimensional analysis. Experiments are performed to determine the constants and the exponential powers for these expressions.

2.4 Experiments: materials and procedure

A Hele-Shaw cell was created using two circular acrylic plates with a diameter of 100 mm (4 in.) and uniform thickness of approximately 3.2 mm (1/8 in.) set 50, 75 or 100 μm apart on an acrylic stand. Plastic shims (AccuTrex) were placed between the plates to provide the desired gap spacing. In order to insert air into the cell a standard 8-32NC thread was tapped in the center of one plate and a plastic pipe fitting (Cole Parmer) with an inner diameter of 2.4 mm (3/32 in.) was inserted. Air pressure was controlled using a pressure transducer (Marsh Bellofram) and a function generator (Agilent) to provide a step function. Current, I, from the function generator in the range of $4.8 < I < 10.4$ mA was supplied to the transducer to yield pressure outputs of $\Delta P = 3.5, 7.0$ or 10.5 kPa $(0.5, 1.0$ or 1.5 psig). There was no observable flexing of the plates used to form the Hele-Shaw cell when tested at these low pressures (less than 15% of 1 atmosphere). An air compressor was used to fill a storage tank to provide pressurized air for the experiments when necessary, and was connected to the transducer with

tubing that had an inner diameter of 6.4 mm (1/4 in.). Glycerol-water mixtures were used as the experimental liquid. Kinematic viscosities of roughly 4, 37, and 280 cSt were made using mixtures of 50%, 80%, and 95% glycerol-water respectively (54; 55). Based on these viscosities and our other parameters we determine the Reynolds number to be in the range of $10^{-5} < Re^* < 10^{-1}$. Surface tension for pure glycerol on acrylic is approximately 60 mN/m, yielding values of $\gamma/b \approx 1.2$ kPa for the smallest gap spacing. Therefore $\Delta P > \gamma/b$ for our range of pressures although the ratio $\gamma/(b\Delta P)$ is approximately one-third for the smallest pressure of 3.5 kPa. Bond numbers are in the range $0.01 < Bo^* < 0.1$, based on capillary lengths in the range of 1-2 mm where the value varies due to the density difference between the fluid mixtures. The range of normalized correlation parameters are $1 < N_\omega \frac{\Delta P}{\mu_L} < 500$ and $0.1 < N_{\bar{h}} \mu_L \Delta P < 100$ for ω and $\bar{h}/b$, respectively.

Drops with volumes of either 13, 30 or 50 μl were placed at the center of the Hele-Shaw cell by using an Eppendorf syringe. The supply valve from the storage tank to the transducer was opened prior to the signal generator supplying the transducer with a current. As the signal generator began to supply the transducer with a current the transducer allowed the pressurized air to enter the cell through the tapped hole. A CCD camera (PixeLINK) looking normal to the cell from above was used to capture video of the experiment at a minimum of 30 fps at the maximum resolution of 1280 × 1024 pixels and at a maximum of 100 fps at a reduced resolution of 640 × 480. The video captured an experiment from just before the initial injection of the air until a few seconds after the drop burst. Run times for the experiments ranged from less than 0.1 to over 102 s depending on viscosity, providing a minimum of approximately 10 experimental images for analyzing each experiment. The combination of volumes, viscosities, pressures and gap spacings yielded 51 experiments. Several experiments at small gap spacings, $b < 75$ μm, with the lowest viscosity fluid of 4 cSt were difficult to perform as the drops were susceptible to meandering or to an instability that occurs along the interface as they are squeezed between the plates (56). After each experiment the Hele-Shaw cell was disassembled. Water with a small amount of soap was applied to each side of both acrylic plates followed by a thorough rinse with water. A soft towel was used to dry the plates to avoid scratching and the Hele-Shaw cell was reassembled for a new experiment.

A MATLAB program was used to precisely analyze the images. For each image frame the gas area and the total area were measured by calculating and summing local pixel intensities, $A_{gas_i} = \sum_i A_{gas_i}$ and $A_{tot_i} = \sum_i A_{tot_i}$, respectively. There were some initial pixels that were always present due to the pixel intensity of the gas phase inlet and therefore produced a non-zero initial area for the gas phase. Only the frames from the initial injection of air until the first burst were analyzed with the bursting time recorded as t_{end} for these experiments. The area data was used to produce an average film thickness estimate using Eq. (2.1). A steady state film value for the average film thickness measurements is defined as the final two to three values for the film thickness being within 10% of one another. No error bars are plotted in the following graphs because none of the data is averaged.

2.5 Experiments: results and discussion

2.5.1 Qualitative results

Fig. 2.2 shows images of drops prior to bursting for a range of pressures and viscosities. The set of top and bottom images represents results of experiments with two different initial volumes of 13 and 50 μl, respectively, with the pressures listed in the left hand column. In general the Saffman-Taylor instability is always present (13; 16). The amplitude of the fingers appear less pronounced at the lower pressures, for a given volume and viscosity, and tend to become more pronounced through branching and tip splitting events at higher pressures according to the images. Also, the fingering pattern appear to be symmetric for most of the experimental images shown.

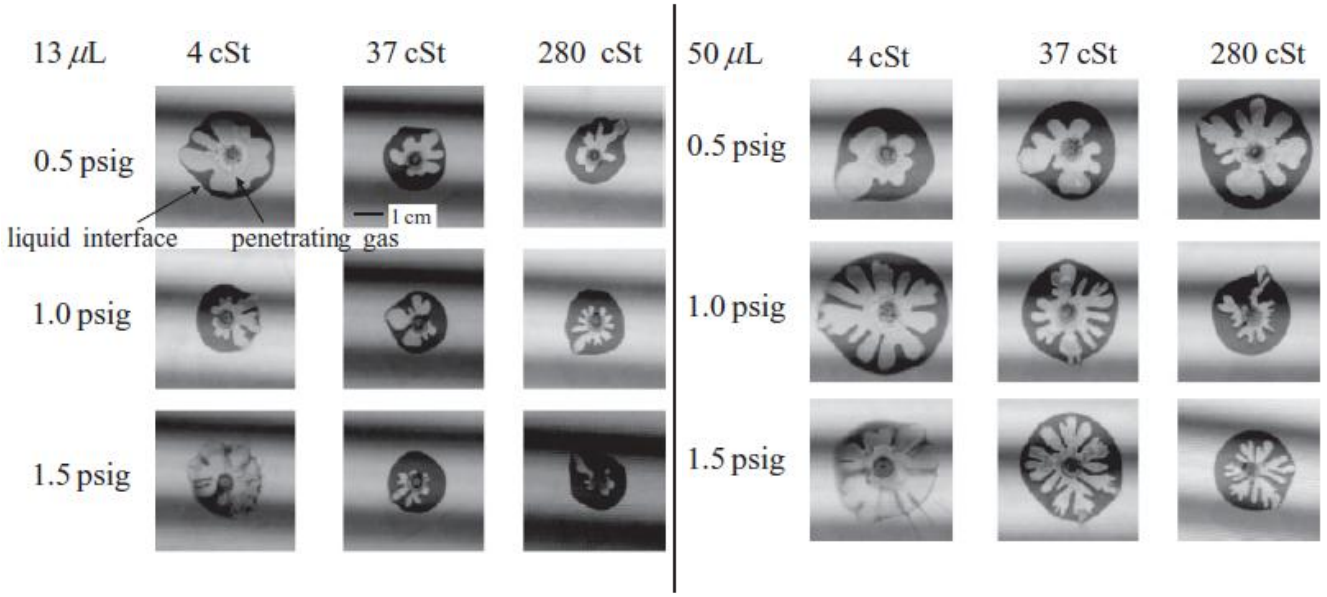

Figure 2.2 *Images of bursting event for drops in a Hele-Shaw cell. The volume for the upper potion of the figure and lower portion, separated by the line, are 13 μl and 50 μl respectively. The viscosity is listed at the top and the pressure on the left hand column.*

The first and second columns of the 13 μl volume experiments show fingering patterns that are qualitatively similar at each pressure. The total cross sectional area at bursting though does not appear similar, with a much larger area in the 4 cSt viscosity and 3.5 kPa experiment, versus the 37 cSt and 3.5 kPa one. The remainder of the experiments in the first and second column do appear to have similar total expanded volumes at bursting. A comparison of the first and second column for the 50 μl experiments reveals similar patterns to those seen in the 13 μl experiments, i.e. similar fingering patterns at each pressure. Comparing experiments with different volumes and for fixed viscosity, there is qualitatively similar fingering behavior at equivalent pressure values. Comparing the two drop volumes for fixed pressure with varying viscosity also shows similar trends of a decrease in the total and gas cross sectional areas at the bursting event.

2.5.2 Quantitative results

Figs. 2.3(a)-2.3(b) shows semi-log plots of the measured gas, and the total cross sectional areas made dimensionless using the constants C_{gas} and C_{tot}, respectively, as functions of elapsed time. The values for the constants are generated from a fit to the equation $A_{gas} = C_{gas}(e^{\omega t} - 1)$ and $\Delta A_{tot} = C_{tot}(e^{\omega t} - 1)$ using the experimental data. The dotted lines are the plots of the function $e^{\omega t}$ for each of the corresponding experiments. The viscosity is 280 cSt in all of the data shown in these two plots with the other operating parameters described in the legend. At early elapsed times there are errors in the image analysis that are displayed by several values of the dimensionless areas being less than unity for a few sets of experimental results shown in Fig. 2.3(a). Comparing the two sets of data, Figs. 2.3(a) and 2.3(b), it appears that the dimensionless gas area has a slightly larger range ($1 \leq A_{gas}/C_{gas} + 1 \leq 10^3$) than the change in the total area ($1 \leq \Delta A_{tot}/C_{tot} + 1 \leq 20$). The largest elapsed times occur for a combination of larger fluid volumes, and small gap spacing.

Figure 2.3(c) shows the data for the normalized average-total film thickness $\bar{h}/b$ versus elapsed time Δt. The film thickness values, each denoted by a symbol described in the legend, correspond to experiments shown in the previous graph where the viscosity is constant in each at 280 cSt. Most of the data for the average film thicknesses reach a steady value prior to

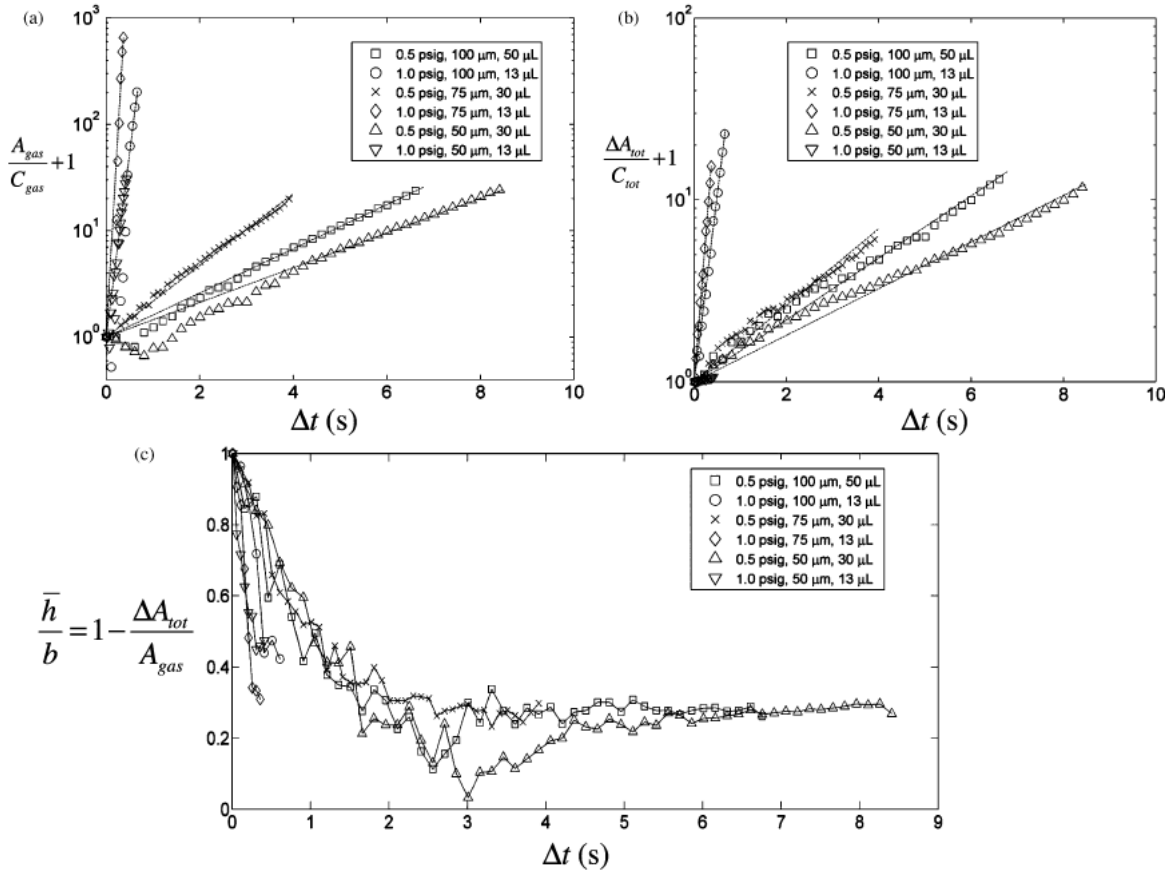

Figure 2.3 *Semilog plot of a)* $\frac{A_{gas}}{C_{gas}}+1$ *and b)* $\frac{\Delta A_{tot}}{C_{tot}}+1$ *versus elapsed time for inlet pressures, fluid volumes and gap spacings as listed in the legend. The viscosity is 280 cSt in each experiment. Lines are drawn through the data representing the best fit curves* $e^{\omega t}$*. c) Plot of normalized total average film thickness* $\bar{h}/b$ *versus elapsed time for inlet pressures, fluid volumes and gap spacings as listed in the legend. The viscosity is 280 cSt in each experiment. Several experiment do not reach an equilibrium while others display small amplitude oscillatory behavior.*

bursting. Some of the points exhibit oscillatory behavior partially due to viscous fingering. But some experiments do appear to show liquid displacements where the ratio of the transient area measurements are indeed oscillatory. All of the data points corresponding to experiments with inlet pressures of 7.0 kPa reach an equilibrium in a much shorter time than the 3.5 kPa inlet pressure experiments while the data points corresponding to the low pressure experiments (3.5 kPa) all seem to reach an equilibrium value after approximately 1 second.

Figure 2.4 displays a summary of the total area and gas area measurements in the form of two plots. Figs. 2.4(a)-2.4(b), are log-log plots of normalized $\Delta P/\mu_L$ versus $Re^* = \omega b^2/\nu_L$ where the Reynolds numbers are determined by using ω derived from the gas and total area data, respectively. Each data set consists of approximately three decades of data with a best fit line also drawn. There is little scatter in the data with a monotonic trend for increasing normalized $\Delta P/\mu_L$ versus $Re^* = \omega b^2/\mu_L$.

Figure 2.5(a) shows a log-log plot of normalized $\Delta P/\mu_L$ versus the bursting time, normalized by a combination of the kinematic viscosity, gap spacing and liquid volume. The data range is fairly robust with the bursting time plotted for over three decades of values. The general trend is a monotonic decrease in the bursting time as either the pressure or gap spacing is increased or by a decrease in the liquid viscosity. The best fit line appears to fit the general trend with several data points from different experiments lying directly on the line.

Figure 2.5(b) shows the log-log plot of normalized $\mu_L \Delta P$ versus measured film height measured using Eq. (2.1), normalized by the plate separation distance. The range of normalized $\mu_L \Delta P$ spans three decades but the average film thickness only spans one i.e. the minimum average film thickness is approximately one-tenth of the gap spacing suggesting that the films span the range of 5-95 μm. The dotted line is the best fit for all of the data with several data points from different experiment lying on the line. The dispersion in the data is fairly uniform at small and large values of the normalized $\mu_L \Delta P$ parameter with an equal number of points above and below the best fit line.

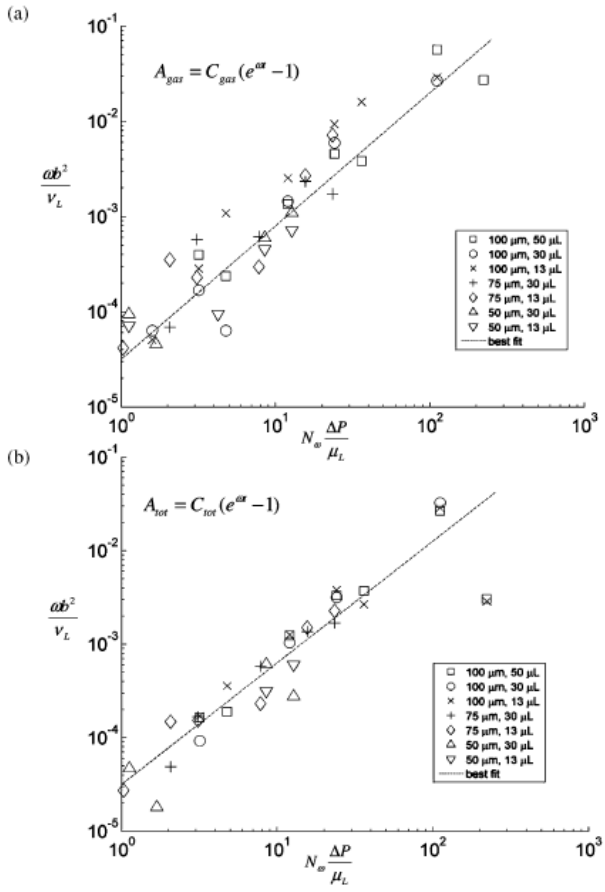

Figure 2.4 *Log-log plots of Reynolds number* $Re^* = \omega b^2/\nu_L$ *versus normalized* $\Delta P/\mu_L$ *where the characteristic rate* ω *is measured using either the transient a) gas or b) total cross sectional area fit to the expression* $C_i(e^{\omega t} - 1)$ *where the* i *represents either the gas gas or total tot area. A best fit line is drawn in each graph.*

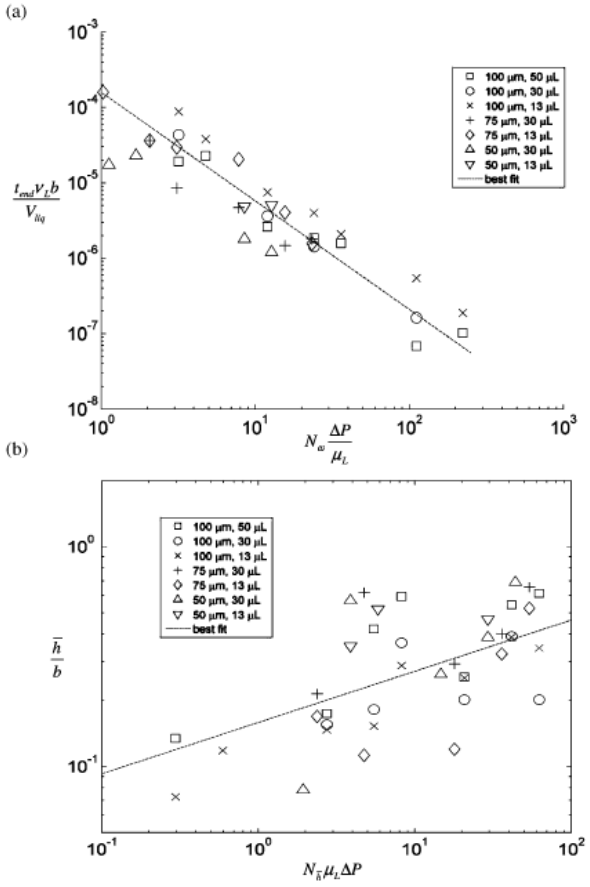

Figure 2.5 *a) Log-log plot of $t_{end}\nu_L b/V_{liq}$ versus normalized $\Delta P/\mu_L$. b) Log-log plot of $\bar{h}/b$ versus normalized $\mu_L \Delta P$. A best fit line is drawn in each graph.*

2.5.3 Discussion

In Figs. 2.3(a)-2.3(b) the lines representing the best fits, $e^{\omega t}$, appear to fit the data very well for the elapsed time range shown. At early times there is clearly some deviation possibly due to errors in the algorithm used to measure the areas but taken as a whole it appears that the plots are linear suggesting that the radial expansion empirical correlations, Eqs. (2.2a-b) are accurate for the range of parameters tested. The results seem to correspond to the pre-wet cell experiments of Carrillo et al (9) since these clearly show exponential behavior. The discrepancy between our results and there's may be due to the fact that the authors plot their data versus a non-dimensionalized function $f(t)$, which is used to capture the transient behavior of the rotating motor, instead of the actual elapsed time as we have done. Another possible reason for the discrepancy is the notion that a pre-wet and dry cell possess different dynamics. Since the less viscous phase fluid displaces the more viscous one then there is some dynamic wetting of the dry-wet region where the liquid and the plates meet. This would suggest that surface tension may in fact be relevant in the results presented here. But since the surface tension does not vary much from one experiment to another then its precise relevance cannot be accurately determined. But the reader should note that Carrillo et al. study a different problem, i.e. the *stable* displacement of a liquid annulus, for which a nearly exact analytical formulation can be drawn. The study presented here reduces to the Carrillo et al. result when the Saffman-Taylor instability is ignored and average quantities are considered. Although the average fronts are circular and hence the average fluid domain is indeed annular, it is not at all certain that the dynamics of these average magnitudes in actual viscous fingering flows should coincide with the dynamics of a liquid annulus studied in (9).

We continue the discussion with results related to the characteristic rate ω. The values for the exponent m used in the expression for ω, Eq. (2.4), based on the gas and total area data are 1.19 and 1.28 and for C_ω are 1.7×10^{-5} and 3.1×10^{-5}, respectively, for the data shown in Figs. 2.4(a)-2.4(b). Therefore our assumption of constant and equivalent characteristic rate ω for the measurements of $A_{gas}(t)$ and $A_{tot}(t)$ appears to be accurate. Also the values for each ω appears to be within 20-30% of unity. The fact that the values are larger than unity suggest

that an additional pressure may need to be included in future studies such as capillary pressure γ/b. Also, a more detailed explanation of the behavior near the penetrating gas-displaced liquid region that includes the curvature of the interface in the plane of the plates may provide more accurate results (Ref. (51) provides a review of relevant studies). This would require more detailed analysis of the fingering wavelength since the curvature is directly related to its value, but this is outside the scope of the present study. The range for the constants, normalized by the gap spacing, are $10,000 < C_{gas}/b^2 < 40,000$ and $2000 < C_{tot}/b^2 < 10,000$. The constants do not change by one order of magnitude and therefore we believe it would be difficult to determine an accurate correlation between them and the variables ΔP and μ_L.

The data for the burst time, shown in Fig. 2.5(a), follows the best fit line fairly well. The bursting time t_{end} is the only empirical expression that appears to involve fluid volume. According to the best fit line, the bursting time, t_{end} is proportional to $\left(\frac{\Delta P}{\mu_L}\right)^{-1.38}$. The absolute value of the exponent is similar to the one determined for the characteristic rate ω suggesting that the product of ωt_{end} is weakly dependent on $\Delta P/\mu_L$ according to the experiments and therefore mostly depend on the volume and b, i.e. $\omega t_{end} \sim \frac{V_{liq}}{b^3}$. Given that $\omega \propto \frac{\Delta P}{\mu_L}$ then the time to burst is approximately $t_{end} \sim O(\frac{\mu_L V_{liq}}{b^3 \Delta P})$ where we have assumed a power of unity for the empirical relationship between ω and $\frac{\Delta P}{\mu_L}$. This relationship though may fail to capture precise bursting times because the velocity of the leading-penetrating interface may dominate, particularly in the deeply non-linear regime of the Saffman-Taylor instability.

The final set of data to discuss are the average film thickness results. The main result is that the film does appear to reach a steady state thickness for our range of parameters according to the data presented in Fig. 2.3(c). In Fig. 2.5(b) the plots for the normalized average film thickness follow the monotonic trend shown by the best fit curve. Given the slope and intercept, the best fit curve yields the expression,

$$\frac{\bar{h}}{b} = 0.15\left(\frac{\mu_L \Delta P}{\rho_L^{1/2}\gamma^{3/2}} b^{1/2}\right)^{0.27} \tag{2.5}$$

for the average film thickness as a function of $\mu_L \Delta P$. Note that the gap spacing appears on both sides of the equation for convenience. Twice the exponent, $2n = 0.54$, is lower than what has been predicted for and observed in other systems using similar measurement technique

(9) but is relatively close in value to other general studies. The film measurement data, as a whole, also does not show asymptotic behavior as the $\bar{h}/b$ reaches a maximum value of unity. But individually the data does appear to show asymptotic behavior, in particular the 100 μm gap spacing with 13 μl and 50 μl drop experiments. Overall, it requires about three orders of magnitude change in the normalized $\mu_L \Delta P$ to yield one order of magnitude change in average film thickness for $0.1 < N_{\bar{h}} \mu_L \Delta P < 100$ according to Fig. 2.5(b). The measurement of thin films of gas (thick liquid films) are a surprising result of the experiments. The results for t_{end} when combined with Eqs. (2.2a) and (2.5), are useful for determining the volume of gas, $V_{gas} = A_{gas}(b - \bar{h})$, that penetrates the liquid droplet as it expands in a radial hele-Shaw cell prior to bursting.

2.6 Conclusion

In this manuscript the displacement of a more viscous phase fluid by a less viscous phase is studied in a radial Hele-Shaw geometry. The less viscous phase fluid is air and the more viscous phase is a mixture of glycerol-water at various concentrations. The air is injected into the liquid phase at constant pressure for three different volumes of liquid and the experiment continues until the gas breaks through the interface. The average film thickness, gas phase and total areas, and bursting time are measured by analyzing images of the experiments.

The experimental results suggest the gas phase and liquid phase areas expand exponentially with respect to time, analogous to (9) for the problem of a fluid displaced in a rotating Hele-Shaw cell. The measured film thicknesses span 5-95% of the the gap spacing over the range of pressures and viscosities. The bursting times appear to follow a monotonic trend and scale with the fluid volume.

In the future it will be beneficial to perform additional experiments varying the surface tension either by using surfactants or other fluids. It also may be useful to perform experiments under non-isothermal conditions to understand more details of the finger formation and fluid displacement in non-ideal systems.

2.7 Acknowledgements

The authors would like to thank G. M. "Bud" Homsy and T. P. Witelski for their insightful comments and suggestions. Useful comments were also provided by a referee that should be acknowledged. The authors would also like to acknowledge the NC Space Grant for supporting this research and for providing undergraduate support for A. R. White.

CHAPTER 3. CO_2 SEQUESTRATION IN A RADIAL HELE-SHAW CELL VIA AN INTERFACIAL CHEMICAL REACTION

A paper published in *Chaos*[1]

Andrew. R. White[2], Thomas Ward[3,4]

3.1 Abstract

In this manuscript experimental data for the displacement of a finite volume of aqueous $Ca(OH)_2$ using CO_2 gas in a radial Hele-Shaw cell will be presented. This chemical reaction is known to generate $CaCO_3$ precipitate along the gas-liquid interface and we seek to understand the influence of the reactive process on fluid displacement. The reactive experiment is compared with the non-reactive case to determine if there is any measurable differences between the two in the range of parameters: CO_2 pressures (1-10% of an atmosphere measured in gage pressure), liquid volumes (either 50 or 70 μl) and $Ca(OH)_2$ concentrations (0, 10 or 20 mM) are studied. Analysis is performed by measuring the displacing fluid area A_{gas} and total fluid area A_{tot} to determine several quantities (gas expansion rate, quasi-equilibrium film rate and value, and presence of fingering instability) used to distinguish the experiments. In general there appears to be little affect of the chemical reaction on most of the measured quantities but certain trends are noticeable in the film formation rate.

[1] *A. R. White, T. Ward. CO_2 sequestration in a radial Hele-Shaw cell via an interfacial chemical reaction.* Chaos ***22**, (2012)*

[2] Graduate Student, Department of Mechanical and Aerospace Engineering, North Carolina State University
[3] Assistant professor, Department of Mechanical and Aerospace Engineering, North Carolina State University
[4] Author for correspondence: thomasw@iastate.edu

3.2 Introduction

The displacement of a more viscous fluid by a less viscous fluid in a porous medium has been studied for many years. For many industries, such as oil recovery, this problem is of great interest since displacement of the oil phase by a less expensive, and less viscous fluid phase provides a cost effective means for enhancing recovery. The typical model system consists of a point source introducing the less viscous phase at a constant flow rate into a porous medium containing the more viscous one. A convenient means to represent this system in a laboratory setting is with a Hele-Shaw cell that consists of two parallel-circular plates with a gap spacing much smaller than the radius. The advantage is that the flow occurs mainly in the radial direction making experimental visualization and analysis less daunting.

The radial Hele-Shaw cell has allowed researchers to study the fundamental process of fluid-fluid displacement and has elucidated some of its shortcomings. First, fingers of the less viscous fluid form and penetrate the more viscous fluid rather than displace it evenly (13; 15; 16; 18; 26; 31; 41; 42; 43; 44; 45; 51). This phenomenon, known as the Saffman-Taylor instability (13), is a major problem for oil recovery and its severity varies based on system parameters such as fluid properties, geometry and driving force. Second, there is also a liquid film that is left on the porous media wall which further reduces recovery. Fluid displacement becomes even more complex as a chemical reaction occurs at the interface of the two fluids. In this manuscript we discuss the onset of fingering instability and film formation in a radial Hele-Shaw cell in the presence of an environmentally relevant chemical reaction

Consider the cases of oil recovery where CO_2 gas is sometimes used to displace viscous crude oil (35). After being used for recovery it is desirable to sequester the CO_2. One well known method for carbon sequestration is to exploit the reaction of CO_2 and $Ca(OH)_2$ which, in the presence of water, forms a $CaCO_3$ precipitate (57; 58; 59). This scenario is of interest to fields such as environmental sciences where the ability to efficiently capture and store CO_2, perhaps after being used for oil recovery, is desired. This reaction already occurs naturally, albeit slowly (60). If slightly pressurized CO_2 were injected into an aqueous solution of $Ca(OH)_2$ in a porous medium, such as a nearly depleted oil well, then the ensuing reaction could permanently store

the carbon in solid $CaCO_3$ deposits.

We study this system by presenting data for the expansion of pressurized CO_2 gas into a finite volume of aqueous $Ca(OH)_2$ in a radial Hele-Shaw cell. We vary the inlet CO_2 pressure at low values (1-10% of an atmosphere measured in gage pressure) and also the $Ca(OH)_2$ concentration (0, 10 or 20 mM) in a finite volume of water (either 50 or 70 μl). This chemical reaction occurs along the gas/liquid interface producing the solid precipitate $CaCO_3$. The solubility of $CaCO_3$ is heavily dependent upon the concentration of CO_2 in the aqueous phase i.e. the pressure (61).

The proposed Hele-Shaw system (constant pressure injection and finite liquid volume) represents a deviation from the traditional radial Hele-Shaw cell problem. Recently much work has been done with studying the effect of chemical reactions on the Saffman-Taylor instability in miscible and immiscible liquid-liquid systems with constant flow rate driven or reaction driven displacement (27; 28; 29; 30; 62). The authors believe that the constant pressure injection may represent a condition that is more easily recreated in the field particularly if the displacing fluid is a gas.

As for the finite liquid volume it allows for several analytical tools. First, it allows for the determination of the transient film thickness, $h(t)$, by measuring the displacing and total fluid areas, denoted A_{gas} and A_{tot}, respectively, where A_{tot} is the cross-sectional area occupied by both the gas phase and liquid phase. We also study the onset of fingering by visually comparing the images as the parameters are varied from one experiment to the next. Second, we are able to measure the quasi-equilibrium film value h_∞ (the film thickness prior to bursting, see Fig. 3.1 for schematic) which is revealed as the last recorded value of $h(t)$ measured where $\dot{h} = 0$ (overdot denotes a derivative with respect to time). Lastly, the rate of quasi-equilibrium film formation ω_{film} (also abbreviated as the film formation rate) is also compared between the experiments. This value represents the negative time constant from a curve fit of the transient film thickness data to an exponential function. After measuring these three values for each experiment we further analyze the system by correlating the values to the system parameters (CO_2 pressure and $Ca(CO)_2$ concentration). In general we suspect that the optimal system for simultaneously displacing aqueous $Ca(OH)_2$ and converting CO_2 to $CaCO_3$ would be the

system which produces: 1) no fingering (stable displacement), 2) has a slow gas expansion rate to provide ample time for the chemical reaction, 3) produces thin films so that the chemical reaction occurs mostly along the gas-liquid interface and 4) reaches a quasi-equilibrium film thickness in a relatively short amount of elapsed time.

The finite volume analysis that is key to understanding the experimental data was first studied in 1999 by Carrillo et al (9). In their experiments the authors studied fluid displacement driven by axial rotation in a radial Hele-Shaw geometry in the limit of low Reynolds and Rossby numbers. A study combining experiments and analysis of a similar system and for a wide range of rotation rates was performed in 2006 by Álvarez-Lacalle et al, (52). The finite liquid volume, denoted V_{liq}, allowed tracking of the outer and inner annular liquid radii, then with knowledge of the initial radius the authors determined a steady film thickness where they show that the residual film was less than 10% of the gap spacing. Similar to the analysis of Carillo et al we have also developed expressions for displacement rates and film thickness based on measurements of the penetrating and displaced fluids' cross sectional areas.

In the next section we present a detailed discussion of the chemical reaction of pressurized CO_2 and $Ca(OH)_2$. We also discuss our method for measuring the drop expansion rate, film formation rate and the film thickness. Variations in these results as a function of the input parameters (inlet CO_2 pressure and reactant concentrations) may lead to an understanding of the optimal conditions for CO_2 sequestration based on the outputs (presence of instability, expansion rate, quasi-equilibrium film thickness and quasi-equilibrium film formation rate). Following these discussions are the experimental materials followed by both a qualitative and quantitative analysis of the data. Finally we will make conclusions and make recommendations for future experiments based on the results.

3.3 Analysis

Consider an initially-nearly cylindrical Newtonian droplet containing aqueous $Ca(OH)_2$, of radius $a_2(t = 0) =$ constant, concentrically confined between two parallel circular plates at a distance b apart where $b \ll \ell_c$ (see Fig. 3.1 for illustration) or equivalently the Bond number $Bo^* = (b/\ell_c)^2 \ll 1$ where $\ell_c = \sqrt{\gamma/\Delta\rho g}$ is the capillary length. $\cdot^*$ are used to denote

dimensionless variables throughout this manuscript. Here γ denotes the surface tension, g the gravitational acceleration constant and $\Delta\rho = \rho_l - \rho_g$ is the difference between the liquid and gas density, respectively. In the limit $Bo^* = (b/\ell_c)^2 \ll 1$ we can neglect gravitational effects and assume that the film thicknesses are equal on the top and bottom plates. The other relevant liquid properties are the absolute and kinematic viscosities μ_L and $\nu_L = \mu_L/\rho_L$, respectively. Additional relevant dimensionless parameters are the Reynolds number $Re^* = \frac{\omega_{gas} b^2}{\nu_L}$ and the capillary number $Ca^* = \frac{U\mu_L}{\gamma}$ where U is a measurement of the the displacement speed as discussed previously (7). At time $t > 0$ CO_2 gas is injected into the center of the parallel plates at a constant pressure P_{gas} where the gage pressure is written as $\Delta P = P_{gas} - P_{atm}$ with P_{atm} equal to atmospheric pressure. The injection pressure is low i.e. $\Delta P/P_{atm} \ll 1$ so that the gas density and temperature are both considered constant throughout the displacement process (53). Surface tension, γ, may not be negligible under these conditions considering that the pressure is low enough such that $\Delta P \sim O(\gamma/b)$. As the pressure is increased the formation of the typical Saffman-Taylor fingering instability becomes present at earlier elapsed times.

3.3.1 Interfacial chemical reaction

The chemical reaction to produce $CaCO_3$ can be viewed in two steps. First, CO_2 must dissolve into the aqueous phase to form carbonic acid (60; 63),

$$H_2O_{(\ell)} + CO_{2(g)} \leftrightarrows H_2CO_{3(aq)}.$$

This reaction is slow, reversible, and limited greatly by the ability of CO_2 to dissolve in water as dictated by Henry's Law (63). Higher pressures and temperatures create favorable conditions for CO_2 dissolution and the carbonic acid production. Second the $Ca(OH)_2$ reacts with the H_2CO_3 to form $CaCO_3$ and two water molecules (60; 63),

$$Ca(OH)_{2(aq)} + H_2CO_{3(aq)} \rightarrow CaCO_{3(s)} + 2H_2O_{(\ell)}.$$

This step is limited first by H_2CO_3 production and then by $Ca(OH)_2$ solubility, which becomes more favorable at lower pressures and temperatures. A complete analysis of the second

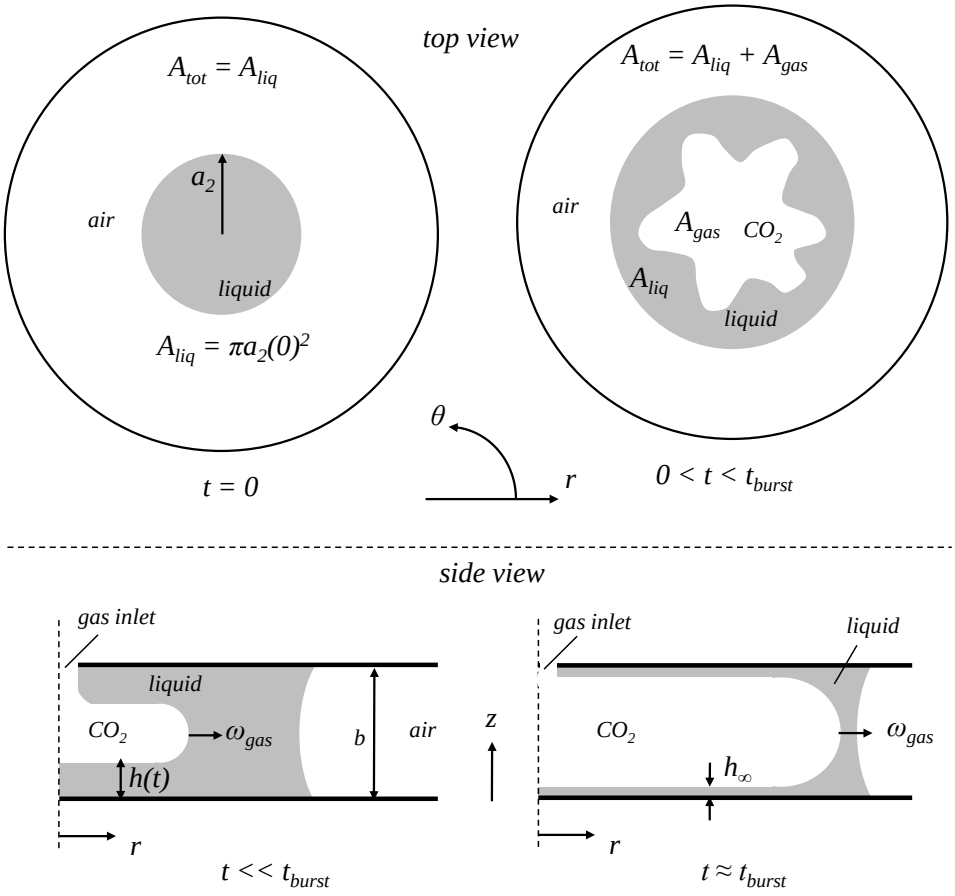

Figure 3.1 *Top and side view of the problem schematic and experimental setup. The top view shows the initial drop configuration at time $t = 0$ and the proposed configuration at later times where a typical fingering instability develops in the azimuthal direction. The side view shows the gas penetration at early and late times. In particular the side view visualizes the analytical tools used in this manuscript: 1) gas expansion rate in the radial direction ω_{gas}, 2) transient film thickness $h(t)$ as the gas displaces the liquid and 3) the quasi-equilibrium film thickness h_∞. Note the schematic is not drawn to scale.*

step requires writing more chemical reaction equations that can involve reversible reactions (63) but these are not relevant for our study.

3.3.2 Characteristic rate relationships and film thickness equation

As discussed in the introduction there are three analytical tools, presented below, that will be used to characterize each individual experiment. Each one is based upon measurement of experimental data. In particular we calculate the transient gas area, A_{gas}, and total area, A_{tot}, as measured from above by analyzing sequential images of the expansion process.

3.3.2.1 Gas expansion rate, ω_{gas}

The authors previously postulated empirical correlations for the expansion rates of the gas and total areas of the forms (7)

$$A_{gas}(t) = C_{gas}\left(e^{\omega_{gas}t} - 1\right), \text{ and} \tag{3.1a}$$

$$\Delta A_{tot}(t) = C_{tot}\left(e^{\omega_{tot}t} - 1\right) \tag{3.1b}$$

respectively, where C_{tot} and C_{gas} are constants and $\Delta A_{tot}(t)$ is the difference between the total area at a specific time, $A_{tot}(t)$, and the initial area of the drop. For this study we focus attention on the gas expansion rate. In the limit $Re^* \ll 1$ we previously used a general correlation between ω_{gas} and $\Delta P/\mu_L$ for comparison with experiments and showed that it is a power law relation (7). The viscosity is not varied in these experiments but we assume a similar power law correlation with respect to the gas pressure,

$$\omega_{gas} = C_\omega \Delta P^m \tag{3.2}$$

where m and C_ω are to be determined by curve fits to experimental data. Values for the exponent may be dependent upon the chemical reaction rate.

3.3.2.2 Quasi-equilibrium film thickness, h_∞

We define the quasi-equilibrium film thickness h_∞/b as the film thickness where $\dot{h}(t) = 0$ prior to bursting. The quasi-equilibrium film is derived from the measurement of the transient film which is made by using the expression,

$$\frac{h(t)}{b} = 1 - \frac{A_{tot} - \pi a_2^2(0)}{A_{gas}}, \tag{3.3}$$

where a_2 is the initial radius of the drop as shown in Fig. 3.1. This transient value is the sum of the film on the top and bottom plate. The quasi-equilibrium value, h_∞/b, is measured by approximating $\dot{h}(t) \approx \Delta h/\Delta t = 0$ which occurs prior to bursting. An average of the last few transient $h(t)$ values has provided a good approximation for h_∞ in these studies.

As for a relationship between the gas pressure and the quasi-equilibrium film thickness an empirical relationship for Ca^* was derived by considering the first two non-zero terms in the Taylor expansion of the average gas displacement (7). Since in this manuscript we only vary the pressure we assume that our film thickness is directly proportional to the pressure to some power ℓ or,

$$\frac{h_\infty}{b} = C_\infty \Delta P^\ell \tag{3.4}$$

where ℓ is to be determined by the curve fitting of experimental data. Previously we saw that the power ℓ was approximately 0.25 (7). Since the viscosity is not varied in the experiments then the actual range of data will be much smaller and may produce another power similar to the different powers of Ca[8] (i.e. $h_\infty \propto Ca^q$) that exist for different ranges of film thickness in bubbles displacing liquid in tubes (64; 48; 46; 47).

3.3.2.3 Quasi-equilibrium film formation rate, ω_{film}

The transient $h(t)$ data provided later in this manuscript reveal that the evolution of the film thickness, prior to bursting, is nearly exponential. This seems reasonable given that $h(t)$ is a function of the gas and total area which both evolve exponentially. But the gas and total area expansion rates are based on correlations, since developing analytical theory for

radial displacements that involve finger formation is non-trivial. Nonetheless, similar to the gas and total areas, we've determined that the film evolves nearly exponentially according to the expression,

$$\frac{h(t) - h_\infty}{b - h_\infty} = e^{-\omega_{film} t}. \tag{3.5}$$

This information was not provided by the authors in previous studies. Similar to the other analytical tools, and from the experiments (discussed later in the manuscript) the authors assume that the rate of formation for the quasi-equilibrium film also has a power law relationship with respect to the inlet pressure,

$$\omega_{film} = C_{film} \Delta P^n. \tag{3.6}$$

The exponent n will also be determined experimentally.

3.4 Experiments: materials and procedure

A Hele-Shaw cell was created using two circular acrylic plates with a diameter of 10.2 cm (4 *in.*) and a gap spacing of 100 μm using plastic shims (AccuTrex) as shown in Fig. 3.2. In order to inject carbon dioxide into the cell a standard 8-32NC thread was tapped in the center of one plate and a plastic pipe fitting (Cole Parmer) with an inner diameter of 2.4 mm (3/32 *in.*) was inserted. Carbon dioxide was stored in a 5.5 MPa tank and was connected to the transducer with tubing that had an inner diameter of 6.35 mm. The inlet gas pressure was controlled using a pressure transducer (Marsh Bellofram) and a function generator (Agilent) to provide a precision step function. The supply valve on the gas tank was opened such that a pressure of at least 140 kPa was created at the input of the transducer prior to any signal being sent by the signal generator. Current from the function generator in the range of $4.6 < I < 5.3$ mA was supplied to the transducer to yield pressure outputs in the range of $1.0 \leq \Delta P \leq 3.10$ kPa ($0.15 \leq \Delta P \leq 0.45$ psig) in steps of 0.35 kPa (0.05 psig). This provides $Re^* = O(.01)$ and $Bo^* = O(.001)$. For Bo^* calculation an acrylic-water surface tension of $\gamma = 35\ mN/m$ was used

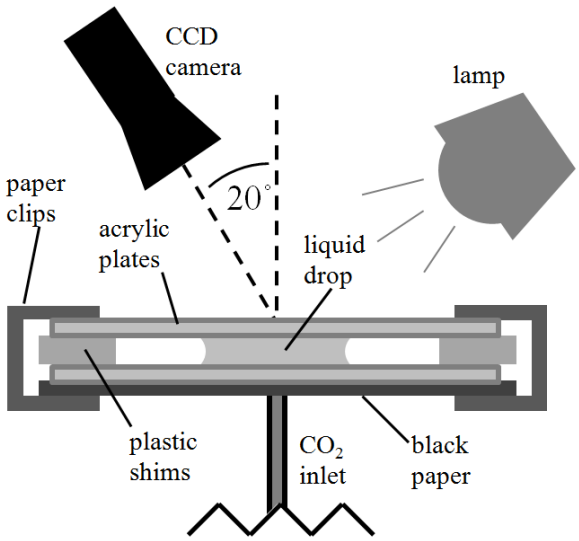

Figure 3.2 *Side view of the experimental setup of the Hele-Shaw cell.*

(65). Calcium hydroxide (Fisher Scientific) concentrations of 0, 10 and 20 mM in water were used as the experimental liquids.

A drop with a volume of 50 or 70 μL was placed at the center of the Hele-Shaw cell by using an Eppendorf syringe. After the transducer received the signal at least three seconds elapsed before any gas was allowed to flow upstream into the Hele-Shaw cell. This was accomplished by placing a manually operated ball valve between the transducer and Hele-Shaw cell. A CCD camera (PixeLINK) was used to capture video of the experiment at 100 or 200 fps looking 20 degrees from normal to the cell from above to reduce complications from glare on the Hele-Shaw cell. The viewing angle distorted the video in one dimension and was compensated for by multiplying that dimension by $cos(20°)$ during analysis. To contrast the liquid drop from the surrounding gas the drop was illuminated at an angle with a halogen lamp, taking advantage of the differing indices of refraction of the liquid and gas. The video captured the experiment from just before the initial injection of the carbon dioxide until either the drop burst or it expanded outside of the viewing area. "Burst" here does not imply a catastrophic event but rather the first instance that the inner gas-liquid boundary becomes discontinuous. Run times for the experiments range from less than 30 up to more than 1000 ms depending on gas pressure, providing a minimum of approximately 10 experimental frames for $1.00 \leq \Delta P \leq 2.75$ kPa and

a minimum of 5 experimental frames at 3.10 kPa. Due to the lack of experimental frames per experiment for 3.10 kPa these experiments are not included in the quantitative analysis. In total 96 experiments were performed with 32 experiments for each concentration of $Ca(OH))_2$. For each concentration 2 iterations were performed at 1.00 and 1.35 kPa, 4 were performed at 1.70 kPa, and 6 were performed for $2.05 \leq \Delta P \leq 3.10$ kPa. Fifteen experiments used 50 μL drops while the rest used 70 μL, however the small difference in volume does not affect the results significantly.

A MATLAB program was used to precisely analyze the frames of each video. For each frame the annular area (area occupied by the liquid), the gas area (area occupied by the injected CO_2) and the total area were measured by counting pixels of different intensities. There were some initial pixels that were always present due to the pixel intensity of the gas phase inlet and therefore produced a non-zero initial area for the gas phase. Only the frames from the initial injection of air until the first burst were analyzed, defined as the event in which the liquid-CO_2 interface becomes discontinuous for the first time and CO_2 is allowed to escape, t_{burst}. The area data was used to produce a transient average film thickness estimated using Eq. (3.3).

3.5 Experiments: results and discussion

3.5.1 Qualitative results

Figure 3.3 shows the drop expansion patterns representative of different concentrations of $Ca(OH)_2$ and different CO_2 pressures. Each image in the figure depicts a 70 μL drop just before it bursts. The Saffman-Taylor instability is less pronounced and even non-existent for experiments performed at low pressures but clearly visible as the pressure increases. The first identifiable fingers seem to form at 2.05 kPa and grow in numbers as pressure increases. By 2.75 and 3.10 kPa anywhere between 5 and 10 fingers are present. The fingering patterns are similar for all concentrations for fixed pressure. It is important to note that, though Fig. 3.3 does provide a good representation of the fingering patterns observed, experiments under the same pressure and concentration sometimes showed slightly dissimilar fingering patters i.e. number of fingers, etc. would vary. This typically occurred at pressures of 2.05 kPa and abovel

or those where fingering instabilities are present. As will be shown in the proceeding analysis, considerably more error was found in the quantitative analysis for experiments at 2.05 kPa and above. The authors suspect the presence of the Saffman-Taylor instability is a leading reason for this error.

A noticeable difference in the some of the images in Fig. 3.3 is the appearance of a ring of residue. This residue only appears in experiments with 10 or 20 mM concentrations and at pressures at 2.05 kPa and above such as at 2.05 kPa and 10 mM $Ca(OH)_2$. After experiments exhibiting this residue the Hele-Shaw cell was disassembled and the presence of residue was verified, however the composition of the residue was not investigated.

Even though the drop expansion sometimes includes fingering instabilities, particularly at the higher pressures, the total drop area expands in a radial pattern; however in some cases the expansion pattern was less radial such as at 1.70 kPa and 20 mM $Ca(OH)_2$ and 2.40 kPa with 10 mM $Ca(OH)_2$. This could be caused by surface roughness in the acrylic (our gap spacing is 100 μm where surface roughness may not be neligible) or in the initial shape of the liquid drop. While an attempt was made to minimize this behavior throughout the course of the research these issues may account for some of the error present in the proceeding quantitative analysis.

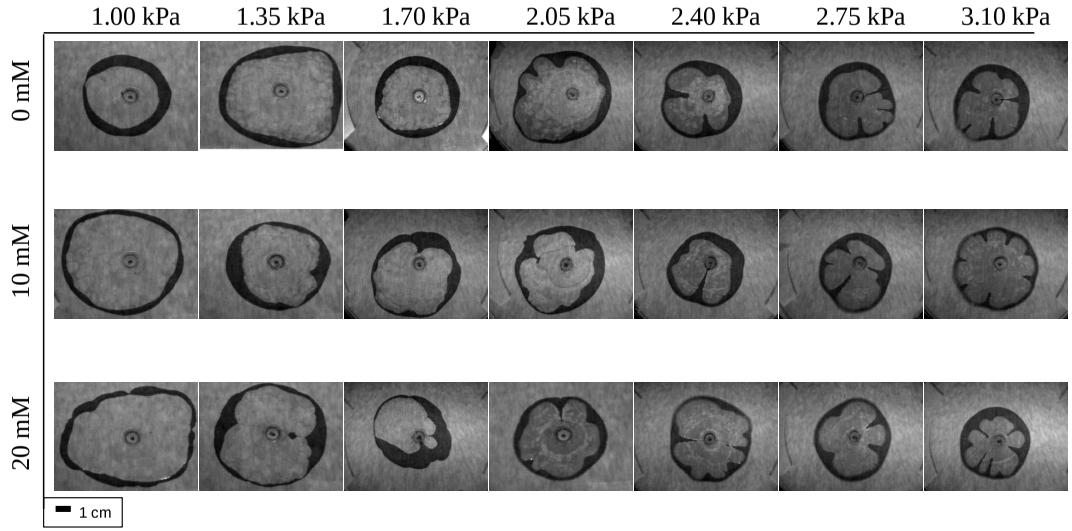

Figure 3.3 *Images of drop expansion just before bursting for different experimental conditions using water with $Ca(OH)_2$ concentrations of 0, 10 and 20 mM. The images represent inlet CO_2 pressures ranging from 1.00 - 3.10 kPa penetrating a 70 μL liquid drop. The $Ca(OH)_2$ concentrations are listed in the left-hand column and the pressures in the top row of the figure. A length scale applicable to each image in the figure is shown in the bottom left.*

3.5.2 Transient gas area and film thickness

Figures 3.4(a) and 3.4(b) show semilog plots of the measured gas area, nondimensionalized by dividing by C_{gas}, versus elapsed time for 0 mM and 20 mM $Ca(OH)_2$ drops, respectively. The values for C_{gas} are determined by fitting the experimental data to Eq. 3.1a while simultaneously determining the gas expansion rate, ω_{gas}. The solid lines plotted against the data are plots of $e^{\omega_{gas}t}$. All of the data fit the exponential model very well for the duration of the experiment. For a few select plots in each figure an image of the drop expansion at the last timestep is inserted. These images highlight the discovery that the exponential behavior of the drop expansion is unaffected by the presence, or lack, of a fingering instability.

Figure 3.5 shows a semilog plot of the estimated film thickness, determined using Eq. 3.3, versus elapsed time for the expansion of a 10 mM $Ca(OH)_2$ from selected experiments. Here the film thickness is normalized by using the quantity $\frac{h(t)-h_\infty}{b-h_\infty}$. Each set of data is fit with a line that was determined by using Eq. 3.5. Similar to the transient gas area plots, the exponential fit works well here.

3.5.3 Quasi-equilibrium film thickness

The normalized quasi-equilibrium film thickness versus pressure is shown in Fig. 3.6. Each point plotted in the figure is the average of all data points at a given concentration and pressure. Error bars are included representing one standard deviation above and below these average values. The normalized thickness range between 0.04 and 0.16, representing a total film thickness between 4 and 16 μm within the 100 μm gap. As a whole the film thickness appears to increase linearly with pressure. The large error bars make it impossible to discern a trend in the data across different concentrations of $Ca(OH)_2$. The gas sometimes forms fingers at early elapsed times, causing the bursting event to happen at different times even at similar pressures and concentrations.

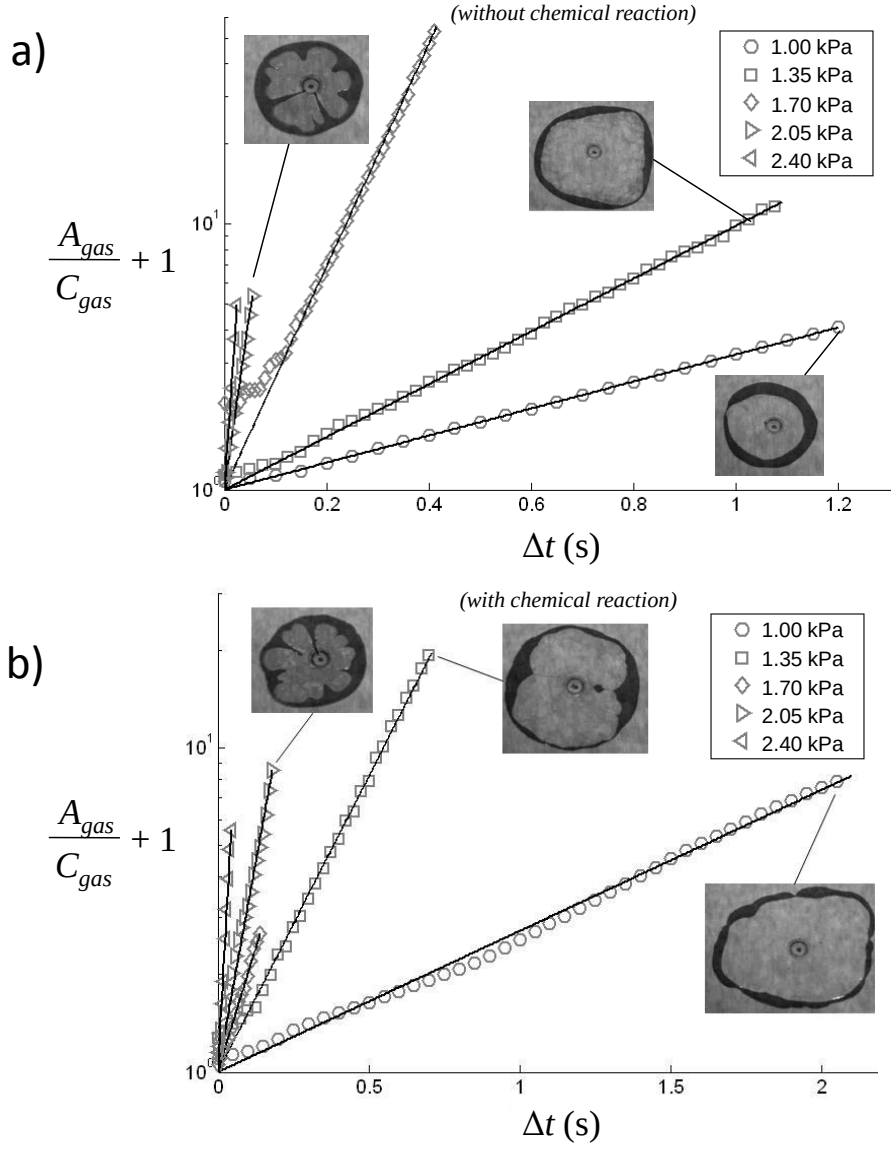

Figure 3.4 *Semilog plots of* $\frac{A_{gas}}{C_{gas}} + 1$ *vs elapsed time for liquid drops with (a) no* $Ca(OH)_2$ *and (b) 20 mM* $Ca(OH)_2$ *experiencing penetrating* CO_2 *pressures indicated in the legend. Plots for each pressure represent a single experiment with no averaging. Lines are drawn through each data set representing the best fit curves of the form* $e^{\omega_{gas} t}$*. Images of the drop expansion just before the bursting event for select pressures are included and correspond to the data set to which they indicate.*

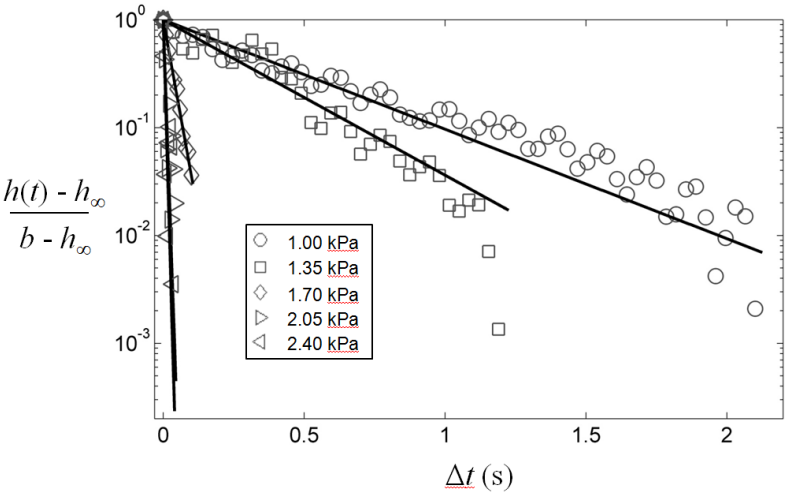

Figure 3.5 *Semilog plot of* $\frac{h(t)-h_\infty}{1-h_\infty}$ *vs elapsed time for liquid drops with 10 mM* $Ca(OH)_2$ *experiencing penetrating* CO_2 *pressures as indicated in the legend. Plots for each pressure represent a single experiment with no averaging. Lines are drawn through each data set representing the best fit curves of the form* $e^{-\omega_{gas}t}$.

3.5.4 Gas area expansion and film formation rates

Using Eq. 3.1(a) and 3.1(b) values for ω_{gas} and ω_{film} were found for each experiment and plotted versus pressure in Fig. 3.7(a) and 3.7(b), respectively. The data points plotted in each figure represent average values for each combination of pressure and $Ca(OH)_2$ concentration. Error bars are included in each figure which represent one standard deviation above and below the mean. Comparing the two figures it appears the range of gas area expansion rates, roughly $1 \leq \omega_{gas} \leq 50$, is less than the range of film formation rates, roughly $3 \leq \omega_{film} \leq 200$, by a factor of between 3 and 4. While there is this discrepancy in the magnitude of the rates the two figures show similar exponential trends with the rates collapsing at $P < 2.05$ kPa.

While large error bars are shown in both figures at 2.05 kPa and above, this presents an interesting result. Experiments at 1.70 kPa and below, which show little to no fingering as depicted in Fig. 3.3, have considerably more consistent expansion rates and film formation rates than experiments at higher pressures which do have pronounced fingering patterns. Two

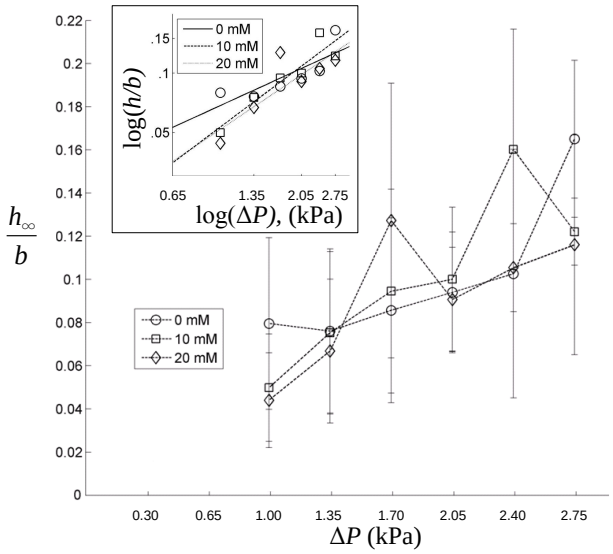

Figure 3.6 *Plots of the average quasi-equilibrium film thickness for pressures 1.00 < ΔP < 2.75 kPa and concentrations as indicated in the legend. Error bars representing one standard deviation above and below the mean are also plotted. An inset includes the best fit to Eq. 3.6.*

examples of typical fingering patterns are shown as insets in Fig. 3.7(a) to further highlight this result.

Unfortunately the large error bars make it difficult to compare the expansion rates and film formation rates at different concentrations of $Ca(OH)_2$. At the three lowest pressures differences in the average rates are very small with overlapping error bars. At higher pressures in Fig. 3.7a differences in the average rates are more pronounced but inconsistent relative to $Ca(OH)_2$ concentration, making it difficult to remark on differences caused by $Ca(OH)_2$. However in Fig. 3.7(b) the average film formation rates for drops without $Ca(OH)_2$ clearly tend to be smaller than drops with 10 or 20 mM $Ca(OH)_2$.

3.5.5 Discussion

The qualitative analysis of the data provides insight into optimal conditions for displacement in the presence of a chemical reaction, as described earlier. First Fig. 3.4(a) and 3.4(b) show

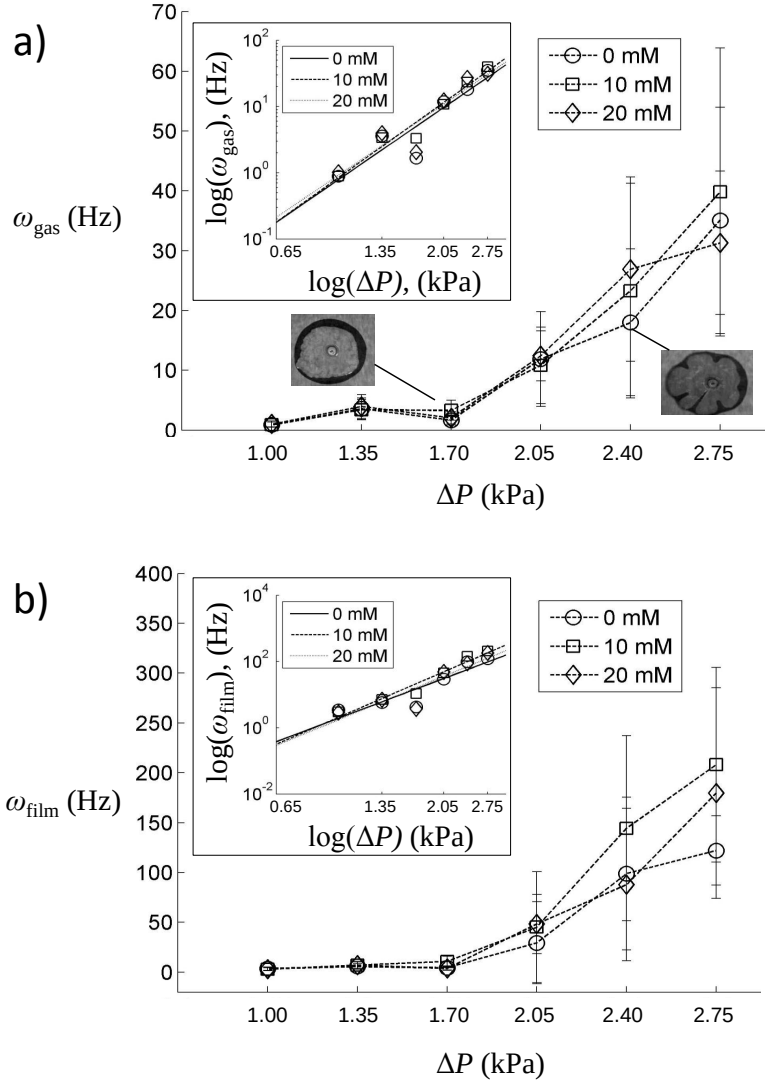

Figure 3.7 *Plots of (a) average gas area expansion rates and (b) average film formation rates for pressures 1.00 < ΔP < 2.75 kPa and concentrations as indicated in the legend. Error bars representing one standard deviation above and below the mean are also plotted. In (a) an inset includes the best fit to Eq. 3.2 and in (b) an inset includes the best fit to Eq. 3.5.*

how the empirical model suggested in Eq. 3.1(a) is fit to the transient gas area data. In fact the gas area as a function of time, $A_{gas}(t)$, is in very good agreement with the form $A_{gas}(t) = e^{\omega_{gas}t} - 1$ even when no fingering instabilities are present. This suggests that the Saffman-Taylor instability is not the root cause for the exponential nature of the pressure-driven expansion of a liquid drop by a gas phase. Perhaps surprisingly, this fact is also true whether or not any $Ca(OH)_2$ or chemical reaction is present in the system. Fig. 3.5 also shows that the transient film thickness, $h(t)$, agrees well with the empirical model in Eq. 3.5 where the film is hypothesized to form like $\frac{h(t)-h_\infty}{b-h_\infty} = e^{-\omega_{film}t}$.

Figure 3.7 digs deeper into the analysis, revealing expansion rates for the area occupied by CO_2 and formation rates for the residual film. The rates in both sets of data collapse below 1.70 kPa and increase after. Applying the correlation for the gas expansion rate in Eq. 3.2 the exponent m is 3.63, 3.78 and 3.58 with C_ω = 770, 1100 and 820 Hz/psig^{-}m for 0, 10 and 20 mM concentrations, respectively. Similarly the exponent n in Eq. 3.4 for the film formation rate is 3.99, 4.57 and 4.37 with C_{film} = 3770, 12100 and 6980 Hz/psig^{-}n for 0, 10 and 20 mM concentrations. Comparing rates in Fig. 3.7(a) and 3.7(b) the film tends to form on a scale three to four times shorter than the drop expands.

Over the range or pressures tested the drop expansion rates for 0, 10 and 20 mM $Ca(OH)_2$ were similar. While at some pressures the 0 mM drops expanded slower, this was not a universal result. Therefore there is no clear dependence of the chemical reaction on the expansion rate. More experiments should be done with more concentrations of $Ca(OH)_2$, higher pressures and larger drop volumes before a definitive conclusion can be reached.

In contrast to Fig. 3.7a, Fig 3.7b does show some differences in regards to $Ca(OH)_2$ concentration. While the film formation rates for all concentrations are roughly similar at pressures below 1.70 kPa, the film formation rates are higher for drops with 10 or 20 mM $Ca(OH)_2$ than drops with no $Ca(OH)_2$ at 2.05 kPa and above. This result could be explained by a potential change to liquid properties as products from the chemical reaction are introduced to the system along the gas-liquid interface.

Another interesting result that comes from Fig. 3.7 is the presence of large error bars at 2.05 kPa and above. The three lowest pressures have considerably smaller standard deviations for

both film formation rates and drop expansion rates. Looking at Fig. 3.3 and the inset images in Fig. 3.7(a) it is clear that these lowest pressures produced little to no fingering instability, while the three highest pressures showed pronounced fingering. It is likely not a coincidence that the onset of the Saffman-Taylor instability coincides with larger errors in the results.

The estimations for film thickness based on Eq. 3.3 are shown in Fig. 3.6 and highlight a slight trend of increasing film thickness with increasing pressure where the exponent ℓ in Eq. 3.6 is 0.63, 1.03 and 0.92 with C_∞ = 0.23, 0.38 and 0.30 psig$^{-\ell}$ for 0, 10 and 20 mM concentrations, respectively. The film thickness varies between 4 and 18 μm in the 100 μm gap, similar to the films of about 10% of the gap spacing observed by Carrillo et al (9). Unfortunately it is impossible to pick out trends of film thickness versus concentration of $Ca(OH)_2$.

Qualitatively the experiments exhibit similar patterns versus pressure for the three concentrations of $Ca(OH)_2$ shown in Fig. 3.3. In general this is not surprising since the liquid viscosity and density are not expected to change greatly between the concentrations. The authors have shown previously that increases in the penetration rate leads to a more pronounced fingering instability, and these new results agree (7).

In summary there does not appear to be any noticeable different in the onset of fingering when the chemical reaction is present. This is a welcome result since stable patterns tend not to burst as quickly as a system with many fingers (7). As for the measurable quantities there are slight deviation in the gas expansion rate and film thickness but, again, there is no clearly discernable difference over the range of pressures and concentrations studied. The one measurable quantity that does appear to show differences is in the film formation rate. Clearly the presence of the chemical reaction produces faster forming films (faster quasi-equilibrium film formation) as the CO_2 pressure increases. But the separation from the experiments without chemical reaction occur at higher pressure so they do not overlap with stable displacements (no observed fingering).

3.6 Conclusion

Radial displacement of a viscous liquid by a less viscous fluid in a Hele-Shaw cell is a technically challenging problem. Most previous studies focused on constant injection of the

less viscous fluid phase into a completely filled Hele-Shaw cell. In this manuscript we presented results for the *constant pressure* injection of carbon dioxide into a finite volume of water that contains calcium hydroxide. The carbon dioxide and aqueous calcium hydroxide can form the precipitate calcium carbonate with the proper operating conditions.

Ideally the chemical reaction would happen such that all of the aqueous calcium hydroxide is converted into calcium carbonate precipitate making this process ideal for sequestration. But there are several barriers to efficient conversion and these are split between the chemical reaction dynamics and the physics of the fluid displacement. Since the CO_2 is a gas it must first dissolve into the water and form carbonic acid before the reaction can proceed. This is more efficient at higher pressure, but using high pressure will reduce the contact time of the two phases since the finite liquid volume will ultimately burst at a shorter elapsed time. High pressures also produce thicker films on the walls of the Hele-Shaw cell which are also barriers to transport as the gas must dissolve into the liquid. Furthermore, the speed at which the film forms and reaches a quasi-equilibrium may be effected by the reactants and products.

The experiments that were performed consisted of two acrylic disks approximately 10 cm in diameter. The CO_2 gas is injected at pressures of approximately 1.0 to 3.1 kPa, with calcium hydroxide concentration of 0, 10 or 20 mM. With our finite liquid volume we were able to analyze film thickness and rate constants for both the gas expansion and film formation. Both clearly show some dependence upon the chemical reaction with more salient effects on the film formation rate.

In the future it will be useful to perform additional experiments at higher pressures to confirm that the film thickness indeed has some bearing on reaction dynamics. There are also other reactants that may allow for more rapid conversion of the CO_2 and it will be beneficial to investigate their applicability. Some involve using buffer solutions to increase the pH which increases the solubility of the calcium hydroxide. Lastly, there are robust and well-established techniques for measuring film thickness that should be used to confirm the measurements reported here and elsewhere.

3.7 Acknowledgements

Support for A. R. White was provided by the Department of Energy's Innovations in Fuel Cycle Research program.

CHAPTER 4. THE CONSTANT-PRESSURE GAS-DRIVEN RADIAL DISPLACEMENT OF A FINITE NON-NEWTONIAN LIQUID DROP

4.1 Introduction

The displacement of non-Newtonian shear-thinning liquids by less viscous fluids is relevant to a number of industries including fluid-assisted injection molding (3; 4), soft lithography (5) and patterning thin polymer films (6). The displacement process can often result in viscous fingering instabilities similar to many Newtonian displacement processes which have been studied for many years (10; 13; 14; 15; 16; 18; 26). This viscous fingering instability often negatively impacts the industrial process, but in some cases such as patterning the instability can be a desired effect (6). Therefore the study of viscous fingering in shear-thinning liquids has been a popular topic dating back to work by Nittmann and Daccord in *Nature* in 1985 (19). Since then many studies on the non-Newtonian problem have been performed.

The first stability analysis of non-Newtonian displacement in a *radial* Hele-Shaw cell was done by Buka, Palffy-Muhoray and Racz in 1987 (21; 22). They studied a liquid crystal being displaced by gas at a constant pressure and used Darcy's Law to formulate a linear stability analysis. While their data seem to fit well with their analysis the use of Darcy's Law may be inappropriate because, as has been shown in chapter 2 and 3, the constant pressure problem results in an interface velocity which is not constant so the flow profile cannot be assumed developed. Nonetheless their experiments exhibit the tell-tale fractal or dendritic fingering patterns that are characteristic of the shear-thinning viscous fingering problem.

A number of other papers have been published on shear-thinning viscous fingering where the less viscous phase is injected at a constant flow rate (20; 66; 67; 68; 69). This means the mean interface velocity is known and a linear stability analysis can be performed. Often in

these studies the instability is characterized by the finger widths, fingering density, perturbation growth rate or the corresponding wavenumber of the fastest growth rate. For example in work by Daccord and Nittmann fingering densities and the fractal dimension are used to quantify the instability for the whole displacement region (20). Instability growth rates have also been used such as in work by Park and Homsy and also by Wilson where the instability amplitude grows in the flow direction exponentially with time (18; 68). There have been fewer studies using a constant pressure displacement. In a paper by Yamamoto *et al* (23) a constant pressure displacement in a linear Hele-Shaw cell was used where they characterized the instability by measuring the density of fingering and also the number of side-branches observed. While these methods for quantifying the instability work well for single fingers or generalizations of a particular fingering regime some information can be lost. In the case of comparing Newtonian viscous fingering, which exhibits smooth pedal-like fingers, to shear-thinning viscous fingering, which can exhibit more complex fractal patterns (19; 20; 21; 66), using finger widths or fingering densities may not satisfactorily compare the two regimes. Also due to the highly non-linear side-branching phenomena in shear-thinning viscous fingering, defining a growth rate in the flow direction becomes difficult.

In this chapter a new method for quantifying the viscous fingering instability that applies to both Newtonian and non-Newtonian fingering regimes will be presented based on comparing the length of the unstable interface to the circumference of the corresponding stable interface. This is analogous to the technique used by Zhao and Maher in their 1990 paper where the length of the interface in a linear Hele-Shaw cell was compared to the initial length of the stable interface (70). This new method measures a physical property that is universal to all viscous fingering problems making it applicable to any viscous fingering regime. This quantity can also be tracked with time and a rate of growth can be found even in highly non-linear regimes. Experiments will be performed using air at constant pressure to displace a finite liquid drop of light mineral oil (Newtonian) and mineral oil with either 250 or 500 ppm polyisobutylene (shear-thinning) in a radial Hele-Shaw cell. In addition to introducing the new instability quantification technique a number of other analytical tools will be used to characterize the displacement process. Similar to chapter 2 and 3 the area of the gas phase will be tracked with

time to determine a rate of expansion of the gas. The same conservation of volume technique will be used to estimate the residual film thickness, and the time it takes for the gas phase to burst through the liquid drop will also be measured.

In the following sections a description of the techniques used to measure the displaced area and the interface length will be presented and the new instability quantification method will be described. Also empirical relationships that describe the gas expansion and film formation over time will be presented. Later a detailed description of the experimental setup and procedure will be presented as well as the improved image analysis technique. The results and discussion will follow and conclusions based on the results will be made.

4.2 Analysis

The problem begins with a finite drop of light mineral oil *or* light mineral oil containing a certain concentration of polyisobutylene (PIB) squeezed between two horizontal plates. The drop is considered to be a cylinder with initial cross sectional area A_i and height equal to the gap b between the plates. The gap b is small such that, with the liquid density $\rho = 820\frac{kg}{m^3}$ and surface tension $\gamma = 0.03\frac{mN}{m}$, the Bond numbers ($Bo^* = \frac{\rho g b^2}{\gamma}$) range between $7\times10^{-4} \leq Bo^* \leq 1.68\times10^{-2}$. The superscript '*' denotes dimensionless variables. The small Bo^* allows for gravitational effects to be neglected and for the assumption that the residual film thicknesses are equal on the top and bottom plates (refer to Fig. 4.1b and 4.1c). The Reynolds numbers Re^* range between $10^{-6} < Re^* < 10^{-1}$ so inertial effects will not be greatly important. The definition of the Re^* used in the proceeding analysis will be defined in section 4.2.3.

At $\Delta t = 0$ air is injected into the center of the liquid drop through the bottom plate with a constant pressure P_g. The gauge pressure of the injected air is then $\Delta P = P_g - P_{atm}$ and $\Delta P/P_{atm} \ll 1$ so that the gas density and temperature can be assumed constant. For elapsed times $\Delta t > 0$ the gas displaces the liquid phase radially and, after some elapsed time, the interface that forms between the injected gas and the liquid becomes unstable in the form of *viscous fingering*. Eventually the injected gas escapes through the liquid phase, the interface becomes discontinuous, and the experiment ends. This elapsed time is called t_{burst}. In chapter 2 a power law relationship between t_{burst} and the gas pressure was found according to:

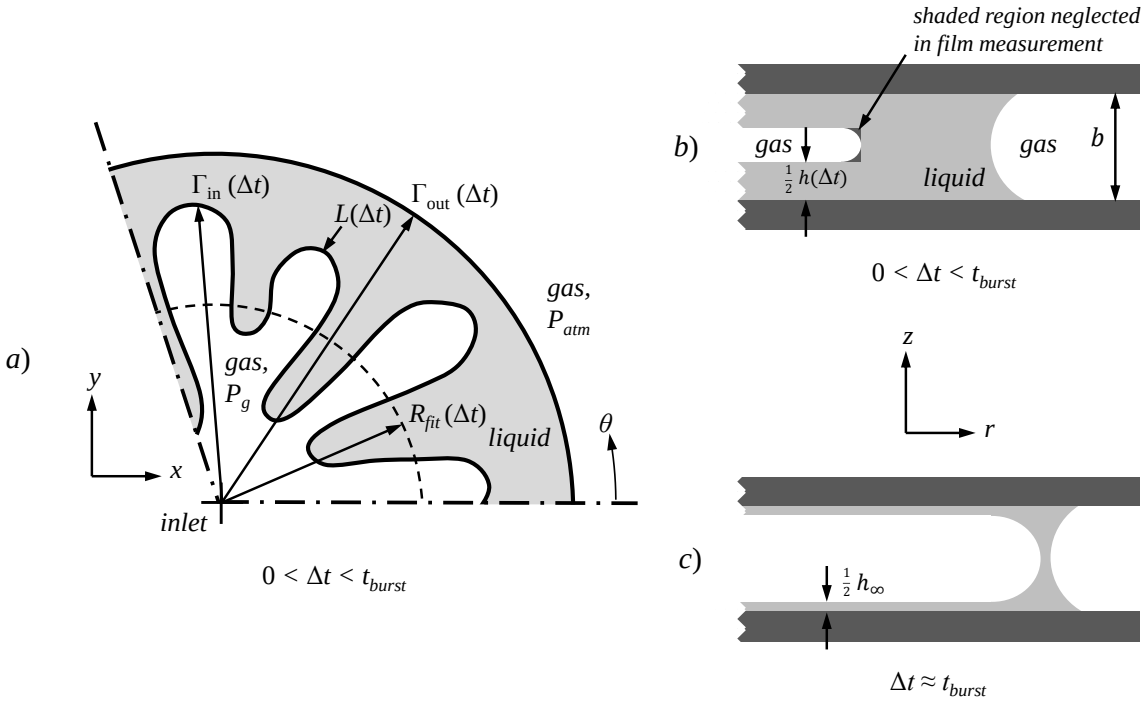

Figure 4.1 *An arbitrary sector of the gas-driven displacement in the horizontal plane is shown in (a) with the inner liquid-gas interface, $\Gamma_{in}(\Delta t)$, whose length is $L(\Delta t)$, and the outer interface, $\Gamma_{out}(\Delta t)$, at elapsed time $0 \le \Delta t \le t_{burst}$. Also pictured is the fitted radius $R_{fit}(\Delta t)$ of the corresponding stable case. The displacement in the vertical plane is shown in (b) and (c) where the gap between the plates is b. The residual film $h(\Delta t)$ is assumed equal on top and bottom so that either side is $h(\Delta t)/2$ as shown in (b). In (c) the elapsed time approaches t_{burst} and the film approaches a quasi-equilibrium value, h_∞.*

$$\frac{t_{burst}\nu_o b}{V_L} = C_t\left[\frac{\Delta p}{\mu_o}\sqrt{\frac{\rho b^3}{\gamma}}\right]^p \tag{4.1}$$

where ν_o and μ_o are the kinematic and dynamic viscosities measured at the 1 Hz shear rate (see Fig. 4.2) and V_L is the liquid volume. The constant C_t and the exponent p are to be determined experimentally. For all analyses in this chapter viscosities for the Newtonian and non-Newtonian liquids shown in Fig. 4.2 will be taken at the 1 Hz shear rate. Experimental data in this chapter will be fit to eq. 4.1 and compared to the result from chapter 2.

4.2.1 Area measurement using an integral method

Consider the liquid-gas interfaces $\Gamma_{in}(\Delta t)$ and $\Gamma_{out}(\Delta t)$ that are present as the gas phase displaces the finite liquid phase as shown schematically in Fig. 4.1a. The cross-sectional area contained by Γ_{in} , A_{gas}, as well as the area contained by Γ_{out}, A_{tot}, at any elapsed time Δt is desired. Previously to calculate A_{gas} and A_{tot} the pixels occupied by either area were counted. A more convenient method for determining the areas uses the Kelvin-Stokes theorem: $\iint_A(\nabla\times\mathbf{F})\cdot\mathbf{n}dA = \oint_C \mathbf{F}\cdot d\mathbf{s}$. Here $\mathbf{F}$ is a vector field defined on the region A enclosed by the simple closed curve C and $\mathbf{n}$ is the normal vector to the region A. In the case of region A being planar and by choosing $(\nabla\times\mathbf{F})\cdot\mathbf{n} = \frac{\partial F_y}{\partial x} - \frac{\partial F_x}{\partial y} = 1$ the double integral becomes exactly the area of the region A enclosed by C. One solution for $\mathbf{F}$ is $F_x = -\frac{1}{2}y$ and $F_y = \frac{1}{2}x$, and it follows that the area enclosed by a simple closed curve C is $A = \frac{1}{2}\oint_C(xdy - ydx)$. This equation can be used to find the area A_{gas} enclosed by Γ_{in} which is a simple closed curve. With the discretized inner interface $\Gamma_{in}(n)$ composed of N points where $\Gamma_{in}(1) = \Gamma_{in}(N)$, we can chose $x(n) = \Gamma^n_{in,x}$, $y(n) = \Gamma^n_{in,y}$, $dx(n) = \Gamma^{n+1}_{in,x} - \Gamma^n_{in,x}$ and $dy(n) = \Gamma^{n+1}_{in,y} - \Gamma^n_{in,y}$, resulting in:

$$A_{gas}(\Delta t) = \frac{1}{2}\sum_{n=1}^{N-1}(\Gamma^n_{in,x}\Gamma^{n+1}_{in,y} - \Gamma^n_{in,y}\Gamma^{n+1}_{in,x}) \tag{4.2}$$

which returns a positive result when traveling counterclockwise about the interface. In an identical way the area enclosed by Γ_{out} is found using

$$A_{tot}(\Delta t) = \frac{1}{2}\sum_{n=1}^{N-1}(\Gamma^n_{out,x}\Gamma^{n+1}_{out,y} - \Gamma^n_{out,y}\Gamma^{n+1}_{out,x}). \tag{4.3}$$

With the exception of very early elapsed times, Γ_{in} and Γ_{out} typically contain $O(10^2)$ to $O(10^3)$ points.

4.2.2 Viscous fingering quantification

Consider again the interface $\Gamma_{in}(\Delta t)$ and now the area occupied by the gas phase $A_{gas}(\Delta t)$. Stable radial displacement of the liquid by the gas is defined as displacement with no fingering i.e. $\Gamma_{in}(\Delta t)$ is a circle . Therefore at a given elapsed time with displaced area A_{gas} the corresponding stable case would be a circle with radius $R_{fit}(\Delta t) = \sqrt{\frac{A_{gas}(\Delta t)}{\pi}}$. The length of the observed discretized inner interface with N points at a particular elapsed time can be approximated by summing the distances between each of the points, or

$$L = \sum_{n=1}^{N-1} [(\Gamma_{in,x}^{n+1} - \Gamma_{in,x}^{n})^2 + (\Gamma_{in,y}^{n+1} - \Gamma_{in,y}^{n})^2]^{\frac{1}{2}}. \tag{4.4}$$

Then a direct comparison can be made between the length of the inner interface L and the circumference of the corresponding stable case:

$$\xi(\Delta t) = 1 - \frac{L(\Delta t)}{2\pi R_{fit}(\Delta t)} \tag{4.5}$$

where ξ will be called the *fingering magnitude*. This new quantity provides a robust measurement of the degree to which viscous fingering is occurring and provides a picture of how the instability grows with time in radial geometry. While it does not imply anything about the instability's geometry, it allows for a direct comparison between very different fingering regimes such as smooth Newtonian *pedal* fingers to complex non-Newtonian *dendritic* instabilities (see Fig. 4.7).

For early elapsed times Γ_{in} is roughly circular and thus $\xi \simeq 0$ up to the time when the instability first develops, t_s. The threshold for when the displacement is in the viscous fingering regime is chosen as $\xi \approx 0.09$ which was determined by examining experimental images qualitatively, and from $t_s \leq \Delta t \leq t_{burst}$ ξ increases roughly linearly on this domain. Therefore the fingering magnitude can described by:

$$\xi(\Delta t) = \begin{cases} 0 & : 0 \leq \Delta t < t_s \\ \omega_\xi \left(t_s - \Delta t\right) & : t_s \leq \Delta t \leq t_{burst} \end{cases} \tag{4.6}$$

where the slope ω_ξ is the *instability growth rate*. The experimental data will be fit to eq. 4.6 and the instability growth rates of both Newtonian and shear-thinning displacements will be compared.

4.2.3 Gas expansion rate and dimensionless numbers

An empirical correlation for the expansion rates of the gas area was previously postulated in chapter 2 and again in chapter 3

$$A_{gas}(\Delta t) = C_{gas}(e^{\omega_{gas}\Delta t} - 1) \tag{4.7}$$

where C_{gas} is a constant and ω_{gas} is the gas area expansion rate. This exponential model has been used successfully and we will continue to use it in this chapter. Two important dimensionless parameters for characterizing the system are the Reynolds number, Re^*, and the capillary number, Ca^*. Both of these numbers traditionally include a characteristic velocity. Whereas a constant flow rate system can use that flow rate to determine a characteristic velocity, determining a characteristic velocity in the constant pressure system is not as straight forward. Furthermore with the introduction of the viscous fingering instability the velocity becomes not only a function of time but also r and θ. Therefore a different approach to determining a characteristic velocity and thus a Re^* and Ca^* that justly characterizes the system on the whole will be used.

Using eq. 4.7 implies that the average gas radius as a function of time is of the form $\bar{r} \propto \sqrt{e^{\omega_{gas}\Delta t} - 1}$. Using the first two terms of the Taylor series expansion of $e^{\omega_{gas}\Delta t}$ gives $\bar{r} \propto \sqrt{\omega_{gas}\Delta t + O(\omega_{gas}\Delta t)^2}$. By ignoring the higher-order terms the average velocity is proportional to the square root of the expansion rate or $\bar{v} \propto \sqrt{\omega_{gas}}$. Let us replace the characteristic velocity in Re^* and Ca^* then with $\sqrt{\omega_{gas}}$:

$$Re^* = \frac{\rho\sqrt{\omega_{gas}}b}{\mu_o} \cdot N_{Re} \tag{4.8}$$

$$Ca^* = \frac{\mu_o\sqrt{\omega_{gas}}}{\gamma} \cdot N_{Ca}. \tag{4.9}$$

The undefined terms N_{Re} and N_{Ca} are necessary to make the groups dimensionless. In an attempt to determine the simplest forms for N_{Re} and N_{Ca} we will choose $N_{Re} = N_{Ca} = \sqrt{\nu_o}$. This results in

$$Re^* = b\sqrt{\frac{\rho\omega_{gas}}{\mu_o}} \tag{4.10}$$

$$Ca^* = \frac{1}{\gamma}\sqrt{\frac{\mu_o^3\omega_{gas}}{\rho}} \tag{4.11}$$

where the characteristic velocity is now essentially $v_{char} = \sqrt{\nu_o\omega_{gas}}$. Previous work shown in chapter 2 and 3 has also suggested a power law relationship between ω_{gas} and $\frac{\Delta p}{\mu_o}$. Under the assumption that $\omega_{gas} \sim \frac{\Delta p}{\mu_o}$ a second set of Re^* and Ca^* will be defined by replacing $\sqrt{\omega_{gas}}$ with $\sqrt{\frac{\Delta p}{\mu_o}}$:

$$Re_p^* = \frac{b}{\mu_o}\sqrt{\rho\Delta p} \tag{4.12}$$

$$Ca_p^* = \frac{\mu_o}{\gamma}\sqrt{\frac{\Delta p}{\rho}}. \tag{4.13}$$

To test the relationship between ω_{gas} and $\frac{\Delta p}{\mu_o}$ the two Reynolds numbers, Re^* and Re_p^*, will be plotted against each other:

$$\frac{\rho\omega_{gas}b^2}{\mu_o} = C_\omega\left[Bo^* \cdot \frac{\rho b^2}{\mu_o}\left(\frac{\Delta P}{\mu_o}\right)\right]^m \tag{4.14}$$

where an exponent of $m \approx 1$ would indicate that $\omega_{gas} \sim \frac{\Delta p}{\mu_o}$.

4.2.4 Residual film estimation

The transient residual film $h(\Delta t)$ is determined using a global mass conservation approach identical to that used in chapters 2 and 3, leading to the expression

$$\frac{h(\Delta t)}{b} = 1 - \frac{A_{tot}(\Delta t) - A_i}{A_{gas}(\Delta t)}, \tag{4.15}$$

where A_i is the initial area of the drop. This transient value is the sum of the film on the top and bottom plate. The quasi-equilibrium value, h_∞/b, is defined as the film thickness at

$\Delta t = t_{burst}$.

The above equation neglects the curvature at the inner interface. One can show that the effect of disregarding the curvature of the interface in film estimation is negligible. Referring to Fig. 4.1b, the region neglected in the above equation is the shaded area around the inner liquid-gas interface. The cross sectional area in this region is $A_{neglect} = (b-h)^2\left(\frac{1}{2} - \frac{\pi}{8}\right)$ and integrating about the interface gives $V_{neglect} = \int_{\Gamma_{in}} A_{neglect} d\ell$ or

$$V_{neglect} = (b-h)^2\left(\frac{1}{2} - \frac{\pi}{8}\right)\sum_{i=1}^{N-1}\left[(\Gamma_{in,x}^{i+1} - \Gamma_{in,x}^{i})^2 + (\Gamma_{in,y}^{i+1} - \Gamma_{in,y}^{i})^2\right] \tag{4.16}$$

It will be shown later in this chapter that values for h typically range between $0.1 \leq \frac{h}{b} \leq 0.5$. Then the leading terms in eq. 4.16 before the summation notation will be $O(10^{-3})$ to $O(10^{-5})$ mm^2. The longest interface occurs in the 500 ppm PIB experiment at 6.9 kPa in a 50 μm gap where the interface is nearly 90 cm long. In this maximum case the value of $V_{neglect}$ would be about $O(0.1)$ μL which is much less than the 50 μL volume.

Previously an exponential rate of decay was suggested for the formation of thin films on the top and bottom walls of the Hele-Shaw cell. This provided some further insight into the relationship between the film formation rate and the injection pressure. Further analysis, partially based on improved algorithms for measuring the expansion area described in section 4.2.1, have led to attempts of additional curve fits. Here a power law relationship is proposed for the film formation of the form $h(t) = C_{film}(\Delta t)^{n_{film}}$ where n_{film} is the formation power law exponent and C_{film} is the power law coefficient. Best fits of the data using this relation results in a nearly constant n_{film} over the range of experiments with a value of approximately $-\frac{1}{2}$. This suggests a diffusion like process that leads to film formation. The constant C_{film} however does vary with pressure and polymer concentration. Our proposed model for the transient film thickness is then:

$$h(\Delta t) = C_{film}(\Delta t)^{-\frac{1}{2}} \tag{4.17}$$

where C_{film} is to be determined experimentally. As for a relationship between the gas pressure

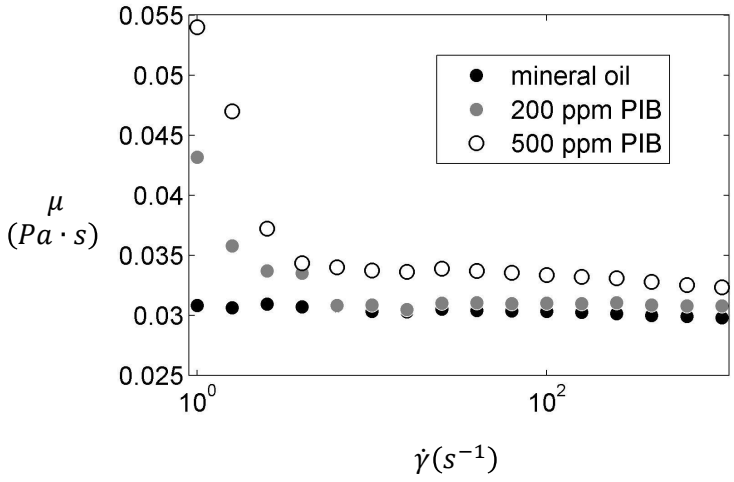

Figure 4.2 *Viscosity versus strain rate data for 0, 200 and 500 ppm polyisobutylene (M.W. 4,700,000) in light mineral oil is shown. The rheology data was measured using a parallel plate-plate rheometer.*

and the quasi-equilibrium film thickness the value Ca_p^* from eq. 4.11 will be used.

4.3 Materials and procedure

4.3.1 Setup and experimental procedure

Two square acrylic plates with a thickness of 11 mm and width of 15 cm were used to create the Hele-Shaw cell. Plastic shims (AccuTrex) with thicknesses of 50, 100 and 250 μm were placed between the two plates to achieve the desired gap spacing. In one plate a 10-32NC thread was tapped into the center in order to insert a plastic barbed fitting (Cole Parmer) with an inner diameter of 2.4 mm. Through this inlet air was injected into the cell at a constant pressure $1.4 \leq \Delta P \leq 6.9$ kPa which was controlled by a pressure regulator (Marsh Bellofram). Up stream from the regulator was a solenoid valve (Marsh Bellofram) controlled by a function generator (Agilent) that initiated the flow when desired. Air was stored upstream from the valve at a pressure much greater than the operating pressures.

A liquid drop with a volume of 100, 200 or 500 μL for the 50, 100 or 250 μm gap spacings, respectively, was used to keep the initial drop area roughly constant. With the cell disassembled

the drop was pipetted (Biohit) onto the plate without the inlet. The plate with the inlet was then carefully placed on top with the drop centered about the inlet. Large binder clips held the cell together. A CCD camera (PixeLINK) was used to capture video with a resolution of 640 x 480 pixels and frame rates up to 100 fps. The camera viewed the experiments at an angle of 20° from normal to the cell and a 300 W lamp was used to illuminate the drop. Though the drop and surrounding air are clear the refraction indices are different and the combination of lighting and viewing angle produced a high contrast between the liquid and gas (see Fig. 4.3a). The slight distortion in the y-direction of each experimental frame caused by the camera angle was easily corrected during image analysis by scaling the y-axis by $(cos20°)^{-1}$. Experimental videos were captured from the initial injection of the gas up to the bursting time t_{burst}.

The experimental liquids used were light mineral oil (Fisher Scientific) with 0, 250 and 500 ppm polyisobutylene (Acros) with an approximate M.W. of 4,700,000. The oil-polymer solutions were mixed at 80°C using a magnetic stirring hot plate. All experimental fluids were at room temperature during experiments. Rheology data showing the viscosity versus strain rate are shown in Fig. 4.2. The rheology data was acquired using a parallel plate-plate rheometer. Experiments in a 250 μm gap at 6.9 kPa reached t_{burst} too quickly for an adequate number of experimental frames at 100 fps, so at 250 μm only pressures up to 5.5 kPa were used. In total 42 experiments were performed.

4.3.2 Image analysis

The experimental videos captured with the CCD camera were analyzed in MATLAB frame by frame. Each frame is a bitmap image with pixel values ranging from 0 to 255 where 0 corresponds to black and 255 corresponds to white. The combination of camera angle and lighting allowed the area occupied by the drop to appear significantly darker than the surrounding gas-filled areas. A threshold could then be chosen where pixels below it had their values floored to 0 to represent pixels occupied by liquid. Pixels above the threshold were given a value of 255 to represent pixels occupied by air. A simple 2-D median filter was used to smooth the data in some cases (MATLAB function: "medfilt2"). An example of a raw video frame and the frame after the application of a threshold is shown in Fig. 4.3a and Fig. 4.3b, respectively.

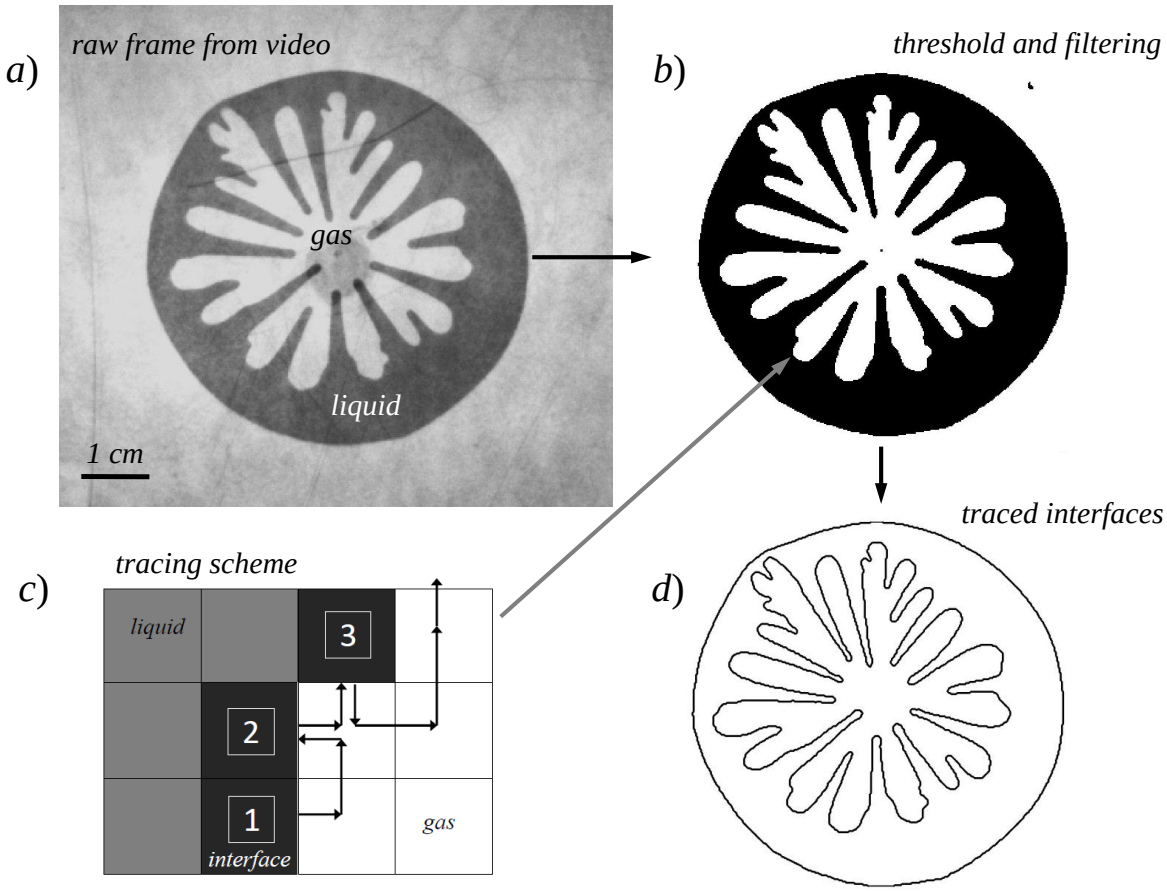

Figure 4.3 *A pixel threshold and filtering process is applied to a raw frame from an experimental video in (a) resulting in the black and white image in (b). A schematic of the interface tracing scheme is shown in (c) which then results in traces of the inner and outer interfaces in (d). The inner interface in (d) in this example consists of 2364 points and the outer interface consists of 844 points.*

Next it was necessary to trace the inner and outer liquid-gas interfaces. In Fig. 4.3c a zoomed-in view of an arbitrary location on the interface is shown where each square is a pixel. The white squares represent the gas area, the light gray squares represent the liquid area, and the dark gray squares represent the interface and are the pixels we wish to trace. Beginning with a known pixel on the interface the eight adjacent pixels are investigated one at a time in a counterclockwise manner until a pixel with value 0 is found. For example in FIG. 4.3c the initial known pixel is marked with a '1'. Then the pixel to its right is called. Because that pixel is white (has a value of 255) it continues counterclockwise as indicated by the arrows. Finally a pixel with a value = 0, marked by a '2' in Fig. 4.3c, is reached. Then the process continues by searching the pixels adjacent to pixel '2'. It is crucial that the first pixel called in the sequence is to the side from which the current pixel was reached. As shown in Fig. 4.3c, when discovering pixel '2' the movement was from right to left. Therefore the first step in discovering the next pixel is to move from left to right starting from pixel '2'. This algorithm is used to trace both the inner interface, Γ_{in}, and outer interface, Γ_{out}, as shown in Fig. 4.3d. With the inner and outer interfaces traced the areas occupied within each interface as well as the length of the interface can be calculated and then used in the analytical tools described earlier in this chapter.

4.4 Results

Figures 4.4, 4.5 and 4.6 show the traces of actual liquid-gas interfaces for select experiments in a 50, 100 and 250 μm gap, respectively. Each experiment shown is at $\Delta t = t_{burst}$. A dotted circle is plotted on top of each inner interface where the circle shares its center with the inner interface's centroid and the circle's area is equal to $A_{gas}(t_{burst})$. This fitted circle represents the corresponding stable case described in section 4.2.2. In each plot the pressure is listed on the left which increases from top to bottom and the PIB concentration is listed across the top which increases from left to right. The inner interface Γ_{in} and outer interface Γ_{out} are labeled in each figure in the top right. A scale bar is shown at the bottom in cm. In Fig. 4.4, particularly at the lowest pressure, there exists a small portion of liquid that remains attached to the gas inlet. With the gap being so small in these experiments the liquid phase likely has

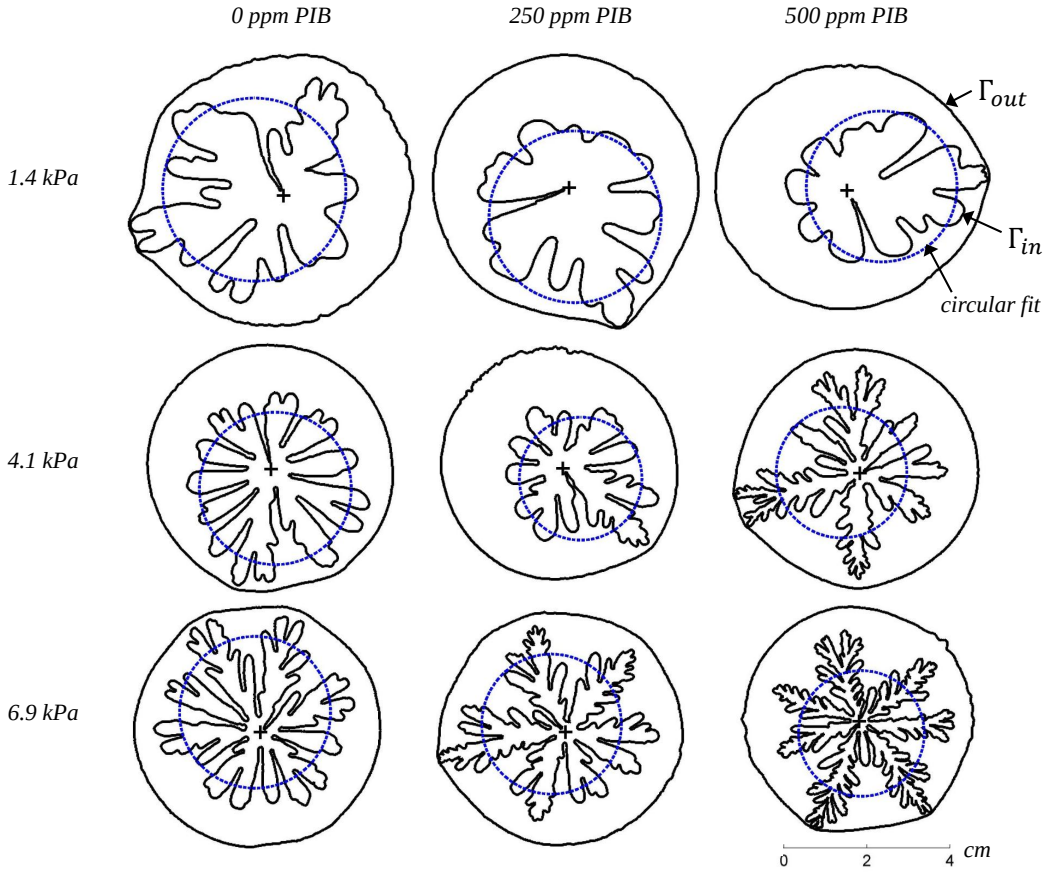

Figure 4.4 *The inner interface, Γ_{in}, and the outer interface, Γ_{out}, of experiments in a 50 μm gap are traced in black at elapsed time t_{burst}. Pressure increases from top to bottom and PIB concentration increases from left to right. The gas inlet is marked with a "+" and the inner interface of the corresponding stable case with radius R_{fit} is represented by the circular dotted line.*

difficulty de-wetting the sharp edge of the gas inlet. While this certainly has an impact on the qualitative view of the displacement, the quantitative measures of these experiments still fit well with the rest of the data as will be shown in the proceeding results.

In Fig. 4.7 the inner interfaces for mineral oil (Fig. 4.7a) and mineral oil with 500 ppm PIB (Fig. 4.7b) in a 100 μm gap at 4.1 kPa are traced at time steps of 100 ms, providing a clear look at the evolution of Newtonian and shear-thinning viscous fingering. The concepts of tip-splitting, primarily a Newtonian feature, and side-branching, primarily a shear-thinning feature, are clearly defined in this figure.

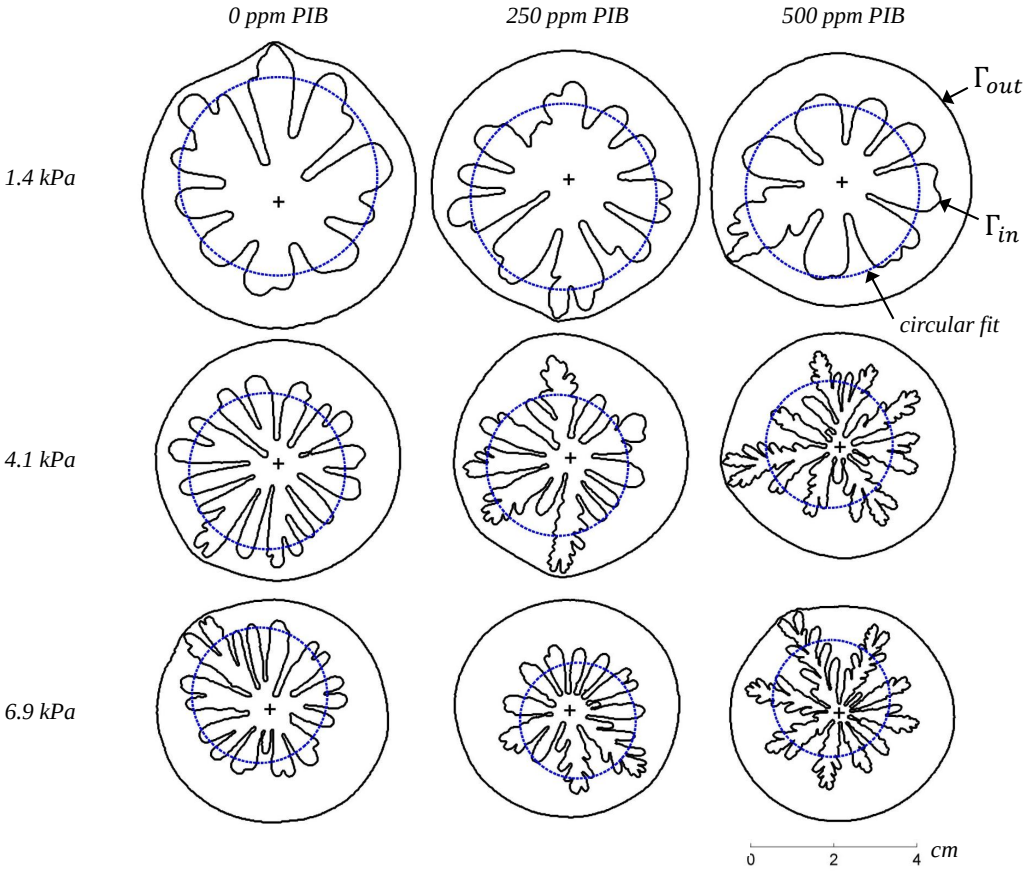

Figure 4.5 *The inner interface, Γ_{in}, and the outer interface, Γ_{out}, of experiments in a 100 μm gap are traced in black at elapsed time t_{burst}. Pressure increases from top to bottom and PIB concentration increases from left to right. The gas inlet is marked with a "+" and the inner interface of the corresponding stable case with radius R_{fit} is represented by the circular dotted line.*

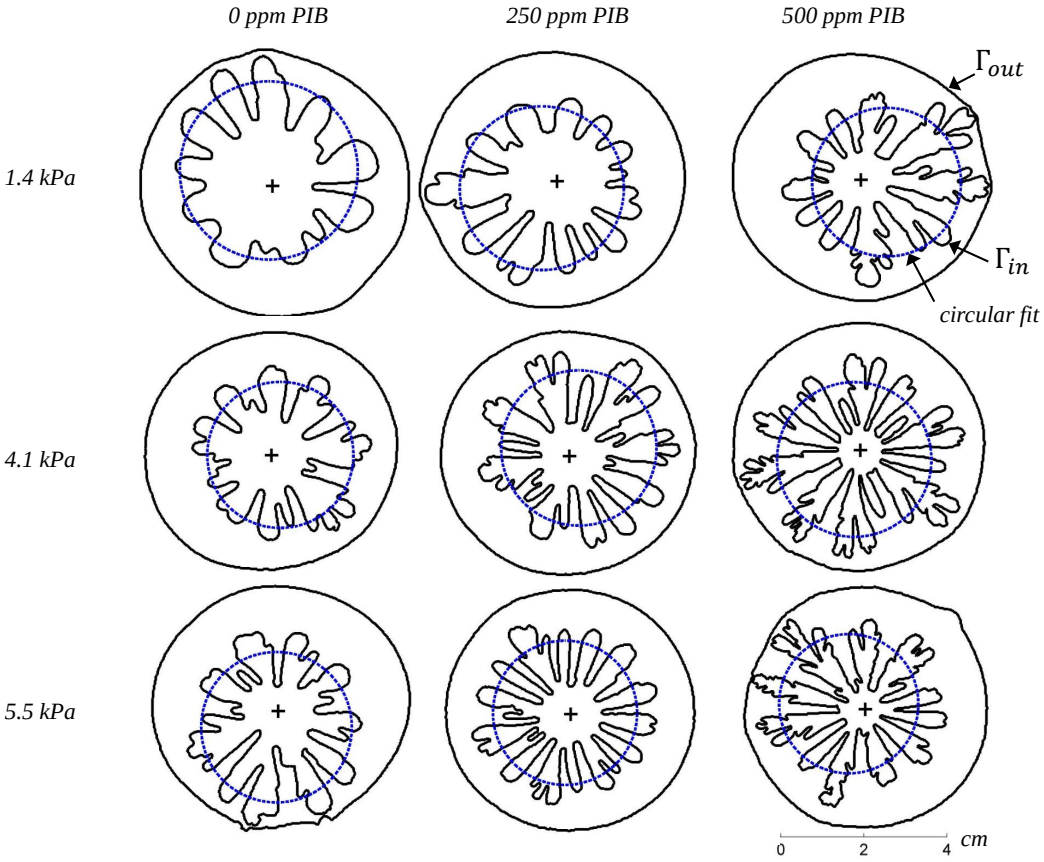

Figure 4.6 *The inner interface, Γ_{in}, and the outer interface, Γ_{out}, of experiments in a 250 μm gap are traced in black at elapsed time t_{burst}. Pressure increases from top to bottom and PIB concentration increases from left to right. The gas inlet is marked with a "+" and the inner interface of the corresponding stable case with radius R_{fit} is represented by the circular dotted line.*

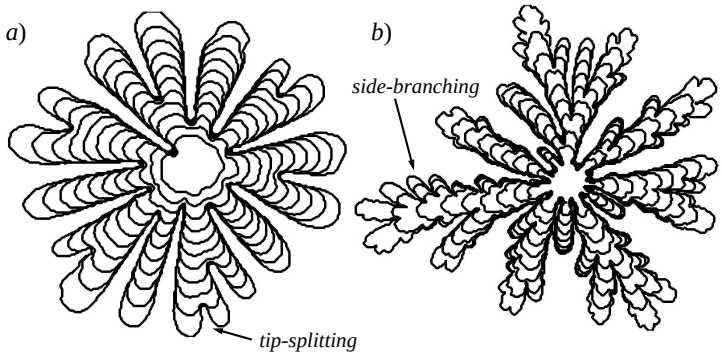

Figure 4.7 *The inner interfaces of a) mineral oil and b) mineral oil with 500 ppm PIB being displaced in a 100 μm gap at 4.1 kPa are shown at timesteps of 100 ms up until $\Delta t = t_{burst}$ to portray the concepts of tip-splitting and side-branching.*

The time it takes for the inner gas phase to burst through the liquid drop is plotted in log-log form in Fig. 4.8. The burst time is normalized using a combination of the viscous time scale and liquid volume, $\frac{\nu_o b}{V_L}$. This value is then plotted against $\frac{\Delta p}{\mu_o}\sqrt{\frac{b^3\rho}{\gamma}}$ similar to the result in chapter 2. The data span almost three decades in the y-direction and about two in the x-direction, and collapse onto roughly one curve whose slope is -1.21 or about $-\frac{5}{4}$. In this plot the experiments with no PIB are black, experiments with 250 ppm PIB are dark gray, and experiments with 500 ppm PIB are light gray. In the plot the circles (○, ●, ●), squares (□, ■, ■) and diamonds (◊, ♦, ♦) correspond to experiments with $Bo^* = 7 \times 10^{-4}$, 2.7×10^{-3} and 1.68×10^{-2}, respectively. The black markers (●, ■, ♦), gray markers (●, ■, ♦) and open markers (○, □, ◊) correspond to PIB concentrations of 0, 250 and 500 ppm, respectively. The data labeling convention used in Fig. 4.8 will be consistent throughout this chapter save for Fig. 4.9, 4.11 and 4.13.

The liquid displacement is further characterized by thr semi-log plot of the area occupied by the gas phase versus elapsed time in Fig. 4.9a-4.9c. The liquid drops have 0 ppm, 250 ppm and 500 ppm PIB in Fig. 4.9a, 4.9b and 4.9c, respectively. The area is nondimensionalized by

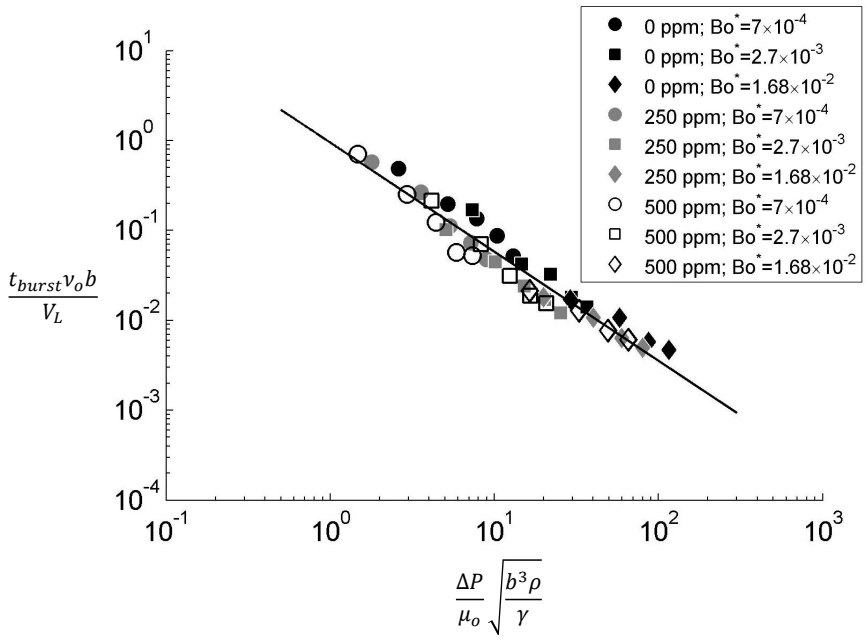

Figure 4.8 *A log-log plot of the normalized burst time is plotted against* $\frac{\Delta P}{\mu_o}\sqrt{\frac{b^3\rho}{\gamma}}$. *The data collapse onto a single curve with a slope of about* $p = -\frac{5}{4}$.

isolating the exponential term in eq. 4.7 resulting in $\frac{A_{gas}}{C_{gas}} + 1$, and the x-axis is dimensional elapsed time in seconds. For clarity only experiments using a 100 μm gap are shown although all experiments have qualitatively similar results. A best fit line using eq. 4.7 is shown as a solid line in the plot. In the plot the circles (●), down-facing triangles (▼), squares (■), up-facing triangles (▲), and diamonds (⧫) correspond to gas pressures of 1.4, 2.8, 4.1, 5.5, and 6.9 kPa, respectively. The marker labels in this figure are consistent with those in Fig. 4.11 and 4.13. In Fig. 4.9d A_{gas}, in m^2, for the displacement of mineral oil with no PIB at 4.1 kPa in a 100 μm gap is plotted versus elapsed time in seconds using both the integral method described in section 4.2.1 and the pixel counting method used in chapters 2 and 3.

Fitting the experimental A_{gas} data to eq. 4.7 and extracting the exponential growth rate provides the gas expansion rate ω_{gas} which is plotted in Fig. 4.10. The y-axis is scaled with $(Re^*)^2$ and the x-axis is scaled with $Bo^* \cdot (Re_p^*)^2$ like in eq. 4.14. The data span nearly two decades in the x- and y-directions and collapse well according to PIB concentration. A best fit line is plotted for each PIB concentration in Fig. 4.10 where each slope is the exponent m

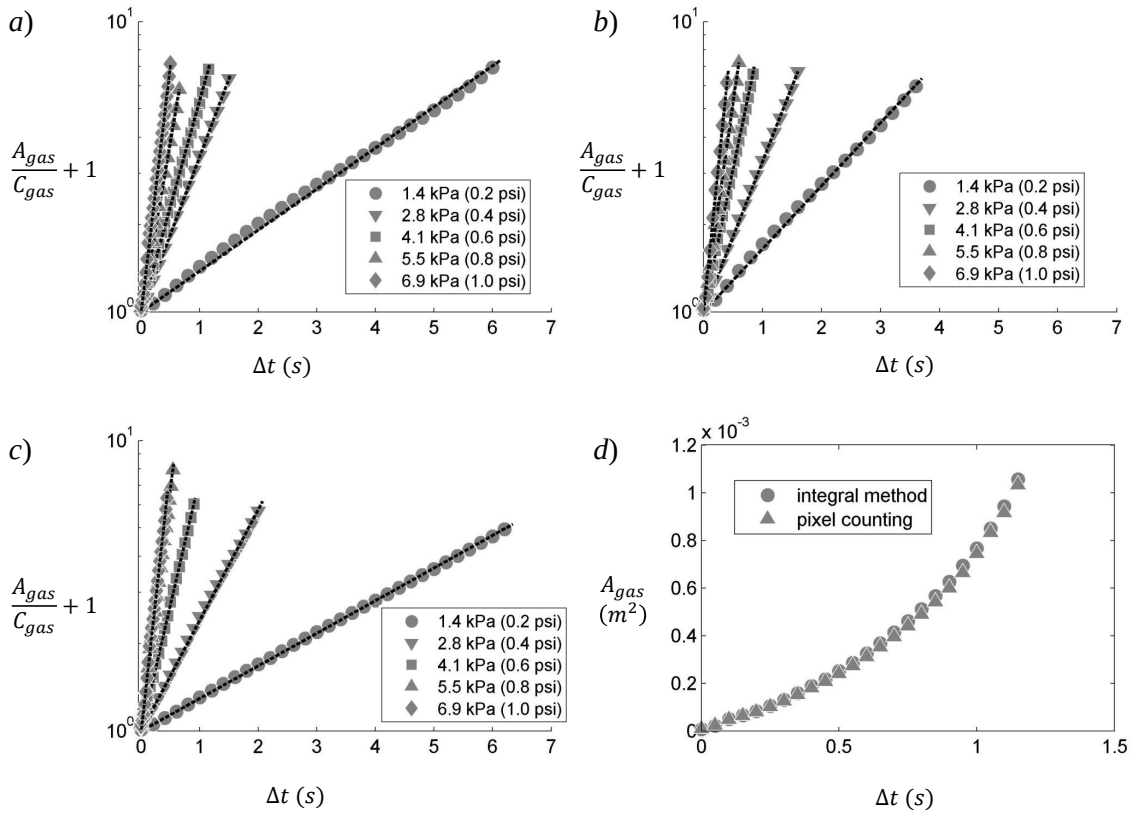

Figure 4.9 *A semilog plot of* $\frac{A_{gas}}{C_{gas}} + 1$ *versus elapsed time is shown for PIB concentrations of (a) 0 ppm, (b) 250 ppm and (c) 500 ppm each at the 100 μm gap. The curves are fit using eq. 4, highlighting the exponential growth observed for all experiments. In (d) gas areas determined using the pixel counting method from chapters 2 and 3 and the integral method described above are shown for 0 ppm PIB in a 100 μm gap displaced at 4.1 kPa.*

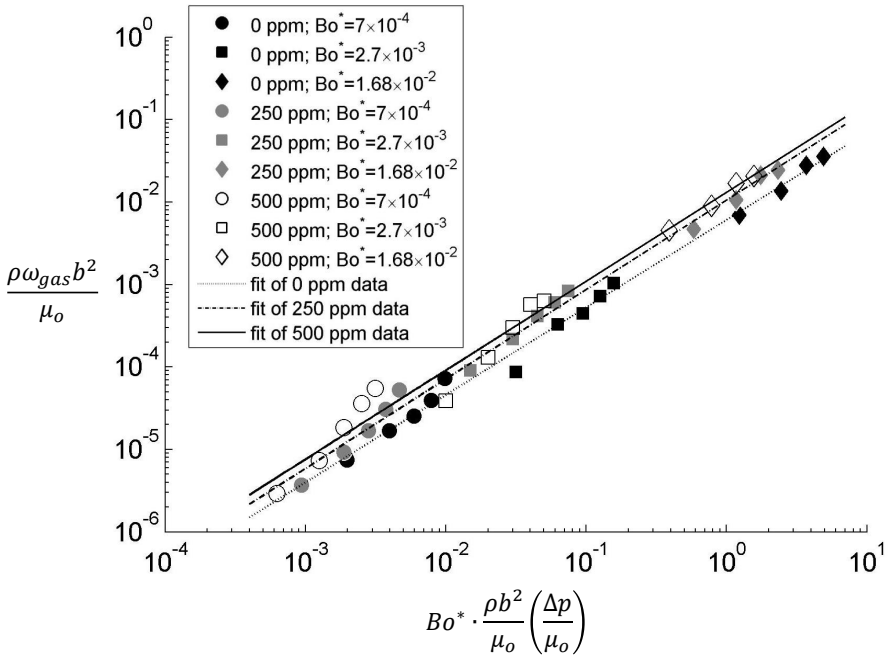

Figure 4.10 *A plot of the Reynolds number incorporating ω_{gas} is shown. The data from each concentration of PIB is fitted to a line whose slope is roughly 1.*

from eq. 4.14 and m is 1.06, 1.08 and 1.08 for the 0, 250 and 500 ppm PIB data, respectively. For the lowest Bond number the 250 and 500 ppm PIB experiments deviate slightly from the fit at higher pressures.

The transient residual liquid film normalized by the gap height is plotted against elapsed time normalized by the burst time in Fig. 4.11 for mineral oil experiments with no PIB in a 100 μm gap. Best fits using eq. 4.17 are shown as solid lines which agree fairly well with the data, particularly at later times. Some data points at the earliest elapsed times are greater than 1 likely due to errors caused by the very small gas areas at these times. The constant C_{film} from eq. 4.17 resulting in the best fit of the data is plotted versus Ca_p^* in the inset of Fig. 4.11. The constant C_{film} has units of $\mu m \cdot s^{1/2}$ and is made dimensionless here by $\frac{\sqrt{\omega_{gas}}}{b}$. Values for C_{film} vary between $20 \leq C_{film} \leq 40$ $\mu m \cdot s^{\frac{1}{2}}$.

The film at $\frac{\Delta t}{t_{burst}} = 1$ in Fig. 4.11 is taken as the quasi-equilibrium film thickness h_∞. While this is not a true equilibrium film Fig. 4.11 shows that the film is relatively stable, hence the "quasi" qualifier. A plot of $\frac{h_\infty}{b}$ is shown versus a modified capillary number Ca_p^* in Fig. 4.12.

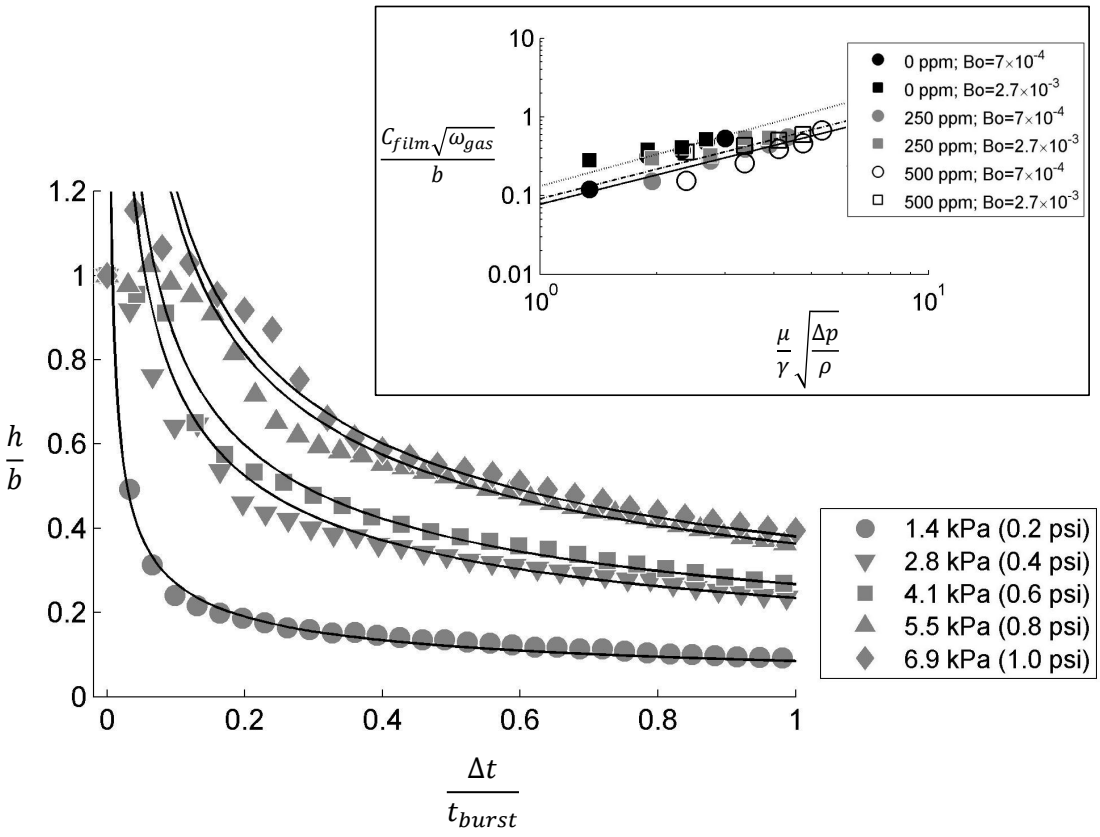

Figure 4.11 *The normalized transient residual film thickness is plotted against* $\Delta t/t_{burst}$ *for experiments with no PIB and a gap of 100* μm*. The plots are fitted using eq. 4.17 and the constant* C_{film} *for every experiment is plotted against* Ca_p^* *in the inset. The film at* $\Delta t/t_{burst} = 1$ *is the quasi-equilibrium film thickness* h_∞*.*

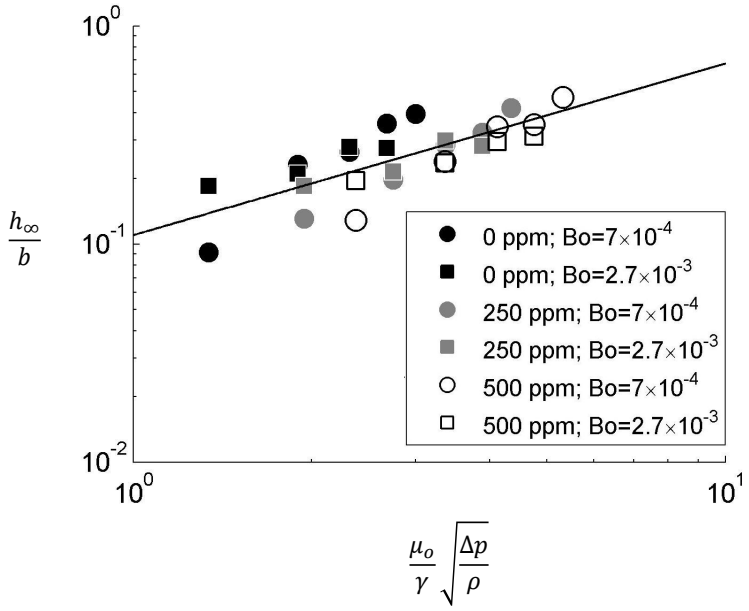

Figure 4.12 *The quasi-equilibrium film thickness estimated at t_{burst} is plotted in a log-log plot against Ca_p^*. Data for 50 μm gap experiments are omitted. The h_∞ for 100 and 250 μm gap experiments are fitted with a single curve whose slope is $\frac{4}{5}$.*

Data from 50 μm gap experiments are omitted here because those films are not sufficiently stable at t_{burst}. The data in the log-log plot is fit with a line whose slope is 0.79 or roughly $\frac{4}{5}$.

In Fig. 4.13 the fingering magnitude ξ is plotted versus elapsed time for each experiment. In each experiment there is an initial period where $\xi \approx 0$ i.e. the interface is essentially a circle. The nine plots are organized by Bo^* and PIB concentration where Bo^* decreases from top to bottom and PIB concentration increases from left to right. For one experiment with $Bo^* = 1.68 \times 10^{-2}$ and 250 ppm PIB the interfaces at $\Delta t = t_s$ and $\Delta t = t_{burst}$ are shown where the arrows indicate to which data point they correspond. This clarifies the difference between $\xi \approx 0$ and $\xi > 0$.

The threshold value for ξ when fingering is apparent is $\xi \approx 0.09$. The time when $\xi \approx 0.09$ is t_s and at this time the maximum stable gas area A_s occurs. Some values for t_s for 0 and 250 ppm experiments are shown along with t_{burst} in Fig. 4.14 where the left-facing triangles (◂), right-facing triangles (▸) and up-facing triangles (▲) correspond to Bond numbers of 7×10^{-4}, 2.7×10^{-3} and 1.68×10^{-2}, respectively. The x- and y-axis scaling is identical to that used in

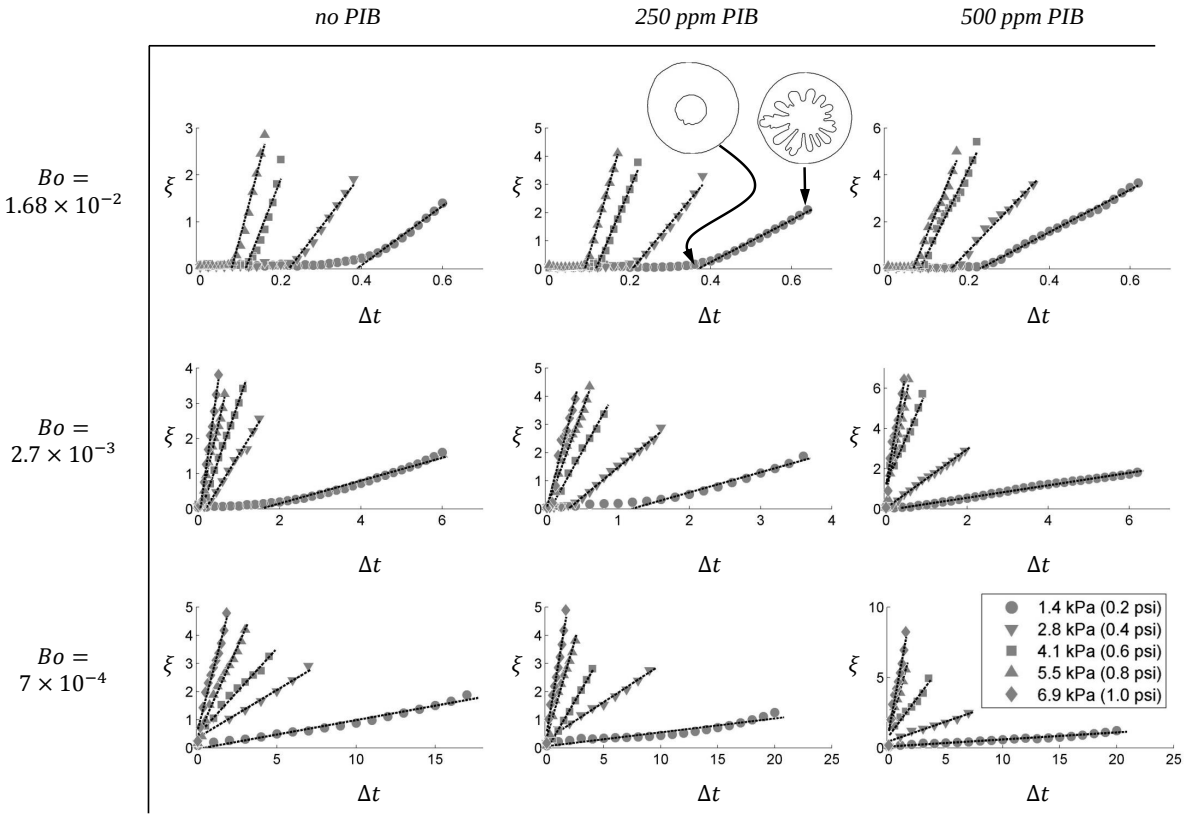

Figure 4.13 *The fingering magnitude, ξ, is plotted versus elapsed time. Data from $t_s \leq \Delta t \leq t_{burst}$ are fitted with a linear curve whose slope is the instability growth rate, ω_ξ. For the 250 ppm PIB experiment at 1.4 kPa and $Bo^* = 1.68 \times 10^{-2}$ the interface of the maximum stable area and the interface at t_{burst} is shown where the arrows indicate the data point to which they correspond.*

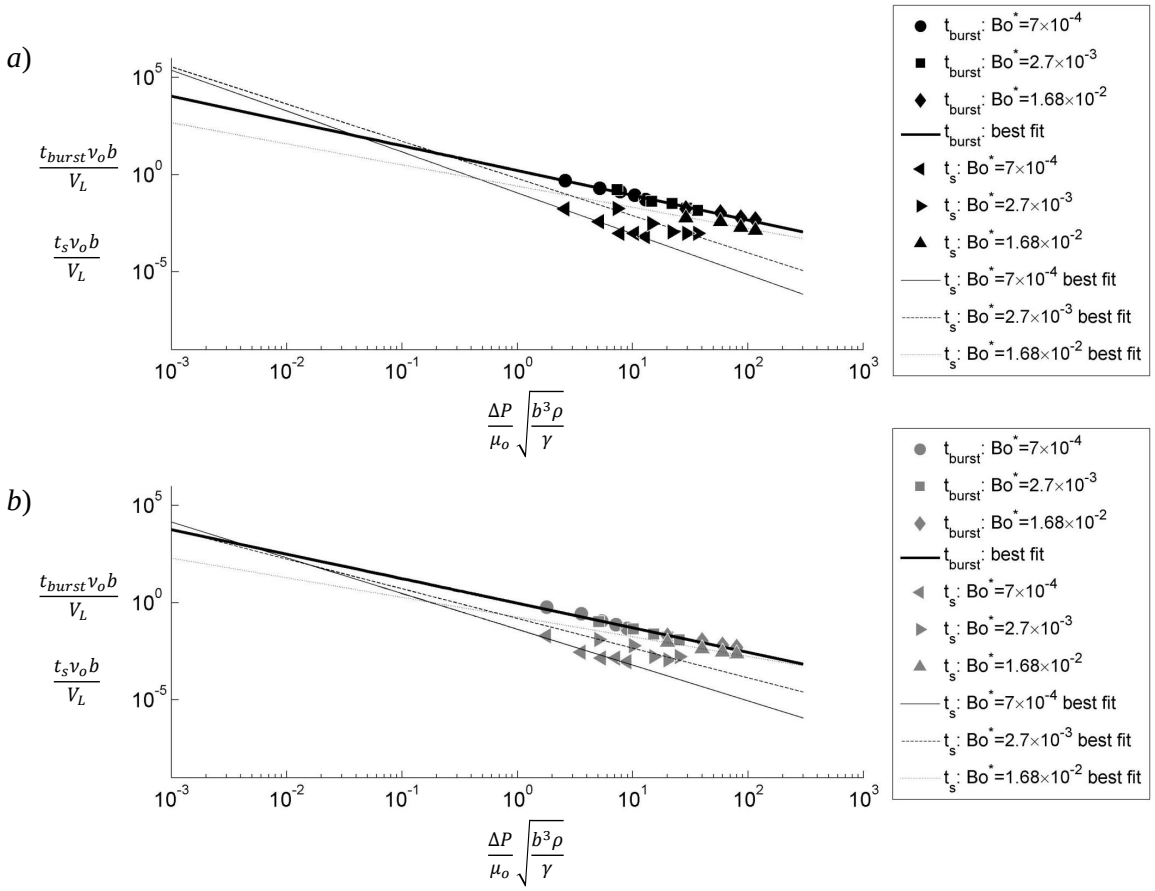

Figure 4.14 *The time it takes for the instability to develop, t_s, is plotted along with the bursting time, t_{burst}, for (a) 0 and (b) 250 ppm experiments using the same scaling from Fig. 4.8. The t_{burst} data is fit with a single curve and the t_s data is fit according to Bo^*. The x-axis is extended to show when the t_s fits intersect with the t_{burst} fit.*

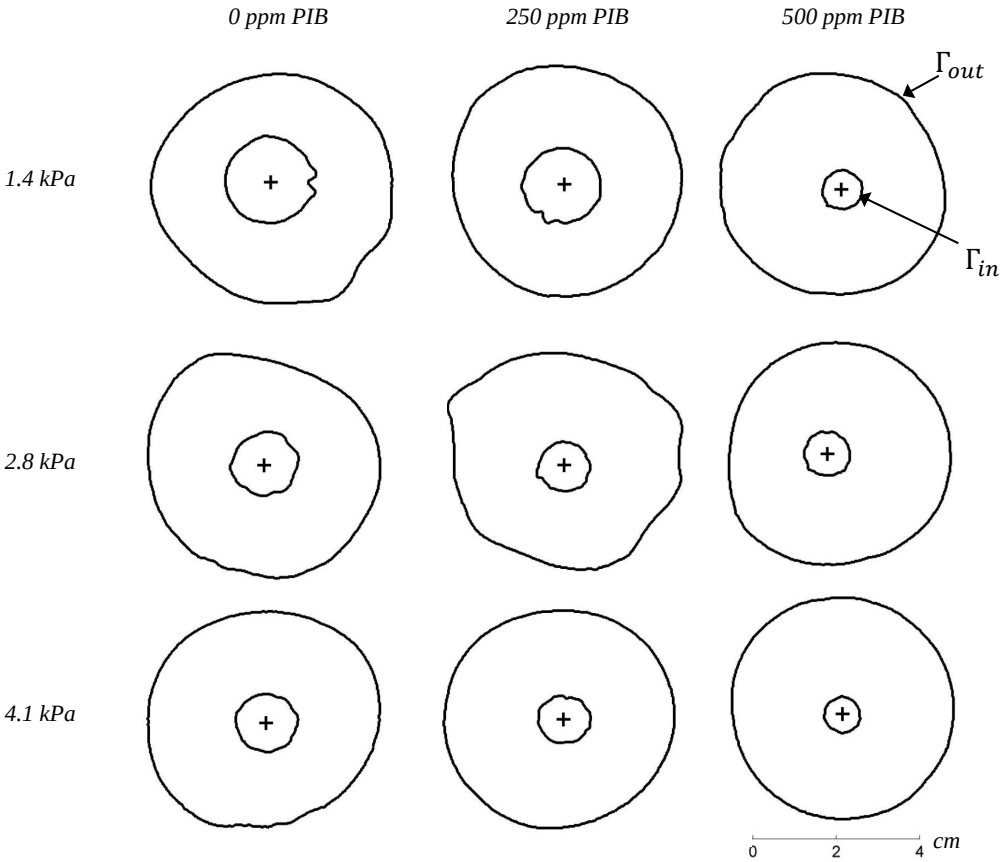

Figure 4.15 *Images of the inner and outer interfaces for experiments in a 250 μm gap are shown at time t_s when the maximum stable gas area occurs (when $\xi \approx 0.09$).*

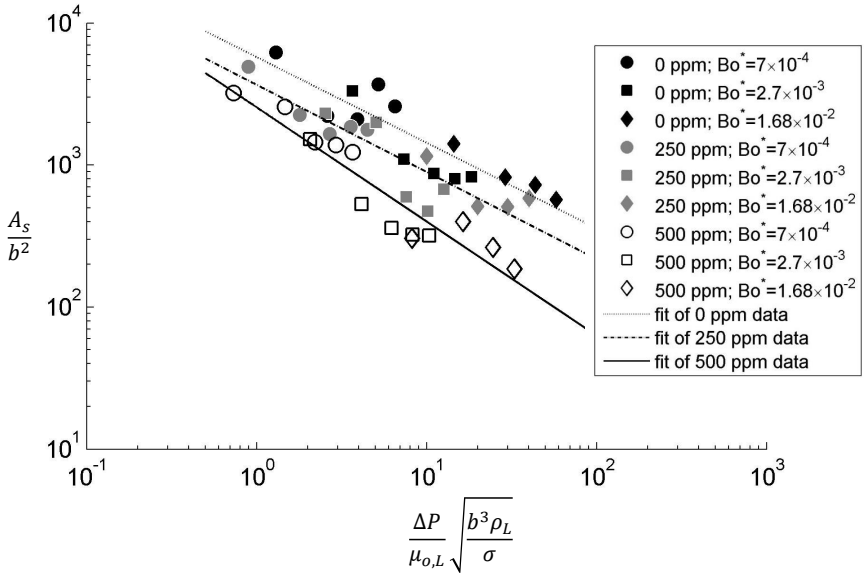

Figure 4.16 *The maximum stable gas area, A_s, is plotted against $\frac{\Delta P}{\mu_o}\sqrt{\frac{b^3\rho}{\gamma}}$. Best fit lines according to PIB concentration are included.*

Fig. 4.8. The t_{burst} data is fit with a single line and the t_s data is fit according to Bo^*.

In Fig. 4.15 traces of the inner and outer interfaces are shown for some experiments in a 250 μm gap at $\Delta t = t_s$. These images represent interfaces when $\xi \approx 0.09$ and $A_{gas} = A_s$. In Fig. 4.15 pressure increases from top to bottom and PIB concentration increases from left to right. The inner interface Γ_{in} and outer interface Γ_{out} is labeled in the top right and a scale bar is provided in the bottom right.

Plots of A_s for all experiments are shown in Fig. 4.16 where A_s is normalized by b^2 and the x-axis is scaled similarly to Fig. 4.8. For over about 2 decades in the x-direction and nearly two in the y-direction the data collapse somewhat according to PIB concentration. The data is fit according to PIB concentration and the slopes of the best fit lines are -0.60, -0.61 and -0.80 for the 0, 250 and 500 ppm PIB experiments, respectively.

From $t_s \leq \Delta t \leq t_{burst}$ ξ increases roughly linearly with time. Therefore data on that domain is fit with a linear line in Fig. 4.13 according to eq. 4.6 where the slope of this line is the instability growth rate ω_ξ. This rate is then plotted in Fig. 4.17 versus $Bo^* \cdot \frac{\Delta p}{\mu_o}$. There are

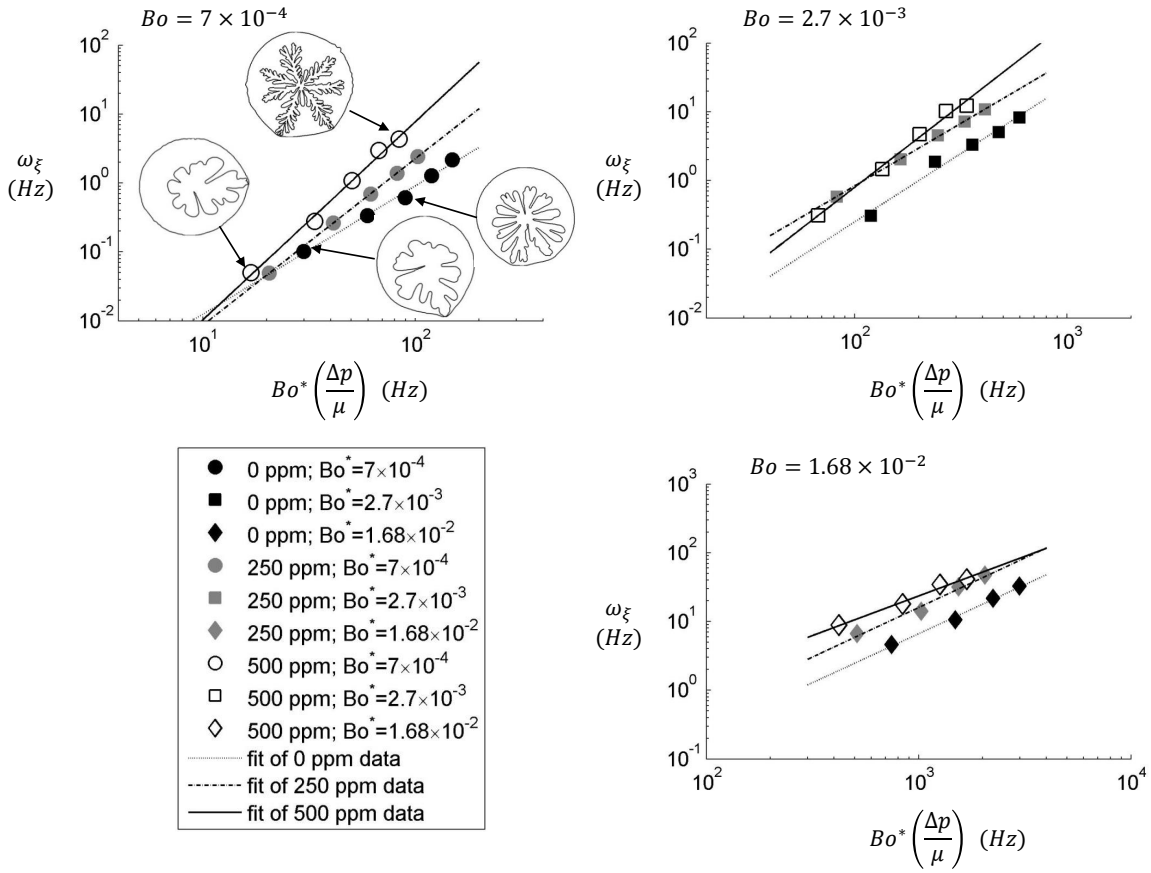

Figure 4.17 *Plots of the instability growth rate ω_ξ are shown separated by Bond number. In each individual plot the width of the x-axis is two decades and the height of the y-axis is 4 decades. For $Bo^* = 7 \times 10^{-4}$ images of the interfaces at t_{burst} are included and correspond to the experiment to which they point.*

three distinct plots representing ω_ξ versus $Bo^* \cdot \frac{\Delta p}{\mu_o}$ in Fig. 4.17 where in each plot Bo^* is constant. In each of the three individual plots the total width of the x-axis is two decades and the total height of the y-axis is 4 decades which allows for a visual comparison of the slopes of each best fit line. Images of the interfaces at $\Delta t = t_{burst}$ are shown in the $Bo^* = 7 \times 10^{-4}$ plot for a few experiments.

4.5 Discussion

The radial displacement of a liquid drop by a gas at constant pressure has clearly been achieved for both Newtonian and shear-thinning regimes based on the fingering behavior shown in Fig. 4.4-4.6. At the lowest pressure (1.4 kPa) in Fig. 4.4-4.6 the fingering regime appears mostly Newtonian for each liquid i.e. the fingers are "pedal-like" and new fingers develop through "tip-slitting" rather than "side-branching" as shown in detail in Fig. 4.7. Increasing the pressure introduces non-Newtonian side-branching behavior in the shear-thinning liquids. This could be due to some transition where a critical Weissenberg number, Wi^*, is reached where Wi^* is defined as

$$Wi^* = \dot{\gamma}\lambda \tag{4.18}$$

where $\dot{\gamma}$ is the shear rate and λ is the relaxation time. A Newtonian liquid would effectively have $\lambda \approx 0$ and $Wi^* \approx 0$ for all $\dot{\gamma}$, whereas a shear-thinning liquid would have $Wi^* > 0$ as the shear rate increases. While we do not have data on λ for the 250 and 500 ppm PIB liquids, one can speculate that $0 < \lambda_{250ppm} < \lambda_{500ppm}$. For low pressures $\dot{\gamma}$ is low and Wi^* is likely near 0. As the pressure, and therefore shear rate, increases then $Wi^* > 0$ and the non-Newtonian side-branching features begin.

The 500 ppm PIB experiments show the greatest amount of side-branching as would be expected. The pressure at which non-Newtonian viscous fingering first appears is lower for 500 ppm PIB experiments than 250 ppm PIB experiments because the relaxation time for the 500 ppm PIB liquid is likely larger than the 250 ppm PIB liquid. The Newtonian liquid exhibits almost no side-branching throughout all of the experiments; increasing the pressure for the

mineral oil experiments results in more and thinner fingers with smooth sides.

Additional qualitative results can be pulled away from Fig. 4.4-4.6. The distance from the gas inlet (marked by a '+') where the first fingers form is always greater for the Newtonian experiments. This result is consistent with previous results (67). Also since the area of the dotted circular fit is equal to A_{gas} one can observe visually that the gas area at t_{burst} is larger in the Newtonian liquid for nearly every pressure in each gap, and then the 250 ppm PIB liquid has a larger gas area than the 500 ppm PIB liquid. Therefore the displacement process is less efficient in shear-thinning liquids.

Varying the gap spacing in Fig. 4.4-4.6 also affects the fingering patterns. There is a noticeable lack of side-branching in the 250 μm experiments whereas the 50 μm non-Newtonian experiments show the most side-branching.

The time it takes for the gas phase to burst out of the liquid drop, t_{burst}, is plotted in Fig. 4.8 using the relation from eq. 4.1. All of the data collapse roughly onto a single curve for a range and domain of multiple decades. The exponent p from the best fit is -1.21 or about $-\frac{5}{4}$, yielding the relationship:

$$\frac{t_{burst}\nu_o b}{V_L} = -0.056\left[\frac{\Delta p}{\mu_o}\sqrt{\frac{\rho b^3}{\gamma}}\right]^{-\frac{5}{4}} \tag{4.19}$$

The exponent is a little smaller than the exponent of -1.38 found in previous work (7), however the scaling for t_{burst} has once again be shown to work very well. Consistently across the two decades of $\frac{\Delta p}{\mu_o}\sqrt{\frac{b^3\rho}{\gamma}}$ the experiments with PIB burst slightly faster than the Newtonian experiments.

Previous work with constant pressure radial displacement in a Hele-Shaw cell has shown that the gas phase expands exponentially with time with and without the viscous fingering instability (8). Each experiment in this chapter, be it Newtonian or shear-thinning, shows exponential growth in the gas area according to eq. 4.7. Figure 4.9 clearly shows this behavior for experiments in a 100 μm gap, but the same behavior is observed in 50 and 250 μm gaps. The data fits very well with eq. 4.7.

The gas expansion rates, ω_{gas}, from eq. 4.7 are plotted in Fig. 4.10 using $(Re^*)^2$ versus the

dimensionless group $Bo^* \cdot \frac{\rho b^2}{\mu_o}\left(\frac{\Delta p}{\mu_o}\right)$. The data collapse well according to PIB concentration. The exponent from eq. 4.14 is between 1.06 and 1.08 which is nearly unity. Flooring the exponent to 1 and simplifying eq. 4.14 results in the expression

$$\omega_{gas} = C_\omega \cdot Bo^* \cdot \frac{\Delta p}{\mu_o} \tag{4.20}$$

where C_ω = 0.006, 0.011 and 0.013 for the 0, 250 and 500 ppm PIB liquids, respectively. The exponent being nearly unity suggests $\omega_{gas} \sim \frac{\Delta p}{\mu_o}$. For 250 and 500 ppm PIB experiments at $Bo^* = 7 \times 10^{-4}$ it is clear that ω_{gas} has a greater dependence on $\frac{\Delta p}{\mu_o}$ than suggested by eq. 4.20 while the Newtonian expansion rates remain $\omega_{gas} \sim \frac{\Delta p}{\mu_o}$. At the two higher Bond numbers ω_{gas} scales more similarly for all experiments. The shifting up of the shear-thinning experiments in Fig. 4.10 may be due to choosing the 1 Hz viscosity; the shear rates undoubtedly vary with pressure and gap height and thus the effective viscosity in the shear-thinning liquids will change, but it would be difficult to determine local shear rates during the displacement process.

Previously an exponential model for the transient residual film thickness $h(\Delta t)$ was proposed in chapter 3. In this chapter a power law relationship between $h(\Delta t)$ and elasped time yielded the best fits. Initially the relationship $h(\Delta t) = C_{film}\,(\Delta t)^{n_{film}}$ was fit to the data whereupon the the exponent n_{film} was found to be about $-\frac{1}{2}$ for all experiments. The coefficient C_{film} varies with pressure and the polymer concentration so the data was fit using eq. 4.17. This resulted in good fits of the data as shown in Fig. 4.11. The values for C_{film} range between 20 and 40 $\mu m \cdot s^{\frac{1}{2}}$ and are shown in the inset of Fig. 4.11.

The residual film value at t_{burst}, denoted h_∞, is taken as the quasi-equilibrium film thickness. For experiments in the 50 μm gap the film was not sufficiently stable at t_{burst} i.e. $\frac{dh}{dt} \ll 0$ so those experiments are excluded from the residual film analysis. The equilibrium film is plotted in Fig. 4.12 versus Ca_p^* and scales roughly with $\Delta p^{0.4}$. The best fit curve in Fig. 4.12 is defined by

$$\frac{h_\infty}{b} = -2.21\left[\frac{\mu_o}{\gamma}\sqrt{\frac{\Delta p}{\rho}}\right]^{\frac{4}{5}} \tag{4.21}$$

In general experiments with less polymer added resulted in slightly larger film thicknesses.

Previous studies on the residual film resulting from two-phase displacement have found that the film scales with $Ca^{\frac{2}{3}}$ (17; 64), however the capillary number used here is of course defined differently.

In Fig. 4.13 the fingering magnitude ξ, as defined in eq. 4.6, is plotted versus elapsed time. There is always an initial period where A_{gas} expands as a circle and the interface is stable. This initial period of stable displacement is significantly longer when the gap height is increased. In Fig. 4.14 the length of this initially stable period, t_s, is plotted along with t_{burst} using the same scaling. It is clear from both Fig. 4.14a and 4.14b that, based on the best fits, there will be some combination of system parameters where t_s and t_{burst} will intersect. It is then theoretically possible to use Fig. 4.14 to predict what pressures, drop volumes, etc. will yield stable displacement all the way to t_{burst}.

Images of the interfaces in a 250 μm gap when the maximum stable gas area occurs are shown in Fig. 4.15. These interfaces in Fig. 4.15 represent interfaces when $\xi \approx 0.09$, the chosen viscous fingering threshold. It is clear that these interfaces are mostly circular but show the very first signs of viscous fingering. It is also clear visually that the maximum stable gas areas are significantly larger for the Newtonian experiments than the experiments with PIB in Fig. 4.15. The maximum stable gas areas A_s for all experiments are plotted in Fig. 4.16 and show that the shear-thinning experiments always have smaller maximum stable gas areas. The maximum stable area scales roughly with $\Delta p^{-\frac{2}{3}}$. It is important to note that during the stable displacement periods the gas area is expanding exponentially e.g. the exponential growth is not exclusive to the fingering instability.

Once $\xi > 0.09$ it is clear that ξ grows linearly with time for most experiments in Fig. 4.13. Zhao and Maher reported a similar linear trend for a linear Hele-Shaw cell (70). A few experiments in Fig. 4.13 deviate slightly from the linear trend but these are exceptions. The fact that ξ grows linearly on the domain $t_s \leq \Delta t \leq t_{burst}$ means literally the length of the actual liquid-gas interface increases linearly with respect to the radius of the corresponding stable case R_{fit}, and since R_{fit} grows exponentially with time then ξ grows as the product of an exponential and linear function of time. Using $R_{fit}(\Delta t) = \sqrt{\frac{A_{gas}(\Delta t)}{\pi}}$ along with eq. 4.6 and eq. 4.7 on $t_s \leq \Delta t \leq t_{burst}$ results in an expression for the length of the interface during both

the stable and unstable periods:

$$L(\Delta t) = \begin{cases} 2\sqrt{\pi}\left[C_{gas}\left(e^{\omega_{gas}\Delta t}-1\right)\right]^{\frac{1}{2}} & : 0 \le \Delta t < t_s \\ 2\sqrt{\pi}\left[C_{gas}\left(e^{\omega_{gas}\Delta t}-1\right)\right]^{\frac{1}{2}}\left[\omega_\xi\left(t_s-\Delta t\right)+1\right] & : t_s \le \Delta t \le t_{burst} \end{cases} \tag{4.22}$$

where ω_ξ is the viscous fingering propagation rate from eq. 4.6. The rate ω_ξ is found by taking the slopes of the linear fits in Fig. 4.13. In Fig. 4.17 ω_ξ is plotted against $Bo^* \cdot \frac{\Delta p}{\mu_o}$ which provides the relation:

$$\omega_\xi = C_\xi \left[Bo^* \cdot \frac{\Delta p}{\mu_o}\right]^n \tag{4.23}$$

The slopes of the best fits of the data in Fig. 4.17 according to eq. 4.23 vary with Bo^*, so the data is separated for clarity. At $Bo^* = 7 \times 10^{-4}$ n = 1.86, 2.41 and 2.87 for the 0, 250 and 500 ppm PIB experiments, respectively. At this Bo^* the instability grows faster with increasing PIB, and experiments with PIB are more dependent on $\frac{\Delta p}{\mu_o}$. Traces of the corresponding experimental interfaces are shown for some of the $Bo^* = 7 \times 10^{-4}$ experiments to highlight differences in the fingering instabilities. As Bo^* increases ω_ξ scales with Δp perhaps more similarly for Newtonian and shear-thinning experiments. For $Bo^* = 2.7 \times 10^{-3}$ n = 1.98, 1.82 and 2.39 for the 0, 250 and 500 ppm PIB experiments, respectively. For $Bo^* = 1.68 \times 10^{-2}$ n = 1.42, 1.44 and 1.15 for the 0, 250 and 500 ppm PIB experiments, respectively. For all Bo^* and all pressures the viscous fingering instability grows faster for shear-thinning experiments than for Newtonian experiments.

4.6 Conclusion

The displacement of a finite liquid drop of both Newtonian mineral oil and non-Newtonian mineral oil with dissolved polyisobutylene has been studied by injecting air at a constant pressure into the drop while confined in a Hele-Shaw cell. Qualitative results show that at low pressures the viscous fingering behavior is similar for both Newtonian and shear-thinning liquids. Increasing the pressure above some critical value introduces the characteristic side-branching features in the shear-thinning liquids. Previous work has studied viscous fingering

in the context of varying the Weissenberg number, Wi^*, where a critical Wi^* typically results in a transition from Newtonian to non-Newtonian behavior in non-Newtonian liquids (24). We have certainly observed a transition, although without data on the relaxation times for PIB in mineral oil it is impossible to attribute the transition to a specific Wi^*. Regardless some clear qualitative trends occur in Fig. 4.4-4.6:

i) there is a critical gas pressure above which shear-thinning liquids exhibit side-branching as the primary growth pattern as opposed to Newtonian tip-splitting; increasing the gas pressure further increases the occurrence of side-branching in shear-thinning liquids.
ii) the distance from the gas inlet from which viscous fingering begins is significantly smaller for shear-thinning liquids.
iii) increasing the gap spacing reduces side-branching (non-Newtonian effects) and increases the critical gas pressure for non-Newtonian effects to become present.

The time it took for the gas phase to escape the liquid drop, t_{burst}, was measured and was found to fit well to the power law relationship in eq. 4.19. The exponent in eq. 4.19 is $-\frac{5}{4}$ which is a little smaller than the exponent from chapter 2 which was -1.38. The exponential increase in the gas area A_{gas} with time has again been observed just like in chapter 2 and 3. The exponential behavior was observed in both Newtonian and non-Newtonian regimes. As shown in Fig. 4.13 there is an initial period where the displacement is stable i.e. no viscous fingering is present. Even during this period A_{gas} increases exponentially with time. The gas area expansion rate ω_{gas} was found to fit well to the relationship in eq. 4.14 where the exponent is between 1.06 and 1.08. The following conclusions on the gas area expansion can be made:

iv) the time it takes for the gas phase to burst through the liquid drop decreases with increasing pressure, gap height or viscosity, and increases with increasing volume.
v) $A_{gas}(\Delta t)$ increases exponentially with time for both Newtonian and shear-thinning liquids and with and without viscous fingering.
vi) the exponential gas area expansion rate from eq. 4.7 goes roughly like $\omega_{gas} \sim \frac{\Delta p}{\mu_o}$.

In chapter 3 an exponential fit was attempted for the transient residual film thickness. In this chapter a power law model was attempted with good fits as shown in Fig. 4.11. The fits work particularly well at later times; the power law model naturally has an asymptote at Δt = 0 so it is impossible to fit the first few data points. When applying the power law model in eq. 4.17 it was found that the exponent n_{film} was roughly $-\frac{1}{2}$ for all experiments, suggesting a diffusion-like process. With the exponent fixed values for C_{film} were found between $20 \leq C_{film} \leq 40\ \mu m \cdot s^{\frac{1}{2}}$. Then the film at t_{burst} was taken as the quesi-equilibrium film thickness which was fit to eq. 4.21. In that relationship it follows that $h_\infty \sim \Delta p^{0.4}$. In summary:

vii) the transient residual film forms according to $\Delta t^{-\frac{1}{2}}$.
viii) the quasi-equilibrium film thickness at t_{burst} goes like $h_\infty \sim \Delta p^{0.4}$.

A new method for quantifying the viscous fingering instability has been introduced resulting in the *fingering magnitude*, ξ. This quantity was able to highlight two distinct displacement regimes: an initial stable or circular displacement from $0 \leq \Delta t \leq t_s$ where $\xi < 0.09$, and an unstable displacement with viscous fingering from $t_s < \Delta t \leq t_{burst}$. At elapsed time t_s the maximum stable gas area occurs and it was found that the Newtonian experiments always had larger A_s than the shear-thinning experiments. In the viscous fingering period ξ increases linearly with time, so during this period the slope of the best fit is theinstability growth rate ω_ξ from eq. 4.6. Values for ω_ξ could be found for both Newtonian and non-Newtonian experiments and ω_ξ was always lower for the Newtonian experiments than for the shear-thinning experiments. At the lowest Bo^* the shear-thinning liquids had a greater dependence of ω_ξ on Δp, and as the gap height increased the dependence of ω_ξ on Δp became similar for both Newtonian and shear-thinning experiments. Because ξ is a relative measure of the actual liquid-gas interface L to the corresponding stable radius R_{fit} described in section 4.2.2 and R_{fit} grows exponentially with time, L grows as the product of an exponential and linear function of time. Then the length of the liquid-gas interface could be described as a function of C_{gas}, ω_{gas}, ω_ξ and Δt in eq. 4.22. In summary:

ix) all experiments exhibit an initial stable displacement period followed by viscous fingering until t_{burst}.

x) the maximum stable gas area A_s is always larger for Newtonian liquids compared to shear-thinning liquids.

xi) the fingering magnitude ξ increases linearly with time and L increases as the product of an exponential and linear function of time.

xii) the instability growth rate ω_ξ is always smaller for Newtonian experiments.

xiii) ω_ξ has a significantly greater dependence on Δp for shear-thinning experiments in a 50 μm gap compared to Newtonian experiments.

CHAPTER 5. GENERAL CONCLUSION AND FUTURE WORK

5.1 General conclusion

In this thesis the constant-pressure gas-driven displacement of a finite liquid drop in a radial Hele-Shaw was studied. In chapter 2 the problem was studied using air to displace a water-glycerol mixture. This paper, originally published in 2011, first showed the exponential expansion of the gas phase with time as it displaced the liquid phase. Also a first attempt at estimating the film thickness in a finite drop in the presence of viscous fingering was made. Chapter 3 continued the work from chapter 2 by attempting to observe an interfacial chemical reaction in a CO_2 - $Ca(OH)_{2(aq)}$ system. Improvements in the analysis techniques allowed for an estimation of the film formation rate as part of an exponential model.

It is in chapter 4 that some great improvements were made in the analysis process. Improved image analysis allowed for the liquid-gas interfaces to be traced. While before areas were measured by counting pixels within a region, now an integral method using the Kelvin-Stokes theorem could be used to calculate the area based on the liquid-gas interface. It was also possible to measure the length of the interface. This led to the new fingering magnitude quantity. This new quantity is a novel way to quantify the viscous fingering instability across very different fingering patterns.

There is a seemingly infinite number of projects that can stem from this relatively simple experiment. A couple future projects based on the constant pressure displacement problem are briefly described in the next sections.

5.2 Future work

5.2.1 Potential flow analysis for stable radial displacement

In chapters 2-4 the constant pressure radial displacement of a liquid in a Hele-Shaw cell has shown that the displaced area $A_{gas}(t)$ increases exponentially with time. This result was reached by assuming an empirical relationship. As stated before the constant pressure system makes an analytical solution difficult particularly in the presence of the viscous fingering instability. However some experiments in chapter 3 under low pressure with low viscosity liquid have resulted in very little viscous fingering while still exhibiting an exponential increase in A_{gas}. This special case of the stable displacement can potentially be described analytically using a potential flow analysis.

Consider the constant-pressure radial displacement problem described throughout this thesis. For an incompressible and irrotational flow the continuity equation for the gas phase is

$$\frac{1}{r}\frac{d}{dr}\left(r\frac{d\phi}{dr}\right) = 0 \tag{5.1}$$

where ϕ is the velocity potential $\phi = \frac{du_r}{dr}$. Since there is no pressure gradient in the gas phase an interfacial stress balance at the liquid-gas interface can be used to find a form for $\frac{du_r}{dr}$. The stress balance at the interface is $\mathbf{n}\cdot\|\boldsymbol{\sigma}\| = \gamma\kappa\cdot\mathbf{n}$ where $\boldsymbol{\sigma} = -P\mathbf{I}+\boldsymbol{\tau}$, $\boldsymbol{\tau} = \mu[\nabla\mathbf{u}+(\nabla\mathbf{u})^T]$ and $\|*\|$ denotes a jump across the interface. Along the gas side of the interface a commonly imposed boundary condition is zero shear stress or $\frac{du_r}{dz} = 0$ which implies that the tangential component of the interfacial stress is negligible. Therefore the normal component of the stress balance will be used, $\mathbf{n}\cdot\|\boldsymbol{\sigma}\|\cdot\mathbf{n} = \gamma\kappa$. The only nonzero term in $\nabla\mathbf{u}$ is $\frac{du_r}{dr}$ and to satisfy continuity $\frac{du_r}{dr}|_L = \frac{du_r}{dr}|_g$, so the stress balance can be written

$$(-P_L + P_g) + 2(\mu_L - \mu_g)\frac{du_r}{dr} = \gamma\kappa \tag{5.2}$$

The liquid viscosity is much larger than the gas viscosity such that $\frac{\mu_g}{\mu_L} \ll 1$. Then, dividing the above equation by μ_L and subbing in ΔP yields

$$\frac{-\Delta P}{\mu_L} + 2\frac{du_r}{dr} = \frac{\gamma\kappa}{\mu_L} \tag{5.3}$$

The pressure contribution from the curvature of the interface depends on both the curvature in the r-plane and the curvature in the z-plane:

$$\gamma\kappa = \gamma\left(\frac{1}{b-\bar{h}} + \frac{1}{a_r}\right) \tag{5.4}$$

where a_r is the radius of curvature in the r-plane at a given point along the interface. The contribution from $\frac{\gamma}{a_r}$ is only important when $a_r \sim b$ which is only at very early elapsed times, so that can be neglected. The contribution from curvature in the z-plane, $\frac{\gamma}{b-\bar{h}}$, can dominate when $\bar{h} \to b$. It has been shown that for low pressures, e.g. $\Delta P = O(\frac{\gamma}{b})$, the residual film can range between $0.1b \leq \bar{h} \leq 0.5b$ indicating this pressure contribution cannot be neglected and

$$\frac{du_r}{dr} = \frac{1}{2\mu_L}\left(\Delta P - \frac{\gamma}{b-\bar{h}}\right) \tag{5.5}$$

Inserting this into eq. 5.5 yields

$$\left(\frac{2\mu_L}{\Delta P - \frac{\gamma}{b-\bar{h}}}\right)\frac{dr}{dt} = r \tag{5.6}$$

where $\frac{dr}{dt} = u_r$ at the interface. Integrating eq. 5.6 with respect to time and using $r(0) = a_{in}$ where a_{in} is the gas inlet radius results in:

$$r(t) = a_{in}e^{\omega_o t} \tag{5.7}$$

where $\omega_o = \frac{2\mu_L}{\Delta P - \frac{\gamma}{b-\bar{h}}}$. Then the area of the stable circular displaced area is $A_{gas}(t) = \pi[r(t)]^2$ or

$$A_{gas}(t) = C_{gas}e^{2\omega_o t} \tag{5.8}$$

where the constant C_{gas} is identically the cross sectional area of the gas inlet $\pi(a_{in})^2$. This solution is expected to be valid only when $\Delta P = O(\frac{\gamma}{b})$, requiring very low pressures. While this analytical solution is currently a work in progress, the fact that an exponential solution is found is promising since throughout this thesis the gas area has been found to grow exponentially

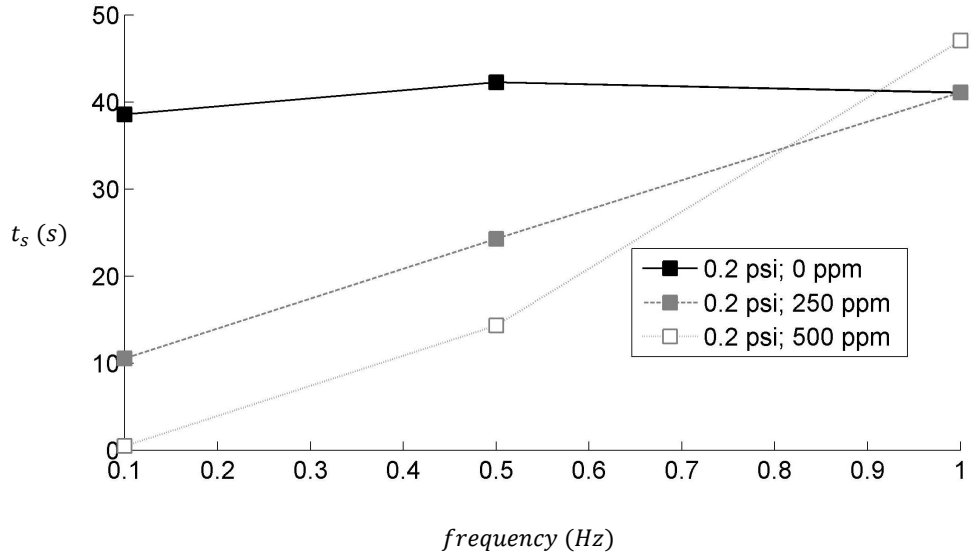

Figure 5.1 *The time it takes for the instability to devlop, t_s, is plotted versus the pulsing frequency in Hz. The maximum pressure is 0.2 psi (1.4 kPa) and the black, gray and unfilled markers correspond to 0, 250 and 500 ppm experiments, respectively.*

with time. In the future we hope to complete some radial Hele-Shaw experiments at these very low pressures with liquids of varying viscosity to compare the experimental results to this solution. The solution will also be expanded to include an exponential or power law model for the film thickness as has been observed in chapter 3 and 4.

5.2.2 Pulsed-pressure displacement

A lot of recent work has dealt with trying to control or eliminate the viscous fingering instability such as by using elastic plates in a Hele-Shaw cell (33) and introducing gradients in the gap height (34). In a pressure driven system the use of a pulsed pressure approach i.e. cycling between $\Delta p = p_{gas}$ and $\Delta_p = 0$ could have the effect of stabilizing the interface without needing to alter the geometry of the system.

Some preliminary experiments have been completed using mineral oil with and without PIB in a 100 μm gap. In these experiments a procedure like that used in chapter 4 was used.

In Fig. 5.1 the time it takes for the instability to develop, t_s, is plotted versus the pulsing frequency. The drop volume is 200 μL and the maximum pressure is 0.2 psi (1.4 kPa). The pulsing frequencies shown are 0.1, 0.5 and 1 Hz with a duty cycle of 20%. The t_s for the 0 ppm liquid remains almost constant at about 40 s for each frequency. However it is clear that as the frequency increases the 250 and 500 ppm liquids remain stable for a longer period of time. In fact at 1 Hz the 500 ppm experiment remains stable longer than the Newtonian experiment.

This is a very interesting preliminary result because in chapter 4 the non-Newtonian liquids always became unstable earlier than the Newtonian liquid. As the frequency increases beyond 1 Hz and becomes almost indistinguishable to a constant pressure injection there will likely be a point at which the non-Newtonian interfaces become unstable earlier than the Newtonian ones again. Therefore there may exist some optimum frequency for the stability of the shear-thinning liquids. In the future experiments at higher frequencies will be performed and other liquids will be used such as polyacrylamide solutions.

BIBLIOGRAPHY

[1] M. Muskat, R. D. Wyckoff. An approximate theory of water-coning in oil production. *Trans. A.I.M.E.* Tulsa meeting, October (1934)

[2] M. G. Arthur. Fingering and coning of water and gas in homogenous oil sand. *Trans. A.I.M.E.* Los Angeles meeting, October (1941)

[3] S. J. Liu, Y. C. Wu. Dynamic visualization of cavity-filling process in fluid-assisted injection molding-gas versus water. *Poly. Test.* **26**, (2007)

[4] M. A. Parvez, N. S. Ong, Y. C. Lam, S. B. Tor. Gas-assisted injection molding: the effects of process variables and gas channel geometry *J. Mater. Process. Tech.* **121**, (2002)

[5] N. Roos, M. Wissen, T. Glinsner, H. C. Scheer. Impact of vacuum environment on the hot embossing process. *Proc. SPIE* **5037**, (2003)

[6] J. Peng, T. Han, Y. Yang, B. Li. Pattern formation in polymer films under the mask. *Polymer* **44**, (2003)

[7] T. Ward, A. R. White. Gas-driven displacement of a liquid in a partially filled radial Hele-Shaw cell. *Phys. Rev. E* **83**, (2011)

[8] A. R. White, T. Ward. CO_2 sequestration in a radial Hele-Shaw cell via an interfacial chemical reaction. *Chaos* **22**, (2012)

[9] L. Carrillo, J. Soriano, J. Ortin. Radial displacement of a fluid annulus in a rotating Hele-Shaw cell. *Phys. Fluids* **11**, 4 (1999)

[10] D. J. Lewis. The instability of liquid surfaces when accelerated in a direction perpendicular to their planes II. *P. R. Soc. A* **202**, 1068 (1950)

[11] G. Taylor. The instability of liquid surfaces when accelerated in a direction perpendicular to their planes I. *P. R. Soc. A* **201**, (1950)

[12] H. S. Hele-Shaw. The flow of water. *Nature* **58**, 1489 (1898)

[13] P. G. Saffman, G. Taylor. The penetration of a fluid into a porous medium or Hele-Shaw cell containing a more viscous liquid. *P. R. Soc. A* **245**, (1958)

[14] R. L. Chuoke, P. van Meurs, C. van der Poel. The instability of slow, immiscible, viscous liquid-liquid displacements in permeable media. *Trans. A.I.M.E.* **216**, (1959)

[15] G. M. Homsy. Viscous fingering in porous media. *Ann. Rev. Fluid Mech.* (1987)

[16] L. Paterson. Radial fingering in a Hele Shaw cell *J. Fluid Mech.* **113**, (1981)

[17] C. W. Park, G. M. Homsy. Two-phase displacement in Hele-Shaw cells: theory. *J. Fluid Mech.* **139**, (1984)

[18] C. W. Park, S. Gorell, G. M. Homsy. Two-phase displacement in Hele-Shaw cells: experiments on viscously driven instabilities. *J. Fluid Mech.* **141**, (1984)

[19] J. Nittmann, G. Daccord, H. E. Stanley. Fractal growth of viscous fingers: quantitative characterization of a fluid instability phenomenon. *Nature* **314**, (1985)

[20] G. Daccord, J. Nittmann. Radial viscous fingers and diffusion-limited aggregation: fractal dimension and growth sites. *Phys. Rev. Letters* **56**, 4 (1986)

[21] A. Buka, P. Palffy-Muhoray. Stability of viscous fingering patterns in liquid crystals. *Phys. Rev. A* **36**, 3 (1987)

[22] A. Buka, P. Palffy-Muhoray, Z. Racz. Viscous fingering in liquid crystals. *Phys. Rev. A* **36**, 8 (1987)

[23] T. Yamamoto, H. Kamikawa, H. Tanaka, K. Nakamura, N. Mori. Viscous fingering of non-Newtonian fluids in a rectangular Hele-Shaw cell. *J. Soc. Rheol. Jpn.* **29**, 2 (2001)

[24] P. Fast, L. Kondic, M. J. Shelley, P. Palffy-Muhoray. Pattern formation in non-Newtonian Hele-Shaw flow. *Phys. Fluids* **13**, 5 (2001)

[25] P. Fast, M. J. Shelley. A moving overset grid method for interface dyanmics applied to non-Newtonian Hele-Shaw flow. *J. Comp. Phys.* **195**, (2004)

[26] K. V. McCloud, J. V. Maher. Experimental perturbations to Saffman-Taylor flow. *Phys. Rep.* **260**, (1995)

[27] A. De Wit, G. M. Homsy. Viscous fingering in reaction-diffusion systems. *J. Chem. Phys.* **110**, 17 (1989)

[28] A. De Wit. Fingering of chemical fronts in porous media. *Phys. Rev. Letters* **87**, 5 (2001)

[29] J. Fernandez, G. M. Homsy. Viscous fingering with chemical reaction: effect of in-situ production of surfactants. *J. Fluid Mech.* **480**, (2003)

[30] Y. Nagatsu, K. Matsuda, Y. Kato, Y. Tada. Experimental study on miscible viscous fingering involving viscosity changes induced by variations in chemical species concentrations due to chemical reactions. *J. Fluid Mech.* **571**, (2007)

[31] H. Kim, T. Funada, D. D. Joseph, G. M. Homsy. Viscous potantial flow analysis of radial fingering in a Hele-Shaw cell. *Phys. Fluids* **21**, (2009)

[32] M. C. Dallaston, S. W. McCue. New exact solution for Hele-Shaw flow in doubly connected regions. *Phys. Fluids* **24**, (2012)

[33] D. Pihler-Puzovic, R. Perillat, M. Heil, A. Juel. Modelling the suppression of radial fingering in elastic Hele-Shaw cells. *APS DFD* San Diego meeting, November (2012)

[34] T. T. Al-Housseiny, P. A. Tsai, H. A. Stone. Control of interfacial intabilities using flow geometry. *Nat. Phys.* **8**, (2012)

[35] M. Blunt, F. J. Fayers and F. M. Orr, Carbon dioxide in enhanced oil recovery. Energy Convers. Manag. **34** 1197 (1993)

[36] V. S. Ajaev and G. M. Homsy, Steady vapor bubbles in rectangular microchannels. J. Colloid Interface Sci. **240** 259 (2001)

[37] D. H. Cho, Expansion of a cold bubble suddenly formed in a hot liquid. Chem. Engng. Sci. **26** 1235 (1971)

[38] V. K. Dhir, Numerical simulations of pool-boiling heat transfer. AICHE J. **47** 813 (2001)

[39] D. Banerjee and V. K. Dhir, Study of subcooled film boiling on a horizontal disc: part 1 - analysis. ASME J. Heat Transfer **123** 271 (2001)

[40] M. B. Gratton and T. P. Witelski, Coarsening of unstable thin films subject to gravity. Phys. Rev. E, **77** 016301 (2008)

[41] D. A. Reinelt, P. G. Saffman. The penetration of a finger into a viscous fluid in a channel and tube. *SIAM J. Sci. Stat. Comput.* **6**, 3 (1985)

[42] L. Schwartz, Stability of Hele-Shaw flows: the wetting-layer effect. Phys. Fluids **29** 3086 (1986)

[43] J. Vanden-Broeck. Fingers in a Hele-Shaw cell with surface tension. *Phys. Fluids* **26**, 2011 (1983)

[44] D. Bensimon, L. P. Kadanoff, S. Liang, B. I. Shraiman, C. Tang, Viscous flows in two dimensions. Rev. Mod. Phys. **58** 977 (1986)

[45] B. G. Cox. On driving a viscous fluid out of a tube. *J. Fluid Mech.* **14**, (1962)

[46] F. Fairbrother and A. E. Stubbs, Studies in electro-endosmosis. Part IV. The "bubble-tube" method of measurement. J. Chem. Soc. **1** 527 (1935)

[47] G. I. Taylor. Deposition of a viscous fluid on the wall of a tube. *J. Fluid Mech.* **10**, (1961)

[48] J. D. Chen. Measuring the film thickness surrounding a bubble inside a capillary. *J. Colloid. Interf. Sci.* **109**, 2 (1986)

[49] D. A. Reinelt, Interface conditions for two-phase displacement in Hele-Shaw cells. J. Fluid Mech. **183** 219 (1987)

[50] E. Meiburg, Bubbles in a Hele-Shaw cell: numerical simulation of three-dimensional effects. Phys. Fluids A **1** 938 (1989)

[51] T. Maxworthy, Experimental study of interface instability in a Hele-Shaw cell. Phys. Rev. A **39** 5863 (1989)

[52] E. Álvarez-Lacalle, J. Ortín and J. Casademunt, Relevance of dynamic wetting in viscous fingering patterns. Phys. Rev. E **74** 025302(R) (2006)

[53] J. M. Smith, H. C. Van Ness Introduction to Chemical Engineering Thermodynamics 4th Ed. McGraw-Hill, New York (1987)

[54] R. C. Ernst, C. H. Watkins and H. H. Ruwe, The physical properties of the ternary system ethyl alcohol-glycerin-water. J. Phys. Chem. **40** 627 (1936)

[55] P. N. Shankar, M. Kumar, Experimental determination of the kinematic viscosity of glycerol-water mixtures. Proc. R. Soc. Lond. A **444** 573 (1994)

[56] T. Ward, Radial spreading of a viscous drop between parallel-plane surfaces. Phys. Fluids **18** 093101 (2006)

[57] G. Montes-Hernandez, R. Perez-Lopez, F. Renard, J. M. Nieto, L. Charlet. Mineral sequestration of CO_2 by aqueous carbonation of coal combustion fly-ash. J. Hazard. Mater. **161** 1347 (2009)

[58] D. N. Huntzinger, J. S. Gierke, S. K. Kawatra, T. C. Eisele, L. L. Sutter. Carbon dioxide sequestration in cement kiln dust through mineral carbonation. Environ. Sci. Technol. **43** 1986 (2009)

[59] H. Kojima, M. Hakuta, K. Kudoh, T. Ichinoseki, H. Midorikawa. Chemical absorption into slurry in gas-sparged stirred vessel under continuous operation. J. Chem. Eng. Jpn. **22** 621 (1989)

[60] W. Dreybrodt, L. Eisenlohr, B. Madry, S. Ringer. Precipitation kinetics of calcite in the system $CaCO_3 - H_2O - CO_2$: the conversion to CO_2 by the slow process $H^+ + HCO_3^- \rightarrow CO_2 + H_2O$ as a rate limiting step. Geochim. Cosmochim. Ac. **61** 3897 (1997)

[61] Z. Liu, W. Dreybrodt. Dissolution kinetics of calcium carbonate minerals in H_2O CO_2 solutions in turbulent flow: the role of the diffusion boundary layer and the slow reaction $H_2O + CO_2 \rightleftharpoons H^+ + HCO_3^-$. Geochim. Cosmochim. Ac. **61** 2879 (1997)

[62] T. Podgorski, M. C. Sostarecz, S. Zorman and A. Belmonte. Fingering instabilities of a reactive micellar interface. Phys. Rev. E **76** 016202 (2007)

[63] D. Kern. The hydration of carbon dioxide. J. Chem. Edu. **37** 14 (1960)

[64] F. P. Bretherton. The motion of long bubbles in tubes. *J. Fluid Mech.* **10**, (1961)

[65] H. W. H. Yang. Water-based polymers as pressure-sensitive adhesives-viscoelastic guidelines. J. Appl. Polym. Sci. **55** 645 (1995)

[66] H. Zhao, J. V. Maher. Associating-polymer effects in a Hele-Shaw experiment. *Phys. Rev. E* **47**, 6 (1993)

[67] J. E. Sader, D. Y. C. Chan, B. D. Hughes. Non-Newtonian effects on immiscible viscous fingering in a radial Hele-Shaw cell. *Phys. Rev. E* **49**, 1 (1994)

[68] S. D. R. Wilson. The Taylor-Saffman problem for a non-Newtonian liquid. *J. Fluid Mech.* **220**, (1990)

[69] D. Lindner, E. Bonn, C. Poire, M. B. Amar, J. Meunier. Viscous fingering in non-Newtonian fluids. *J. Fluid Mech.* **469**, (2002)

[70] H. Zhao, J. V. Maher. Viscous-fingering experiments with periodic boundary conditions. *Phys. Rev. A* **42**, 10 (1990)